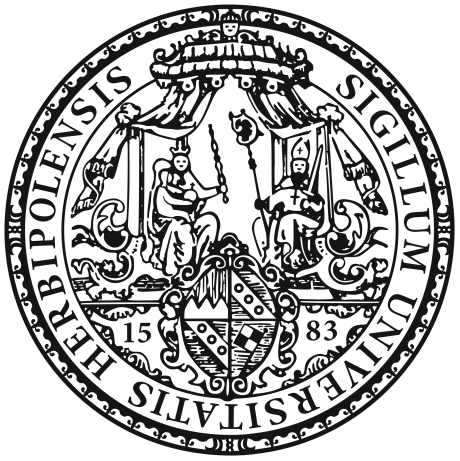

The pathogenicity and origin of auto-antibodies in chronic inflammatory demyelinating polyradiculoneuropathy and the identification of cutaneous biomarkers in Charcot-Marie-Tooth 1A patients

Die Pathogenität und Herkunft von Auto-Antikörpern bei chronisch inflammatorischer demyelinisierender Polyradikuloneuropathie und die Identifikation von Biomarkern in Haut von Charcot-Marie-Tooth 1A Patienten

Doctoral thesis for a doctoral degree
at the Graduate School of Life Sciences,
Julius-Maximilians-Universität Würzburg,
Section Neuroscience.

Submitted by

Beate Hartmannsberger

from

Kaufbeuren

Würzburg, 2020

Submitted on:

Members of the *Promotionskomitee*:

Chairperson:	**Prof. Dr. Carmen Villmann**
Primary Supervisor:	**Prof. Dr. Claudia Sommer**
Supervisor (second):	**Prof. Dr. Rudolf Martini**
Supervisor (third):	**Prof. Dr. Heike Rittner**
Supervisor (fourth):	**PD Dr. Kathrin Doppler**

Date of Public Defense:

Date of Receipt of Certificates:

Affidavit

I hereby confirm that my thesis entitled "The pathogenicity and origin of auto-antibodies in chronic inflammatory demyelinating polyradiculoneuropathy and the identification of cutaneous biomarkers in Charcot-Marie-Tooth 1A patients" is the result of my own work. I did not receive any help or support from commercial consultants. All sources and / or materials applied are listed and specified in the thesis.

Furthermore, I confirm that this thesis has not yet been submitted as part of another examination process neither in identical nor in similar form.

Place, date Signature

Eidesstattliche Erklärung

Hiermit erkläre ich an Eides statt, die Dissertation "Die Pathogenität und Herkunft von Auto-Antikörpern bei chronisch inflammatorischer demyelinisierender Polyradikuloneuropathie und die Identifikation von Biomarkern in Haut von Charcot-Marie-Tooth 1A Patienten" eigenständig, d.h. insbesondere selbständig und ohne Hilfe eines kommerziellen Promotionsberaters, angefertigt und keine anderen als die von mir angegebenen Quellen und Hilfsmittel verwendet zu haben.

Ich erkläre außerdem, dass die Dissertation weder in gleicher noch in ähnlicher Form bereits in einem anderen Prüfungsverfahren vorgelegen hat.

Ort, Datum Unterschrift

Contents

Parts of the results presented in this thesis have been published:

Hartmannsberger, B., Doppler, K., Stauber, J., Schlotter-Weigel, B., Young, P., Sereda, M. W., & Sommer, C. (2020). Intraepidermal nerve fiber density as biomarker in Charcot-Marie-Tooth disease 1A. *Brain Communications*, *2*(1), fcaa012.

The published manuscript and this thesis contain similar text passages in adapted form in some sections.

Abstract

Peripheral neuropathies can severely affect patients. Causes for the disease are diverse but can be classified into two main groups, acquired and hereditary. Examples for these two types are chronic inflammatory demyelinating polyradiculoneuropathy (CIDP) and Charcot-Marie-Tooth disease type 1A (CMT1A).

CIDP has an estimated prevalence of about 1-9:100 000. In this pathogenetically hetereogeneous patient group about 5-10% show auto-antibodies against the node of Ranvier and present with distinct symptoms. Treatment with rituximab - a monoclonal antibody that deletes $CD20^+$ B cells - has been shown to be effective in a majority of auto-antibody associated CIDP cases. This suggests that B cells and the produced auto-antibodies might be pathogenic. Previous studies delivered evidence that auto-antibodies alone can induce nerve damage.

In this study, the aim was to investigate the pathomechanism of auto-antibodies *in vivo* and their exact origin: For the analysis of the pathogenicity of auto-antibodies, passive transfer experiments on Lewis rats were performed with whole IgG from a patient with anti-contactin-1 (CNTN1) IgG4 auto-antibodies. IgG was infused through an intrathecal catheter targeting the thoracic/lumbar region of the spine over a long-term, 3-week period. In a previous study of our group, the IgG from the same patient has been reported to have mild pathogenic effects when applied intraneurally into the sciatic nerve of Lewis rats. In this study however, binding of auto-antibodies to nerve roots could not be detected. Neither evaluation of electrophysiological properties after the injection period nor motor and sensory skills tested throughout the injection period showed differences when compared to animals infused with control IgG. This suggests that in the chronic intrathecal protocol anti-CNTN1 auto-antibodies did not have a pathogenic effect.

In peripheral blood, four B cell subsets capable to produce antibodies were previously described: memory B cells, plasmablasts (PBs), B1 cells and $CD20^+CD38^{hi}$ cells. For the identification of the B cell subsets that produce auto-antibodies, purification and sort protocols as well as an enzyme-linked immuno spot (ELISpot) assay for IgG and IgM were established successfully. Since unstimulated B cell subsets produced very small amounts

of IgG and IgM, peripheral blood mononuclear cells (PBMCs) were stimulated with IL-2 and R848 for 72 h prior to sorting. While the memory B cell frequency decreased after stimulation, the frequency of $CD20^{+}CD38^{hi}$ cells increased and the overall number of antibody-secreting cells was increased. When stimulating patient PBMCs for 10 days though, detection of anti-neurofascin-155 (NF155) auto-antibodies in supernatants by enzyme-linked immunosorbent assay (ELISA) was possible in two out of three patient samples. Even though cell sorting was feasible after 10 days of stimulation, detection of auto-antibodies could not be accomplished using antigen-specific ELISpot. Although the implementation of the cell sorting and purification protocol was successful, further adjustments of the antigen-specific ELISpot need to be performed. However, we could show that after 10 days of stimulation auto-antibody detection is possible by ELISA which helps to pre-screen if patient PBMC contain auto-reactive B cells.

CMT1A has an estimated prevalence of 1:5000 and is caused by a duplication of the *peripheral myelin protein 22 kDa (PMP22)* gene. Patients suffer from distal weakness and muscle wasting leading even to wheelchair-dependency in some cases. Although different treatment options for CMT1A have been tested in previous clinical trials, none of them have been successful. In this study, the aim was to identify objective and reproducible outcome measures that assess the actual nerve damage in a large cohort of CMT1A patients by analyzing a series of parameters. Glabrous skin samples were collected from 48 CMT1A, 7 CIDP and 16 small fiber neuropathy patients and 45 healthy controls. 40-µm cryosections from the lateral part of the index finger were double-labeled using immunofluorescence to investigate cutaneous innervation. The disease severity which was assessed using the Charcot-Marie-Tooth Neuropathy Score version 2 (CMTNSv2) and ranged between mild to severe (3-27) correlated with age in CMT1A patients. Furthermore, the intraepidermal nerve fiber density (IENFD) was reduced in CMT1A patients in comparison to controls and correlated negatively with the disease severity. In controls however, the IENFD correlated inversely with age. Meissner corpuscle density tended to be reduced and correlated inversely with age in CMT1A patients. This was not observed in healthy controls though. Compared to controls, Merkel cell density was also reduced in CMT1A, while the fraction of denervated Merkel cell was increased and correlated with

age. Further differences were revealed concerning the node of Ranvier. Paranodes were shortened and the fraction of long nodes was decreased in CMT1A patients compared to controls.

These data suggest that the IENFD, the Meissner corpuscle and Merkel cell densities are possible candidates for outcome measures as they are associated with disease severity or age of patients. However, a reliable statement about the suitability as a marker for disease progression can not be made in this study since only six CMT1A patients agreed to give a follow-up biopsy two years later.

Zusammenfassung

Polyneuropathien können Patienten schwer betreffen. Krankheitsursachen sind vielfältig, können jedoch in zwei Hauptgruppen unterteilt werden. Sie können erworben oder genetisch bedingt sein. Beispiele für diese zwei Klassen sind die chronisch inflammatorische demyelinisierende Polyradikuloneuropathie (CIDP) und Charcot-Marie-Tooth-Erkrankung Typ 1A (CMT1A).

CIDP hat eine geschätzte Häufigkeit von etwa 1-9:100 000. 5-10% der Patienten dieser pathogenetisch heterogenen Gruppe weisen Auto-Antikörper gegen den Ranvier'schen Schnürring auf und zeigen Symptome, die sich von anderen CIDP-Patienten unterscheiden. Es wurde gezeigt, dass die Behandlung mit Rituximab - einem monoklonalen Antiköper, der $CD20^+$ B-Zellen deletiert - bei der Mehrheit der Auto-Antikörper-assoziierten CIDP-Fälle wirksam ist. Das deutet darauf hin, dass B-Zellen und die produzierten Auto-Antikörper pathogenetisch sein könnten. Frühere Studien liefern Beweise, dass Auto-Antikörper allein Nervenschädigungen verursachen können.
Ziel dieser Studie war es, den Pathomechanismus der Auto-Antikörper *in vivo* zu untersuchen und deren genaue Herkunft zu ermitteln: Um die Pathogenität von Auto-Antikörpern zu ermitteln, wurden Passiv-Transfer-Versuche an Lewis Ratten mit Gesamt-IgG einer Patienten mit anti-CNTN1 IgG4 Auto-Antikörpern durchgeführt. Das IgG wurde mittels eines intrathekalen Katheters, der am thorakalen/lumbalen Abschnitt der Wirbelsäule endete, über eine langzeitige, 3-wöchige Zeitspanne injiziert. Eine frühere Studie unserer Arbeitsgruppe hat gezeigt, dass das IgG derselben Patientin milde pathogenetische Effekte hatte, als diese intraneural in den Ischiasnerv von Lewis Ratten appliziert wurden. In dieser Studie jedoch konnten keine Bindungen von Auto-Antikörpern an die Nervenwurzel ermittelt werden. Patienten-Tiere zeigten keine Unterschiede zu Tieren auf, die mit Kontroll-IgG behandelt wurden, weder in der Untersuchung von elektrophysiologischen Eigenschaften nach der Injektionszeit noch bezüglich motorischer und sensorischer Fähigkeiten, die auch während der Injektionszeit getestet wurden. Dies deutet darauf hin, dass anti-CNTN1 Auto-Antikörper keinen pathogenetischen Effekt bei Anwendung des chronischen, intrathekalen Protokolls hatten.

In peripherem Blut wurden vier B-Zell-Subgruppen beschrieben, die fähig sind, Antikörper zu produzieren: Gedächtnis-B-Zellen, Plasmablasten, B1-Zellen und $CD20^{+}CD38^{hi}$ B-Zellen. Um die Auto-Antikörper-produzierenden B-Zell-Subtypen zu identifizieren, wurden Protokolle zur Anreicherung und zum Sortieren sowie zum ELISpot für IgG und IgM erfolgreich etabliert. Da die Produktion von IgG- und IgM-Antikörpern in unstimulierten B-Zell-Subtypen sehr gering war, wurden mononukleäre Zellen des peripheren Blutes (PBMCs, *peripheral blood mononuclear cells*) mit IL-2 und R848 vor dem Sorten für 72 h stimuliert. Während die Häufigkeit von Gedächtnis-B-Zellen nach der Stimulation abnahm, ist die Häufigkeit von $CD20^{+}CD38^{hi}$ B-Zellen gestiegen und die Gesamtzahl an Antikörper-sezernierenden Zellen hat zugenommen. Wurden Patienten PBMCs jedoch für 10 Tage stimuliert, konnten Auto-Antikörper in Überständen mittels ELISA in zwei von drei Patientenproben ermittelt werden. Obwohl das Sorten nach 10-tägiger Stimulation immernoch durchführbar war, war die Detektion von Auto-Antikörper durch antigenspezifischen ELISpot nicht erfolgreich. Trotz der gelungenen Etablierung der Anreicherungs- und Sortierungsprotokolle müssen weitere Einstellarbeiten am antigenspezifischen ELISpot-Protokoll vorgenommen werden. Trotzdem konnten wir zeigen, dass die Detektion von Auto-Antikörpern nach 10-tägiger PBMC-Stimulation mittels ELISA möglich ist, was dabei hilft zu ermitteln, ob Patienten-PBMCs auto-reaktive B-Zellen enthalten.

CMT1A hat eine geschätzte Häufigkeit von etwa 1:5000 und wird durch eine Duplikation des *PMP22*-Gens (*peripheral myelin protein 22 kDa*) verursacht. Patienten leiden unter distaler Schwäche und Muskelschwund, was in manchen Fällen sogar zu Rollstuhlabhängigkeit führen kann. Obwohl verschiedene Behandlungsmöglichkeiten für CMT1A in früheren Studien getestet wurden, ist keine von ihnen erfolgreich gewesen.
Das Ziel dieser Studie war es, objektive und reproduzierbare Outcome-Parameter, die den tatsächlichen Nervenschaden bemessen, in einer großen Kohorte von CMT1A-Patienten zu identifizieren, wozu eine Reihe an Parametern analysiert wurde. Von 48 CMT1A-, 7 CIDP- und 16 *small fiber neuropathy*-Patienten und 45 gesunden Kontrollen wurden unbehaarte Hautproben der lateralen Region des Zeigefingers entnommen. An diesen wurden Doppelfluoreszenzfärbungen vorgenommen, um die kutane Innervation zu untersuchen.

Der Krankheitsgrad der CMT1A-Gruppe, der durch den Charcot-Marie-Tooth Neuropathy Score version 2 eingestuft wurde, erstreckte sich von mild bis schwer (3-27) und korrelierte mit dem Alter der Patienten. Zudem war die intraepidermale Nervenfaserdichte (IENFD) reduziert in CMT1A-Patienten im Vergleich mit gesunden Kontrollen und korrelierte invers mit dem Krankheitsgrad der Patienten. In gesunden Kontrollen korrelierte jedoch die IENFD invers mit dem Alter. Die Dichte der Meissner-Körperchen neigte zu Abnahme in CMT1A-Patienten und korrelierte negativ mit deren Alter, was nicht in gesunden Kontrollen beobachtet wurde. Im Vergleich mit gesunden Kontrollen war die Dichte der Merkel-Zellen ebenfalls verringert in CMT1A, während der Anteil von denervierten Merkel-Zellen erhöht war und mit dem Alter korrelierte. Weitere Unterschiede wurden am Ranvier'schen Schnürring festgestellt. Paranodale Regionen waren verkürzt und der Anteil von langen Schnürringen war erhöht in CMT1A-Patienten im Vergleich zu den Kontrollen.

Diese Daten deuten darauf hin, dass die IENFD, die Dichten der Meissner-Körperchen und Merkel-Zellen potentielle Kandidaten für Outcome-Parameter sind, da sie entweder mit dem Krankheitsgrad oder dem Alter zusammenhängen. Jedoch kann in dieser Studie keine verlässliche Aussage über die Eignung dieser Parameter als Marker für den Krankheitsfortschritt gemacht werden, da zwei Jahre später nur sechs CMT1A-Patienten zu einer Folgebiopsie eingewilligt haben.

1 Introduction

1.1 Node of Ranvier

Saltatory conduction in myelinated nerve fibers requires the proper function of nodes of Ranvier. The node of Ranvier is a highly organized structure which anchors the loops of the myelin sheath to the axon and specifically clusters voltage-gated sodium (Na_V) and voltage-gated potassium (K_V) channels. This organization is crucial for accurate action potential propagation (Rasband et al., 2016). There are three compartments of the node of Ranvier: nodal, paranodal and juxtaparanodal regions. Each of these compartments can be characterized by clustering of specific proteins and their corresponding functions (Stathopoulos et al., 2015):

In the peripheral nervous system, Na_V and K_V channels (predominantly $Na_V1.6$ and $K_V7.2/7.3$) are clustered at the nodal region and interact with the neural, intracellular AnkyrinG. AnkyrinG in turn is connected to the cytoskeleton through βIVspectrin (Berghs et al., 2000; Pan et al., 2006). The axonally expressed cell adhesion molecule neurofascin-186 (NF186) binds to both AnkyrinG and Na_V channels (Davis et al., 1996). NF186 extracellularly binds neuronal cell adhesion molecule (Nr-CAM, expressed in axons and Schwann cells) and interacting with the glial Gliomedin, they form a complex which attaches the axon to the Schwann cell microvilli (Feinberg et al., 2010). The nodal region is enclosed by two hemiparanodes. At the paranodes, cell adhesion molecules interact as septate-like junctions and anchor the myelin sheath to the axolemma. This forms a barrier that separates nodal from juxtaparanodal ion channels and prevents them from diffusion (Rosenbluth, 2009). The cytoskeleton of the paranodal region is formed by AnkyrinB, αIIspectrin, βIIspectrin and protein 4.1B. Together with CNTN1, contactin-associated protein 1 (Caspr) forms an axonal complex which is stabilized by 4.1B (Susuki et al., 2008). Extracellularly, the Caspr/CNTN1 complex binds NF155 - the glial isoform of NF186 - which functions as the junction between the myelin loops and the axon (Boyle et al., 2001; Charles et al., 2002). The complex formation between Caspr and CNTN1 is important for their proper localization to the paranode (Bhat et al., 2001). The axo-glial junction - formed by these three proteins - is crucial for the architecture of the node of Ranvier as shown in paranodal protein-deficient mice. When Caspr, CNTN1 or NF155

were deleted, failure of proper node formation occurred which caused slowing of nerve conduction velocities (Bhat et al., 2001; Boyle et al., 2001; Pillai et al., 2009). Furthermore, it has been reported that the architecture of nodes of Ranvier was changed in patients with demyelinating neuropathies, such as Charcot-Marie-Tooth disease (CMT) or CIDP (Doppler et al., 2013; Li et al., 2005; Saporta et al., 2009). In the third compartment - the juxtaparanode - $K_V1.1$ and $K_V1.2$ channels are clustered. The cell adhesion molecule Caspr2 is anchored to protein 4.1B which links it to the cytoskeleton (Horresh et al., 2010). Caspr2 forms a complex with the axonal cell adhesion molecule contactin-2 and together they bind extracellularly to glial contactin-2. This axon-glia interaction is required for proper K_V1 channel clustering at the juxtaparanode (Poliak et al., 2003; Traka et al., 2003).

1.2 Skin innervation

The skin consists of two main layers, the epidermis and the dermis. Glabrous skin - found on palms and soles - has distinct features from hairy skin. For instance, it is devoid of hair follicles but contains other types of mechanoreceptors: Merkel cells, Meissner corpuscles, Pacinian corpuscles and Ruffini endings (Abraira et al., 2013). Cutaneous nerve fibers can be both myelinated and unmyelinated. Myelinated fibers are more abundant in glabrous skin than in hairy skin (Doppler et al., 2013; Provitera et al., 2007). It has been demonstrated that all myelinated nerve fibers in the dermis are thinning large Aβ-fibers, while thinly myelinated Aδ-fibers lose their myelin sheath when entering the dermis which makes them undistiguishable from small unmyelinated C-fibers (Provitera et al., 2007). Their localization and involvement in mechanoreceptor innervation differ. While only free nerve endings from unmyelinated C-fibers and thinly myelinated Aδ-fibers penetrate the epidermis as intraepidermal nerve fibers, large myelinated Aβ-fibers do not. However, they are involved in the innervation of mechanoreceptors (Abraira et al., 2013).
Merkel cells are present as touch domes around hair follicles in hairy skin. In glabrous skin though, they are more scarce and located at the epidermal-dermal junction (Woo et al., 2015). Merkel cell survival is dependent on their innervation by free nerve endings from large myelinated Aβ-fibers (Airaksinen et al., 1996). Another mechanoreceptor type, the Meissner corpuscles, are located in the papillae (dermal protrusions into the

epidermis) and can only be found in glabrous skin (Vega et al., 2013). Usually, they are innervated by one to two large myelinated Aβ-fibers and several small unmyelinated nerve fibers which are wrapped around a bulb of lamellar non-myelinating Schwann cells (Nolano et al., 2003).
Cutaneous innervation can be very well investigated using skin punch biopsy, a valuable minimally invasive tool (Doppler et al., 2013; Lauria et al., 2009; Sommer, 2008). Especially the IENFD has been established as a useful measure to detect deterioration of small nerve fibers (Collongues et al., 2018; Lauria et al., 2005; Pereira et al., 2016).

1.3 B lymphocytes

B lymphocytes play an important role in the adaptive immune system as they produce immunoglobulins (Igs) against pathogens, interact with T cells (antigen presentation and co-stimulation) and secrete cytokines. Such as T cells, they are derived from hematopoietic stem cells. However, they differentiate exclusively in the bone marrow which they leave when they have developed into immature, naive B cells (Perez-Andres et al., 2010). In the bone marrow the first line of B cell tolerance is established: Pro-B cells experience somatic recombination and assembly of their V (variable), D (diversity) and J (joining) gene segments of the Ig heavy-chain locus. After the Ig heavy chain is expressed pre-B cells exhibit a pre-B cell receptor (BCR) by expressing a surrogate light chain. Pre-B cells then experience positive selection if their pre-BCR is capable to bind to the microenvironment of the bone marrow which ensures functionality of the heavy chain. If they fail they undergo apoptosis. Following positive selection, the now immature B cells express light chain proteins which interact with the heavy chain forming a IgM-BCR on the cell surface. Binding of the BCR to self-antigens presented in the bone marrow induces receptor editing - rearrangements of light chain gene segments to form a new BCR - cell apoptosis or anergy. This negative selection process prevents auto-reactive B cells to leave the bone marrow and ensures central tolerance (Nemazee, 2017). Immature B cells that prove innocuous can leave the bone marrow as naive immature B cells that express surface IgM and IgD (Nemazee, 2017; Perez-Andres et al., 2010).
Naive immature B cells which are cluster of differentiation (CD)19^{+}CD20^{+}CD27^{-}CD38^{-} patrol between the peripheral blood and the lymph nodes until they encounter their cog-

nate antigen, otherwise they die within several days. When naive B cells find their antigen which is presented by follicular dendritic cells in lymph nodes they are activated by T cells and migrate into germinal centers. There, B cells experience high proliferation, somatic hypermutation and class switch recombination which result in a BCR with high affinity. After this process, which is called affinity maturation, $CD27^+$ memory B cells patrol the body and are able to respond to their cognate antigen T cell independently. Plasma cells however migrate into the bone marrow and secrete antibody. There, plasma cells can persist for several decades (Cassese et al., 2003; Höfer et al., 2006).

In mice, it is well described that there is another B cell lineage - B1 cells - with distinct functions and development. B2 cells are the conventional, antigen-specific lineage which were described above whereas B1 cells constitute an innate-like B cell population (Baumgarth, 2011). Murine B1 cells are phenotypically characterized as $CD5^+$. In contrast to B2 cells, they develop during ontogeny and are most abundant in the peritoneal cavity and pleural space. B1 cells spontaneously secrete protective natural antibodies, mainly from the IgM and IgA isotypes. Natural antibodies are important for microbial pathogen defense but also for debris-clearing homeostasis (Rothstein et al., 2013). In contrast to B2 cells, B1 cells do not experience affinity maturation. As a result, B1 cell antibodies show low affinity but broad cross-reactivity. Failure of maintaining the anergic state of self-reactive B1 cells might lead to auto-immune interactions (Sindhava et al., 2012).
In recent years, the B1 cell population has also been described in humans by *Rothstein and colleagues* (Griffin et al., 2011; Quách et al., 2016; Rothstein et al., 2013; Sindhava et al., 2012). However, it is still controversially discussed if this cell population is indeed constituting a human B1 cell lineage (Covens et al., 2013; Inui et al., 2015; Li et al., 2013; Tangye, 2013) and has been proposed to be pre-PBs, instead (Covens et al., 2013). The latest publication addressing the issue delivered evidence that human B1 cells might actually exist (Quách et al., 2016).

In humans, the most convenient source for B cells is peripheral blood. *Quách et al* investigated four B cell subpopulations with distinct surface marker expression in peripheral blood that are capable of antibody secretion: memory B cells, PBs, B1 cells and the

newly identified $CD20^{+}CD38^{high}$ cells (Quách et al., 2016). Since this classification is rather new, there are more established B cell classification systems. For instance, the memory B cell classification by the expression of IgD and CD27 has been widely used (Klein et al., 1998; Moura et al., 2017). Treatment of different auto-immune diseases with the B cell-depleting monoclonal antibody targeting CD20, rituximab, reflects the pathogenic relevance of B cells (Berghen et al., 2019; Lee et al., 2016; Lindholm et al., 2008; Querol et al., 2015). Even though treatment with rituximab is often beneficial and well tolerated, some severe adverse effects may occur after treatment such as infections, persistent leukopenia or even death (Damato et al., 2016; Kasi et al., 2012).

1.4 Peripheral neuropathies

Damage of peripheral nerves can manifest in sensation and movement impairment, depending on the affected nerves. Neuropathies can be classified by their affected nerve structures. Damage or disruption of the myelin sheath – therefore called demyelinating – usually leads to conduction velocity reduction whereas damage of the axon – called axonal – results in decreased amplitudes of action potentials (Schafflick et al., 2017; Weis et al., 2016). Nerve damage can be caused by various reasons. There are two main groups in which these causes can be divided: hereditary neuropathies and acquired neuropathies. The most common hereditary neuropathy is the Charcot-Marie-Tooth neuropathy (Mygland et al., 2001; Weis et al., 2016) which will be explained in detail in Chapter 1.4.1. Acquired neuropathies can be caused by diseases such as diabetes, but also by toxins such as chemotherapeutic agents or alcohol, for instance (Mygland et al., 2001; Weis et al., 2016). However, we will focus on one of the most prevalent immune-mediated chronic neuropathies (Schafflick et al., 2017), namely the CIDP which will be introduced in Chapter 1.4.2.

1.4.1 Charcot-Marie-Tooth 1A disease

CMT disease – also known as hereditary motor and sensory neuropathy (HMSN) – is the most common hereditary peripheral neuropathy with an estimated prevalence of 1:2500 (Weis et al., 2016). It can be caused by a variety of genetic mutations leading to a very heterogenous clinical picture. In this disease group both types, demyelinating and

axonal types, can be found and are therefore classified as type CMT1 (demyelinating) and CMT2 (axonal), but also intermediate types occur (Weis et al., 2016). The most common CMT subtype is the demyelinating CMT1A which is caused by a duplication of the gene *PMP22* on chromosome 17. Almost most half of all CMT cases belong to the CMT1A subtype which results in an overall occurrence of about 1:5000 (Gess et al., 2013; Manganelli et al., 2014). This autosomal-dominantly transmitted mutation results in a 1.5-fold overexpression of the PMP22 protein (Lee et al., 2018), one of the main myelin proteins (Snipes et al., 1995), leading to demyelination, reduced nerve conduction velocity and length-dependent axonal degeneration (Pareyson et al., 2006). After disease onset - typically in the first decades of life - CMT1A patients predominantly suffer from muscle weakness and wasting, mostly in the lower limbs, which can lead to foot deformities (Pareyson et al., 2006) and in some cases even wheelchair dependency (Van Paassen et al., 2014).

Although the consequences of CMT1A can be extensive no causative treatment has been approved yet. At present, CMT1A patient are treated with physical therapy, pain medication or orthopedic surgeries (Schenone et al., 2011).

However, there have been clinical trials testing drugs already approved for other diseases. The triplet medication PLX3003 composed of baclofen, naltrexone and sorbitol had a small beneficial over placebo (Attarian et al., 2014). Other clinical trials investigating the effect of ascorbic acid on CMT1A disease could not detect beneficial effects (Gess et al., 2015; Lewis et al., 2013; Micallef et al., 2009; Pareyson et al., 2011). In these trials, primary outcome measures to evaluate disease severity and progression were mainly disease scores, such as the Charcot-Marie-Tooth Neuropathy Score (CMTNS) (Shy et al., 2005) or the Overall Neuropathy Limitation Scale (ONLS) (Graham et al., 2006), which represent mostly clinical and functional parameters. Critical discussion about improvements of these scores has lead to adaptation to the CMTNSv2, for instance (Murphy et al., 2011). Also, additional secondary outcome measures have been proposed such as the 9-hole-peg or the foot dorsal tests (Mannil et al., 2014).

Other groups suggested other candidates for potential biomarkers in CMT1A: several groups have investigated *PMP22* messenger ribonucleic acid (mRNA) levels in skin from CMT1A patients (Fledrich et al., 2012a; Katona et al., 2009; Nobbio et al., 2014) but

they did not correlate with disease severity in all of the cited studies. *Nobbio et al.* concluded that *PMP22* mRNA levels are not a suitable biomarker for CMT1A since they did not correlate with clinical and electrophysiological scoring measures (Nobbio et al., 2014). *Fledrich et al.* also tested mRNAs encoding other genes and identified a cluster of five gene transcripts expressed in the skin that present as a suitable series of biomarkers in CMT1A (Fledrich et al., 2017). Furthermore, measurements of intramuscular fat by magnetic resonance imaging have been tested in their suitability as outcome measures and revealed promising results as the fat accumulation correlate with parameters assessing the disease severity in CMT1A (Cornett et al., 2019; Morrow et al., 2016). Recently, neurofilament light chain levels in the plasma of CMT1A patients have been shown to correlated with disease severity (Sandelius et al., 2018). Neurofilament proteins are important scaffolding proteins specifically in neurons. Nerve damage leads to the release of these proteins into the cerebrospinal fluid or the plasma (Khalil et al., 2018). Neurofilament light chain concentrations might be therefore suitable to assess the nerve damage in CMT1A accordingly. However, no conclusions about the damaged nerve fibers - such as their calibers or whether they are myelinated - can be drawn.

Animal models for CMT1A

CMT1A disease and therapeutic approaches have also been studied in rodent models. Three rodent models have been generated with low copy numbers of the *Pmp22* gene which show a CMT1A typical phenotype, demyelination and nerve conduction slowing (Fledrich et al., 2012b). The *Pmp22*-transgenic rat, the so-called 'CMT1A rat', carries three additional copies of the murine gene (Sereda et al., 1996) and has been extensively examined (Fledrich et al., 2012a; Fledrich et al., 2014). Furthermore, different therapeutic approaches have been tested, such as progesterone treatment (Sereda et al., 2003), administration of PTX3003 (Prukop et al., 2019) or treatment with antisense oligonucleotides (Zhao et al., 2018), all of which had beneficial effects in the CMT1A rat. The mouse strains C3 (Verhamme et al., 2011) and C61 (Huxley et al., 1996), both with four additional human *Pmp22* gene copies, also show CMT1A-like phenotpyes. It has been shown that the disease severity correlates with the gene copy number and therefore the PMP22

expression in transgenic mouse strains. For instance, the C22 mice, which carry seven extra copies of the human gene, show a more pronounced neuropathic phenotype than C3 or C61 mice (Huxley et al., 1998; Verhamme et al., 2011) and are usually considered a model for Déjerine Sòttas syndrome (Fledrich et al., 2012b). However, this classification appears not be strictly distinctive since several studies have used C22 or Trembler-J mice as a model for CMT1A (Devaux et al., 2005; Passage et al., 2004; Zhao et al., 2018), in which pathology and treatment options have been tested.

Cutaneous innervation in CMT1A

Studies investigating skin biopsies in CMT1A revealed reduced cutaneous innervation. In comparison to healthy controls, IENFD has been shown to be decreased in glabrous and hairy skin (Duchesne et al., 2018; Nolano et al., 2015). Large myelinated fibers have also been reported to be reduced in skin biopsies of CMT1A patients (Li et al., 2005). Furthermore, Meissner corpuscle density has been shown to be decreased in CMT1A patients at different sites of the hand using skin biopsy or *in vivo* confocal microscopy. Correlation analyses between Meissner corpuscle density and disease severity were not consistent between these studies (Almodovar et al., 2011; Manganelli et al., 2015; Nolano et al., 2015; Saporta et al., 2009). Merkel cell density has not been investigated in CMT1A patients to our knowledge. However, in P0-deficient mice, a model for CMT1B, it has been shown that Merkel cell density was reduced (Frei et al., 1999). Furthermore, the architecture of the node of Ranvier has been investigated using skin biopsy in CMT1A. Paranodal shortening and an increase of the asymmetry index has been reported (Saporta et al., 2009). These studies provide evidence that the investigation of cutaneous innervation using skin biopsy is useful. However, each of these studies only analyzed single parameters or had small cohorts.

1.4.2 Chronic inflammatory demyelinating polyradiculoneuropathy

CIDP comprises a very pathogenetically heterogeneous patient group. This immune-mediated neuropathy shows a prevalence of 1-9 per 100 000. Typical symptoms are motor and sensory dysfunction leading to proximal and distal weakness that persist at least 8 weeks (Mathey et al., 2015). CIDP is predominantly diagnosed based on nerve conduction studies (Dalakas, 2011). A subset of CIDP patients present with auto-antibodies against proteins of the node of Ranvier. This subgroup has been recently identified and patients suffer from distinct symptoms (Vural et al., 2018). Various groups have identified auto-antibodies against NF155, CNTN1 and Caspr in CIDP patients (Doppler et al., 2016; Doppler et al., 2018; Kawamura et al., 2013; Ng et al., 2012; Querol et al., 2013). These so-called 'seropositive' patients (Vural et al., 2018) usually fulfill electrophysiological criteria of CIDP (reduced nerve conduction velocity, conduction block and extended distal motor latency). However, nerve biopsies do not show onion bulb formation or thinly myelinated fibers, which are classical signs for de-/remyelination (Doppler et al., 2016; Doppler et al., 2015; Ogata et al., 2015). Most seropositive patients respond well to rituximab treatment which is a monoclonal antibody directed against CD20, a B cell specific cluster of differentiation (Franks et al., 2016; Vural et al., 2018). Responses to intravenous Igs, plasma exchange or steroids are not uniform and might depend on the target proteins of auto-antibodies. Successful treatment can lead to improvement of clinical symptoms (Vural et al., 2018). Since not the myelin sheath but structures of the node of Ranvier were the auto-antibodies' target, myelination is not disturbed. Therefore, the term nodopathy has been introduced which describes neuropathies with auto-antibodies attacking nodal and paranodal structures (Uncini et al., 2013). Previously, it has been shown that patients with auto-antibodies to paranodal proteins show nodal lengthening, myelin thinning and detachment of myelin loops in dermal nerve fibers (Doppler et al., 2016; Doppler et al., 2015; Koike et al., 2017). These disturbances of the node of Ranvier are hypothesized to cause the reduction in nerve conduction velocity, conduction block and increased distal motor latency in seropositive CIDP patients (Uncini et al., 2018). It has been reported, that in contrast to seronegative patients, seropositive patients did not show macrophage involvement or demyelination in sural nerve biopsies (Doppler et al., 2016; Koike et al., 2017).

In vitro studies investigating the pathomechanisms of paranodal auto-antibodies have revealed that anti-CNTN1 auto-antibodies prevent complex formation of the Caspr/CNTN1 construct to NF155 in a cell aggregation assay. Furthermore, paranodal regions were shortened whereas nodes were elongated in neuron/Schwann cell cultures when treated with patient IgG (Labasque et al., 2014). Another study revealed similar findings (Manso et al., 2019). They reported inhibition of aggregate formation in a cell aggregation assay when incubation with anti-CNTN1 auto-antibodies was performed. However, these alterations did not occur when anti-NF155 from three different patients were tested. However, intraperitoneal injection of anti-NF155 antibodies in P0 mice caused perturbances in paranodal formation and shortened paranodes in P2, which was however restored in P6 mice. This study provides evidence that anti-CNTN1 and anti-NF155 IgG4 auto-antibodies act through different pathomechanisms that result in disturbed paranodal organization (Manso et al., 2019).

However, in adult subjects that develop a seropositive CIDP the node formation and development is already completed. Several previous studies have performed passive transfer experiments in adult Lewis rats in order to decipher the underlying pathomechanisms of paranodal auto-antibodies (Doppler et al., 2019; Manso et al., 2019; Manso et al., 2016). In rats pre-immunized with P2 peptide, anti-CNTN1 IgG4 has been shown to invade the paranodal regions over time predominantly in small motor neurons which manifested in progressive clinical deterioration and ataxia. They proposed that the pathogenicity of IgG4 auto-antibodies might be mediated by blocking of the target protein function, in this case blocking of CNTN1 function (Manso et al., 2016). The same group showed in a following study (Manso et al., 2019) in naive rats, that anti-NF155 IgG4 auto-antibodies from CIDP patients did not pass through the paranodal junction when applied chronically. The antibodies interacted with NF155 in the Schwann cell surface and caused specific depletion of NF155, which in turn prevented paranodal complex formation. Animals showed conduction pertubations in motor nerves and gait abnormalities (Manso et al., 2019). Another study, investigating the effect of anti-CNTN1 auto-antibodies of isotypes IgG3 and IgG4 in short-term focal applications into the naive sciatic nerve revealed antibody deposition at the paranodal regions. Paranodal organization appeared still normal. Rats treated with either IgG subclass showed signs of conduction block.

However, IgG3 treated animals additionally showed complement component C1q deposition at paranodal regions and had gait abnormalities in contrast to IgG4 treated animals, suggesting different pathomechanisms in different IgG isotypes (Doppler et al., 2019). Interestingly, patients with anti-CNTN1 and anti-NF155 present with distinct onset, symptoms and response to treatment (Vural et al., 2018). This is in accordance with findings from passive transfer experiments, where the target-antigen and isotype show different effects.

1.5 Aims of the studies

1.5.1 CIDP projects

Pathogenicity of auto-antibodies

In recent years, it has been proven that auto-antibodies targeting paranodal proteins are associated with a subset of CIDP patients. This subgroup shows distinct clinical features from seronegative patients. The exact pathomechanisms are not clear. Evidence exists that antibodies against different proteins act in different ways. In order to decipher how auto-antibodies destruct the node of Ranvier, passive transfer experiments have been performed. A previous study of our laboratory investigating anti-CNTN1 IgG4 auto-antibodies in a focal, short-term intraneural application revealed only mild effects. It has been reported that in long-term experiments effects are enhanced. Therefore in this study, the pathogenicity of the same anti-CNTN1 IgG4 auto-antibody was investigated in an intrathecal, long-term application *in vivo* as outlined in the following:

- Potential effects on gait, motor performance and sensitivity to mechanical and thermal stimuli were analyzed by behavioral tests throughout the injection period
- Electrophysiological properties were assessed before and after the injection period
- Nerve tissues were analyzed to reveal potential antibody deposition and disorganization of nodal structures

Auto-antibody producing B cells

CIDP patients are often treated with rituximab. Although most patients respond well to this treatment, it interferes immensely with the immune system. Only tissue resident B cells remain after depletion with rituximab, which makes patients susceptible for severe

adverse effects by this treatment. It is not known where B cells, that produce auto-antibodies, are located or which B cell subset secretes them. Possibly, by identification of the auto-antibody-producing B cell subpopulation a more specified treatment option, that is less invasive, might be established in the future. Furthermore, revealing the subset of auto-reactive B cells might enable prognosis of rituximab treatment since $CD20^-$ B cells are not affected.
The aim of this study was therefore the implementation of a protocol in our laboratory that enables to investigate which B cell subset produces auto-antibodies against paranodal proteins in CIDP patients using the following techniques:

- Purification and enrichment of $CD19^+$ B cells from PBMCs by magnetic activated cell separation (MACS)
- Fluorescence activated cell sorting (FACS) sorting to divide antibody-secreting B cell subpopulations
- Establishment of an antigen-specific ELISpot assay

1.5.2 CMT1A project

There is no treatment approved for CMT1A. Clinical trials testing potential medication still lack suitable secondary outcome measures that assess the actual nerve damage and that are more sensitive than neuropathy scores. Previous studies provide evidence that the investigation of cutaneous innervation using skin biopsy is useful in CMT1A. However, as they only analyzed single parameters or had small cohorts, additional and more extensive investigations of larger cohorts are necessary to identify objective and reproducible biomarkers that detect nerve damage. The aim of this study was to identify objective and reproducible outcome measures for future clinical trials in CMT1A by addressing the following issues:

- Identification of cutaneous nerve structures, such as nerve fiber or mechanoreceptor densities, that reflect disease severity in CMT1A patients
- Analysis if nodal and paranodal parameters are suitable to evaluate disease severity in CMT1A patients

- Evaluation if parameters, that have been identified as measures for disease severity, are suitable for assessing disease progression by analysis of follow-up biopsies

2 Material and methods

2.1 Passive transfer experiments

2.1.1 Equipment, buffers and solutions, antibodies

In the appendix, detailed lists of the technical equipment (Appendix 7.1), reagents (Appendix 7.2), buffers and solutions (Appendix 7.3) and staining antibodies (Appendix 7.4) are provided.

2.1.2 Animals

Female, 8-week-old Lewis rats were obtained from Charles River (190 - 230 g, Charles River Laboratories, Sulzfeld, Germany). Before starting the experiments, rats were allowed to acclimate after transportation to our facility for at least one week. After catheterization rats were singly housed. Use and care of animals were in accordance with the institutional guidelines. All experiments were approved by the Bavarian State authorities (Regierung von Unterfranken). Rats were housed in the animal facilities of the Department of Neurology (University Hospital Würzburg) in a 12 hours (h) / 12 h day (<300 lux) / night cycle with access to food and water *ad libitum*.

2.1.3 Intrathecal catheter implantation

Catheter fabrication

For the fabrication of intrathecal catheters, a knot was tied into the middle of a 15 cm piece of PE-10 polyethylene tubing. The knot was fixed with dental cementum. When the cement was dry, the catheters' lumens were checked for patency with 70% ethanol (EtOH) using a 30Gauge (G) canule and stored overnight in a 70% EtOH bath. Before implantation, the insert part of the catheters were shortened to 6.5 cm and the catheters were flushed with 0.9% sodium chloride (NaCl) solution.

Catheter implantation

For the implantation of intrathecal catheters into the spinal subarachnoid space, naive rats were deeply anesthetized with 2.5% isoflurane in a 50% O_2/room air composite. Before placing the heads of the animals into the stereotactical frame, their napes were shaved. After placement into the frame, the rats eyes were covered with eye ointment to protect

them from drying-out.

The implantation of intrathecal catheters was performed under aseptic conditions as described previously (Malkmus et al., 2004). In short, beginning at the edge of the skull (nuchal crest) a lateral incision of about 2 cm was performed in a caudal direction using a No. 15 scalpel. Then the muscle was removed from the skull by gently scraping with the scalpel in the caudal direction. On the shifted muscle, traction was applied using a retractor to prevent damage of the brain stem by putting to much pressure on the atlanto-occipital membrane in the later steps. Further gentle scraping was done to expose the fascia between the skull and the first vertebral body. Under traction of the muscle, the first vertebral body was exposed by further very gentle scpraping, until the first vertebral body could be felt and the membrane between the skull and the first vertebral body (atlanto-occipital membrane) could be seen.

After the exposition of the atlanto-occipital membrane, the dura-hook (a 20G canule whose first 1-2 mm of the tip were bent at 70-80°) was used to make a 2 mm incision into the membrane close to the first vertebral body. An outburst of clear cerebrospinal fluid indicated the penetration of the dura mater. While using the dura hook to open up the incision, a catheter was carefully inserted into the subarachnoid space as parallel as possible to the spinal cord to prevent nerve injury. After inserting the first 1-2 cm of the catheter, the rats' position was changed so that the spine was as straight as possible to facilitate insertion and minimize risk of injury.

When the catheter was fully inserted, the skin of the rats' forehead was punctured using a 20G needle which was used to tunnel the outside part of the catheter from the incision site to the rats forehead. After closing the muscle, fixating the catheter knot and closing the skin incision, 20 µl of 0.9% NaCl was applied using a 30G needle connected to a Hamilton microliter syringe. The catheter was closed with a 0.5 cm long piece of copper wire with a diameter of 0.28 mm.

When rats woke up from anesthesia, they were checked for motor deficits resulting from nerve injury during catheter insertion. Rats showing motor deficits were sacrificed immediately. Rats without motor deficits were allowed to recover for at least one week until behavioral testing and IgG injections. After implantation of catheters, rats were examined and scored daily. Before passive transfer injections, catheters were flushed with 20 µl

NaCl to prevent clogging three times a week.

2.1.4 Whole IgG passive transfer

Purification of IgG

For passive transfer experiments purified whole IgG from a female, 68-year-old CIDP patient with a high titer of anti-CNTN1-antibodies was used. The patient's clinical details were previously described (Doppler et al., 2015). The patient's serum had a high titer of IgG4 auto-antibodies (1:15000) and lower titers of the other IgG isotypes (IgG3: 1:5000, IgG2: 1:1000, IgG1: 1:500) as determined by ELISA for other studies (Doppler et al., 2019; Doppler et al., 2015). As negative control, purified whole IgG from a patient with optical neuritis without evidence of auto-antibodies was used.

IgG was purified from material obtained from therapeutic plasma exchange by exchange chromatography by Susanne Hellmig (AG Schuhmann, Neurologische Klinik, Würzburg). The purification process was previously described (Sommer et al., 2005). Lyophilised IgG was dissolved in 0.9% NaCl solution at a concentration of 100 mg/ml and stored at -20°Celsius (C) until use.

Intrathecal IgG injection

Intrathecal injection of IgG was performed as depicted in the timeline in Figure 1. Daily injections for five days were followed by five injections applied every other day. The last two injections were applied with two days of break in between. The last injection was always applied the day before tissue harvesting. When rat cohorts were larger than six rats, tissue harvesting was performed on two days, day 20 and day 21, due to time and logistical reasons. In case of tissue harvesting on day 20, the behavioral testing and the last IgG injection was performed on the previous day.

IgG injection was performed while the rats were fixated by an investigator. Another investigator removed the plug from the catheter and applied 10 µl of IgG (100 mg/ml) directly followed by injection of 10 µl of NaCl solution to flush the catheter. After the plug was re-inserted, the rat was released.

The investigators were blinded for the patient/control conditions. Rats were randomly divided into two groups. The blinded conditions were not disclosed until all experiments and tissue harvesting were finished.

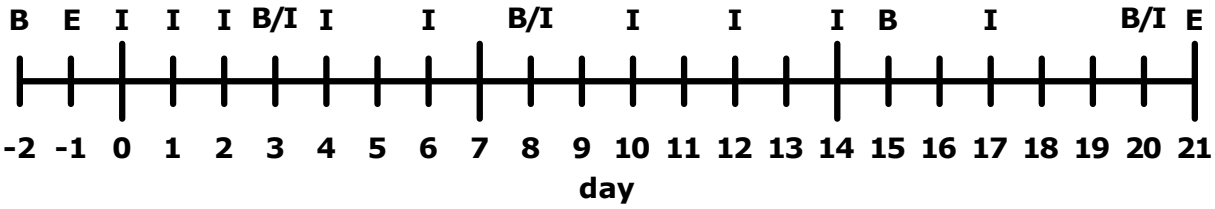

Figure 1: Timeline of intrathecal injections and testing. Before IgG injections, baseline behavioral testing and nerve conduction measurements were performed. After five days of daily injections, five injections were applied every other day followed by two more injections with 2 days of break. Behavioral testing was performed on days 3, 8, 15 and 20 after the first injection day. Nerve conduction measurements were performed immediately before tissue harvesting on day 21. B: Behavioral testing, E: Nerve conduction studies, I: IgG injection.

Intrathecal EBD injection

A 1% Evans Blue dye (EBD) solution was prepared by mixing 0.5 g of EBD with 50 ml Dulbecco's phosphate buffered saline (DPBS), and subsequent filtering through a 0.2 µm filter. 10 µl of the EBD solution was injected intrathecally through the catheter, which was flushed immediately with 10 µl NaCl solution. Tissue harvesting was performed 16 h after injection to evaluate the uptake of the dye into the spinal cord, nerve roots and peripheral nerves.

2.1.5 Behavioral testing

All animals were tested four times before catheter implantation to allow the rats to get used to the testing procedure. After the recovery time from surgery, they were tested again three to four times to allow them again to get used to the testing procedure before obtaining baseline values. Behavioral testing was then performed at day 3, 8, 15 and 19/20 of the 3-week passive transfer period before sacrificing them on day 20/21. When animal groups were larger than 6, the groups were split and sacrificed on two days (days 20/21) due to time and logistic reasons.

Gait analysis

For gait analyses the Noldus CatWalk^{TM} XT system which is a tool for automated gait assessment and evaluation in rodents using the Illuminated Footprint^{TM} technology was used. It is based on internal reflection of a green LED light in a glass plate. When animals, that are placed on the plate, touch the glas, the light gets transmitted and can be recorded with a camera. The rats were allowed to freely move on the CatWalk^{TM} XT

until three valid runs were recorded. A run was valid when the run duration was 0.5 - 5 seconds (sec) long and the run speed variation did not exceed 60%. The foot print area, the standing time and the maximum intensity of the hind paws were calculated. The mean values per parameter per test day were averaged for analysis.

Motor performance test

The rotarod performance test was used to determine motor function and endurance using a TSE RotaRod Advanced. Rats were placed individually on the rod. After an adaptation time of 10 sec with constant speed of 5 revolutions per minute (rpm), the speed of the rotating rod accelerated from 5 rpm to 50 rpm within 500 sec. Rats were tested three times and the fall latencies were recorded and averaged for analysis.

Mechanical sensitivity

Von-Frey testing based on the up-and-down method (Chaplan et al., 1994) was used to determine mechanical sensitivity of the hind paws. Rats were individually placed in acrylic glass boxes on a wire mesh grid. After adaptation to the environment for 15 minutes (min), pressure on the lateral plantar surface of the left and right hind paws (i.e. sural nerve innervation territory) was applied for 3 sec using a von-Frey filament with 5.18 g. If the rat withdrew its hind paw, the filament with the next-smaller diameter was used to test the paw. If the rat did not withdraw, the next-larger filament was used to apply pressure. For each hind paw, pressure was applied six times. The 50% withdrawal threshold describes the force of the von-Frey filament to which an animal responds in 50% of applications. This threshold was determined for analysis.

Thermal sensitivity

The Hargreaves test was performed to determine thermal sensitivity. Rats were individually placed in acrylic glass boxes on a glass surface. After adaptation to the environment for 15 min, heat stimuli on the lateral plantar surface of the left and right hind paws were applied using a Ugo Basile Algometer. The intensity of the infrared radiation (the radial heat stimulus) was set to 40 (range of infrared intensity 0-99). The heat stimulus was applied for a maximum of 20 sec to prevent heat damage. Each hind paw was tested three

times and withdraw latencies were recorded and averaged for analysis.

2.1.6 Nerve conduction studies

Rats were anesthetized with an intraperitoneal injection of a mixture of xylavet (xylazine: 8 mg per kg body weight) and ursotamin (ketaminhydrochloride: 100 mg per kg body weight). For nerve conduction measurements, rats were placed under a heating lamp to prevent hypothermia and their body temperature was measured before and after measurements. Recordings and measurements of nerve conduction features of the right sciatic nerve were performed as described previously (Zielasek et al., 1996). Briefly, monopolar needle electrodes were placed at the sciatic notch (proximal) and at the ankle (distal) for stimulation; recording electrodes were placed in the hind paw. Compound muscle action potential (CMAP) amplitudes [mV] were recorded after supramaximal stimulation at the proximal and distal site. Proximal, distal and F-wave latencies [ms] were measured. In addition, the distance between the proximal and distal stimulation sites was measured to determine the nerve conduction velocity (NCV) [m/s]. A digital Neurosoft-Evidence 3102 electromyograph was used to perform neurographic recordings.

2.1.7 Dissection and tissue processing

The brain, the cervical, thoracic, lumbar regions of the spinal cord, nerve roots and dorsal root ganglia of L3-5 and the sciatic nerve were harvested after rats were killed by decapitation while anesthetized with a ursotamin-xylavet mixture after nerve conduction measurements.

The brain, the spinal cord, root ganglia, nerve roots from the right side and one part of the sciatic nerve were embedded in Tissue-Tek® O.C.T. compound and frozen in methyl butane which had been pre-cooled with liquid N_2. Frozen tissue was stored at -80°C until further processing.

For single teased fiber preparations of the sciatic nerve and the anterior and posterior nerve roots, nerves were incubated in 4% paraformaldehyde (PFA) for 10 min at room temperature (RT) and washed three times with phosphate buffer. Nerves were stored at 4°C until teasing which was done the day after dissection at the latest. The perineurium was removed and single nerve fibers were separated on glass slides with forceps. Teased

fibers were let dry and stored at -20°C until staining.

2.1.8 Immunohistochemistry

Frozen teased fiber preparations were thawed at RT and fixed with acetone at -20°C for 10 min. After washing with phosphate buffered saline (PBS) the tissue was blocked with blocking solution (4% normal goat serum, 4% fetal calf serum (FCS), 0.3% Triton X-100 in PBS) at RT for 1 h. Primary antibodies were diluted in blocking solution accordingly and incubated overnight at 4°C. After washing with PBS, suitable fluorophore-conjugated secondary antibodies were diluted in blocking solution and incubated at RT for 2 h. Specimens were mounted with Vectashield mounting Medium with DAPI.

2.2 B lymphocyte study

2.2.1 Equipment, buffers and solutions, antibodies

In the appendix, detailed lists of the technical equipment (Appendix 7.1), reagents (Appendix 7.2), buffers and solutions (Appendix 7.3) and staining antibodies (Appendix 7.4) are provided.

2.2.2 Isolation of peripheral blood mononuclear cells

PBMCs were isolated either from leukoreduction system chambers (LRSCs) or from ethylenediaminetetraacetic acid (EDTA)-treated whole blood using density gradient centrifugation. In LRSCs, concentrates of leukocytes are collected which are obtained as the byproduct of apheresis for thrombocyte collection. We received LRSCs from anonymous donors from the Institute for Transfusion Medicine of the University Hospital Würzburg. From CIDP patients with auto-antibodies, we received EDTA-treated whole blood. Leukocyte-enriched blood product from LRSCs was diluted 1:10, while whole blood was diluted 1:2 with DPBS at RT. 30 ml of diluted blood suspension was carefully layered over 15 ml of the density gradient medium Lymphoprep^{TM} per 50 ml falcon tube. The medium/blood layering was centrifuged at 600 xg for 30 min without brake at RT. The white mononuclear cell layer was carefully transferred into a new 50-ml falcon tube using a transfer pipette. The cell suspension was filled up to 50 ml with 4°C cold DPBS. The cell suspension was washed by centrifugation at 300 xg for 20 min at 4°C. The supernatant was carefully aspirated, the cell pellet mobilized and resuspended in 50 ml of 4°C

DPBS. Once more, the cells were centrifuged as described before. The pellet was mobilized and resuspended in 10 ml of 4°C cold DPBS. The cell number was determined using a Neubauer counting chamber and trypan blue dead cell staining under an OLYMPUS CKX41 inverted light microscope.
10^7 PBMCs were resuspended in 1 ml of pre-cooled freezing medium, consisting of FCS with 10% dimethyl sulfoxide (DMSO), and transferred into pre-cooled cryotubes. They were immediately placed in a pre-cooled cell freezing container and stored at -80°C. After 24 h the cryotubes were stored in liquid N_2 for at least a week until thawing.

2.2.3 PBMC thawing and stimulation

Thawing

For PBMC thawing, the protocol from R. S. Hansen (Hansen, 2011) was adapted: PBMCs were thawed in a 37°C water bath. The cells were transferred into a 50-ml falcon tube and diluted step by step with pre-warmed cell culture medium (1640 RPMI with glutamin, 10% FCS, 1% penicillin/streptomycin) as follows: 1 ml, 2 ml, 8 ml, 20 ml and filled up to 50 ml. After each dilution step, falcon tubes were gently swiveled and incubated at RT for 3 min. Then cells were centrifuged at 300 xg for 15 min at RT. The supernatant was carefully aspirated, the cell pellet mobilized and resuspended in 10 ml of warm cell culture medium. The previous centrifugation step was performed once more. The pellet was resuspended in 10 ml of cell culture medium and once again centrifuged as described before. The pellet was resuspended in 10 ml of cell culture medium and filtered using a 30-µm mesh filter. The cell number was determined using a Neubauer counting chamber and trypan blue dead cell staining under a light microscope.
When PBMCs were not stimulated but further processed immediately, they were incubated for 1 h at RT to equilibrate.

Stimulation

For stimulation of B cells, PBMCs were resuspended in stimulation medium (cell culture medium containing 15 ng/ml interleukin-2 (IL-2) and 2.5 µg/ml resiquimod (R848)) at a concentration of 3x10^6 cells/ml. Cells were incubated for 72 h or 10 days at 37°C and 5% CO_2, as adapted from (Jahnmatz et al., 2013; Walsh et al., 2013). When PBMCs

were stimulated for 10 days, stimulation medium was changed at day 5 of the stimulation period.

Before processing the cells after stimulation, they were washed twice by centrifugation at 300 xg for 15 min at RT. Cell pellets were resuspended in 10 ml cell culture medium. After the second washing step, cells were filtered through a 30-µm-mesh filter and the cell number was determined.

For supernatant analysis by ELISA, the supernatants were not discarded after the first centrifugation step but filtered through a 0.2-µm filter, aliquoted and stored at -20°C until ELISA analysis.

2.2.4 Magnetic activated cell separation

Cell numbers of freshly thawed or stimulated cells were determined as described before. MACS was performed using the REAlease® CD19 MicroBead Kit (Miltenyi) as described in the user manual. In short, cells were centrifuged at 300 xg for 15 min at RT. The pellets were carefully resuspended in MACS buffer, biotin-coupled antibody cocktail and FcR blocking reagent (Miltenyi) and incubated for 5 min at RT. Then, magnetic microbeads binding against biotin were added and incubated for 5 min at RT. Cell suspension was applied onto the prepared LS column, which was washed with 3x3 ml MACS buffer. The flow-through of unlabeled cells was discarded. The target $CD19^+$ cells were flushed out of the column with 5 ml REAlease Bead Release buffer and incubated for 10 min at RT. The cell suspension was centrifuged as before and the pellet was resuspended in 5 ml REAlease® Release Reagent solution and incubated for 5 min at RT. The enriched $CD19^+$ B cells were then free from MACS reagent complexes and ready for further applications.

2.2.5 Staining for FACS sorting

After MACS, B cell numbers were determined and the cell suspension was centrifuged at 300 xg for 15 min at RT. The cell pellet was resuspended in the viability staining solution (99 µl DPBS and 1 µl of Viobility^{TM} Fixable Dye, Miltenyi Biotech) at a concentration of 10^6 cells per 100 µl and incubated for 10 min at RT in the dark. The cell suspension was filled up to 2 ml with MACS buffer and centrifuged at 300 xg for 10 min at 4°C. The supernatant was aspirated and the cell pellet resuspended in the staining antibody-

mixture (99 µl DPBS with 1 µl CD3-FITC, 2 µl CD19-VioGreen, 2 µl CD20-PE, 2 µl CD27-PE-Vio770, 2 µl CD38-APC, 2 µl CD43-APC-Vio770, Miltenyi biotech) and incubated for 10 min at RT in the dark. Once again, the cell suspension was filled up to 2 ml with MACS buffer and centrifuged at 300 xg for 10 min at 4°C. The supernatant was aspirated and the cell pellet resuspended in sorting medium (1640 RPMI medium without phenol red, 0.5% bovine serum albumin (BSA), 2 mM EDTA) to a concentration of about $2x10^6$ cells/ml and kept on ice until sorting. This protocol was adapted from (Griffin et al., 2012; Quách et al., 2016).

2.2.6 FACS sorting

FACS sorting was performed on a BD FACSAria^{TM} III cell sorter (Beckton Dickinson, San Jose, CA) at the Rudolf Virchow Centre for experimental biomedicine of the University Hospital Würzburg. The BD FACSAria^{TM} III cell sorter was equipped with four lasers (488 nm, 561 nm, 633 nm, 405 nm). FITC fluorescence was measured with a 530/30 filter following 488 nm excitation, whereas VioGreen fluorescence was measured with a 510/50 filter following 405 nm excitation. PE fluorescence was measured with a 582/15 filter and PE-Vio770 fluorescence with a 685 long-pass filter, both following 561 nm excitation. APC fluorescence was determined with a 660/20 filter and APC-Vio770 fluorescence with a 735 long-pass filter, both following 633 nm excitation. The BD FACSDiva software and a 70 µm nozzle was used for B cell sorting at 4°C into the four subgroups memory cells, B1 cells, PBs and $CD20^+CD38^{high}$ cells. Cells were caught in 5 ml round-bottom polystyrene tubes with 700 µl of cooled cell culture medium.

2.2.7 ELISpot assays

ELISpot plates were coated for 24 h or 3 days with 100 µl/well of coating solution. For negative controls 10% FCS in PBS was used as coating solution, for positive controls mouse anti-human kappa chain antibodies (10 µg/ml), for IgG and IgM samples goat anti-human IgG or IgM (5 µg/ml) were used. Plates were wrapped in parafilm to prevent evaporation and stored at 4°C until the next step. Before cell seeding, plates were washed three times with 200 µl/well of cell culture medium and blocked for at least 30 min with 100 µl/well of cell culture medium. Depending on the available cell numbers of B cell subpopulations

100 µl/well of cell suspension was seeded on top of the 100 µl blocking medium. ELISpot plates were incubated at 37°C for 20 h and 5% CO_2. Plates were washed five times with 200 µl/well of DPBS and five times with 200 µl/well of DPBS with 0.1% Tween (DPBS/T). 100 µl/well of alkaline phosphatase (AP)-conjugated IgG- or IgM-antibodies were added and incubated for 18 h at 4°C wrapped in parafilm to avoid evaporation. Before detection the plate was washed three times with 200 µl/well DPBS/T and three times with 200 µl/well of distilled water. 80 µl of the detection solution (Vector Blue Kit) was added per well and incubated in the dark for 3-8 min depending on the spot visibility. Staining was checked by visually evaluating the positive control wells. When they where stained accordingly the reaction was stopped by discarding the reaction solution and washing with 200 µl of distilled water per well. The plates were let dry overnight and stored at 4°C. Protocols were adapted from (Crotty et al., 2004; Racanelli et al., 2006).
Imaging was done using the ImmunoSpot® S5 Versa Analyzer with the software ImmunoCaputre 6.2, which was kindly provided by AG Beyersdorf (Institute for Virology and Immunobiology, University of Würzburg, Germany). Spot counting was manually performed.

2.2.8 ELISA assay

ELISA plates were coated overnight at 4°C with 100 µl of coating solution per well. As coating solution for IgG- and IgM-ELISA goat anti-human IgG or IgM were diluted 1:2000 in 0.1 M carbonate-bicarbonate buffer (pH 9.6). For NF155- and CNTN1-ELISA, 5 µg/ml NF155 protein and 2 µg/ml CNTN1 protein in PBS were used as coating solution. The plates were washed four times with washing buffer. 200 µl of blocking solution per well was incubated at RT for 1 h.
After blocking, the plates were washed twice and 100 µl of PBMC supernatant, diluted accordingly, was applied per well and incubated at 37°C for 90 min. After washing the plate four times with DPBS/T, the suitable secondary horseradish peroxidase (HRP)-conjugated goat anti-human IgG or IgM antibodies (both diluted 1:20 000) were incubated at RT for 1 h. Then, the plate was washed four times with DPBS/T and incubated with 100 µl/well of TMB solution in the dark at 4°C for 20 min. To stop the reaction, 50 µl/well of H_2SO_4 solution was added. Plates were recorded with a Multiskan™ FC microplate

photometer at a wavelength of 450 nm. For each sample, the results of duplicates were averaged for analysis.

For antigen-specific ELISA, 100 µl of undiluted PBMC supernatants, or 100 µl of chicken anti-human NF155 antibodies (diluted 1:1000 in cell culture medium) or goat anti-human CNTN1 antibodies (1:400) for positive controls, were incubated at 37°C for 1 h after blocking. After washing the plate four times with DPBS/T, the suitable secondary HRP-conjugated goat anti-human IgG (diluted 1:10 000), goat anti-chicken IgY (1:5 000, positive control) and donkey anti-goat IgG (1:1 000, positive control) were incubated at 37°C for 30 min. Then, the plate was washed four times with DPBS/T and incubated with 100 µl/well of TMB solution in the dark at 4°C for 20 min. To stop the reaction, 50 µl/well of H_2SO_4 solution were added. Plates were recorded with a Multiskan™ FC microplate photometer at a wavelength of 450 nm. For each sample, the results of duplicates were averaged for analysis.

2.2.9 CIDP patients with auto-antibodies

We received EDTA-blood from CIDP patients who had been tested positive for anti-NF155 or anti-CNTN1 auto-antibodies as determined by ELISA as previously described (Doppler et al., 2015).

2.3 CMT1A study

2.3.1 CMT1A patients and controls

Adult patients were recruited for the CMT-NET study in the hospitals of Münster, München, or Göttingen. They had genetically confirmed diagnoses of CMT1A without any other neurological diseases. From healthy controls, CIDP and small fiber neuropathy (SFN) patients and CMT1A patients, 3-mm skin punch biopsies were taken from the lateral, glabrous part of the index finger as previously described (Li et al., 2005). CIDP, SFN and healthy control samples had already been collected for other studies at the University Hospital of Würzburg (Doppler et al., 2018; Üçeyler et al., 2018). From CMT1A patients, only halves of the 3-mm skin biopsies were used for immunostainings. The other halves were used for other studies within the CMT-NET network. Six CMT1A patients, who had already given a 3-mm skin punch biopsy for the baseline assessment, agreed to another

skin punch biopsy two years later. For the assessment of disease severity, the Charcot-Marie-Tooth Neuropathy Scale version 2 was used, for which the 9 following motor and sensory symptoms are evaluated and rated from 0 (none) to 4 (maximum) (Murphy et al., 2011): sensory symptoms, motor symptoms (legs), motor symptoms (arms), pinprick sensibility, vibration, strength (legs), strength (arms), ulnar CMAP, and radial SNAP amplitude. All patients gave their written informed consent. The study was approved by the ethics committees of the universities München, Münster and Göttingen (IRB number: 31-2-16).

2.3.2 Immunohistochemistry

Half skin biopsy specimens were fixed in 4% PFA for 30 min. They were stored in 10% sucrose at 4°C until freezing. 40-µm sections were cut using a Cryostat Leica CM 3050 S and double-immunolabeled with anti-protein gene product 9.5 (PGP9.5) (PGP9.5, Bio-Rad, Hercules, CA, USA 1:200 or Zytomed Systems, Berlin, Germany, 1:200), anti-myelin basic protein (MBP) (GeneTex, Irvine, CA, USA, 1:200), anti-cytokeratin 20 (CK20) (PROGEN Biotechnik, Heidelberg, Germany, 1:40), anti-S-100 (Abcam, Cambridge, United Kingdom, 1:100), anti-pan-Na_V channel (Sigma Aldrich, St. Louis, MO, USA, 1:100), anti-Caspr (Abcam, Cambridge, United Kingdom, 1:500), anti-NF155 (Abcam, 1:100) or anti-Langerin/CD207 (Dendritics, Lyon, France, 1:500). Primary antibodies were incubated overnight at 4°C and incubation with suitable secondary antibodies (Cy3-conjugated anti-mouse IgG, 1:100, Jackson ImmunoResearch, Suffolk, Great Britain; Alexa Fluor488-conjugated anti-rabbit IgG, 1:400, Jackson ImmunoResearch) was performed at RT for 2 h. Vectashield mounting Medium with DAPI (Vector Laboratories Inc., Burlingame, CA, USA) was used for mounting of the specimens.

2.3.3 Microscopy

For the determination of epidermis lengths and dermis areas - which were used for the density calculations of IENFD, Merkel cell density, Langerhans cell density and nerve bundle densities - images of the stained skin sections were acquired with a fluorescence microscope (Zeiss Axiophot 1, Zeiss, Oberkochen, Germany) with an Axiocam MRm camera (Zeiss) and SPOT software (Diagnostic Instruments, Sterling Heights, MI, USA) with

a 2.5x objective. Epidermis lengths and dermis areas were then measured manually with ImageJ. Intraepidermal nerve fibers, Merkel cells, Meissner corpuscles, Langerhans cells and nerve bundles (more than 5 nerve fibers in a bundle) were counted using a fluorescence microscope Ax10 (Zeiss). Pseudonymization of the specimens was done to blind the investigator during evaluation. For evaluation of the IENFD, numbers of intraepidermal nerve fibers of 4-6 section labeled with anti-PGP9.5 and anti-MBP or anti-CK20 were determined as described elsewhere (Lauria et al., 2005). Numbers of innervated and denervated Merkel cells located at the epidermal-dermal borders were determined for the analysis of the Merkel cell density which was stated as Merkel cells/mm. Langerhans cell density was stated as Langerhans cells/mm. Meissner corpuscle density was measured as Meissner corpuscles/papilla. For this, the number of papillae and Meissner corpuscles was counted. Nerve bundle densities were indicated as nerve bundles/mm^2. For measurements of nodal and paranodal parameters, sections were stained with anti-Caspr and anti-pan-sodium channels. Per sample five dermal nodes of Ranvier were analyzed, when possible. In total, the nodal lengths and diameters, hemiparanodal and paranodal lengths of 164 nodes from 43 CMT1A patients, 34 nodes from seven CIDP patients, 75 nodes from 15 SFN patients and 189 from 42 healthy controls were determined as described in Figure 2. Asymmetry indices were calculated as described elsewhere (Saporta et al., 2009). Furthermore, ratios of nodal lengths and diameters were calculated. When length-to-diameter ratios were greater than 1, nodes were considered long.

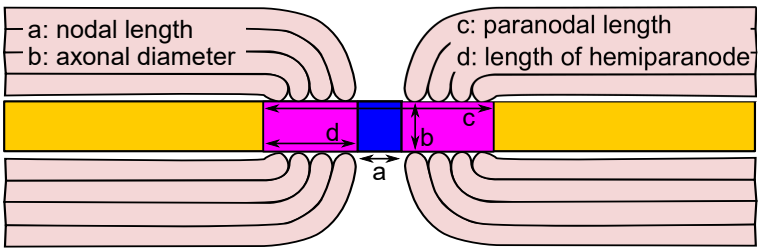

Figure 2: Schematic of the node of Ranvier with the indication of the measured parameters. For determinations of nodal and paranodal parameters, the nodal length and diameter were measured, which are depicted as section a and b, respectively. For determining asymmetry indices, lengths of the hemiparanodes (section d) were measured. Paranodal lengths were determined by measuring section c, which also includes the nodal region. This figure has been previously published in the supplement of *Hartmannsberger et al. (2020)*.

For all follow-up biopsy analyses, 5-6 sections were double-labeled with anti-PGP9.5 and

anti-CK20. The IENFD, Merkel cell density and Meissner corpuscle density were determined in six CMT1A samples.

2.4 Statistical analyses

The Python library SciPy in Python version 3.7.3 (Python Software Foundation, Delaware, USA) was used for performing statistical analyses. For testing for normal distributions of data sets, the Shapiro-Wilk test for normality was performed. For comparison of data sets, we performed the two-tailed Mann-Whitney U test. For correlation analysis Pearson correlation coefficients were calculated. For $p<0.05$, differences were considered statistically significant.

3 Results

3.1 Passive transfer experiments: The pathogenicity of CIDP auto-antibodies

Purified IgG from a CIDP patient with anti-CNTN1 auto-antibodies predominant of the IgG4 isoform has been shown to cause loss of F-waves in the sciatic nerve after intraneural injections in a previous study (Doppler et al., 2019). However, neither motor nor sensory functions were affected by anti-CNTN1 IgG4 auto-antibodies in the sciatic nerves although analyses of teased sciatic nerve fibers revealed binding of the auto-antibodies to the paranodal regions (Doppler et al., 2019).

3.1.1 No effects of auto-antibodies on motor or sensory functions after intrathecal application

We investigated the effect of anti-CNTN1 IgG4 auto-antibodies from the same patient when applied to the nerve roots by intrathecal injection. To assess motor and sensory functions of the treated animals, a series of behavioral tests (rotarod, Catwalk, von-Frey and Hargreaves tests) was performed on days 3, 8, 15 and 20 after the first IgG injection. In total, we investigated 16 Lewis rats injected with control IgG (also referred to as control animals/rats) and 12 animals injected with patient IgG (patient animals/rats).

There were no differences between the control and patient group regarding motor performance as assessed by accelerating rotarod testing (Fig. 3 A, D, G, J, M). Time course analysis of each group showed decreased motor performance in rats treated with control IgG on day 8 compared to baseline and day 3 values, whereas rats treated with patient IgG showed no significant differences over time, although both groups showed a similar trend (Fig. 4 A).

For the analysis of sensory functions, the response to mechanical stimuli was determined using the von-Frey test. Patient rats showed higher sensitivity compared to control rats on day 3 after injection start, while on the other test days there were no differences between the groups (Fig. 3 B, E, H, K, N). The time course analysis showed that there were no changes in control animals over time, whereas patient animals were more sensitive on day 3 compared to day 20 (Fig. 4 B).

Furthermore, there were no differences in thermal sensitivity as assessed by Hargreaves testing between the control and patient groups on all test days (Fig. 3 C, F, I, L, O). Neither were there changes in thermal sensitivity detected over the three-week injection period in either group, respectively (Fig. 4 C).

For gait analysis Catwalk testing was performed. The print areas, standing times and mean maximum intensities for each hind paw were calculated. No differences between control and patient print areas were detected at baseline and days 3, 8 and 20 after IgG injections. On day 15, patient animals showed decreased print areas of the left hind paws compared to the corresponding control paws (Fig. 5 A, D, G, J, M). Time course analysis revealed increased print areas on day 20 compared to day 3 in the right patient paws. In control animals, print areas were decreased at day 8 compared to baseline values in right paws. Left control paws showed decreased print areas on day 15 compared to day 3 (Fig. 6 A). In both groups, there was a trend for smaller print areas after the start of IgG injection but were restored again at day 20 (Fig. 6 A). Standing times did not differ between groups on all testing days (Fig. 5 B, E, H, K, N). In control animals, standing time gradually decreased over time leading to shortening at day 20 when compared to baseline in the right hind paws. Standing time of the left control paws showed the same trend but did not reach statistical significance (Fig. 6 B). For patient animals, standing time was decreased at day 3 compared to baseline. This difference was only significant for the left paws and was restored again at day 8 (Fig. 6 B). Comparison of mean maximum foot print intensity between the groups only showed a decrease in left patient paws compared to controls on day 8 (Fig. 5 C, F, I, L, O). Patient animals did not show changes over time. In control animals, the intensities of the left paws were decreased on day 8 compared to days 15 and 20 (Fig. 6 C).

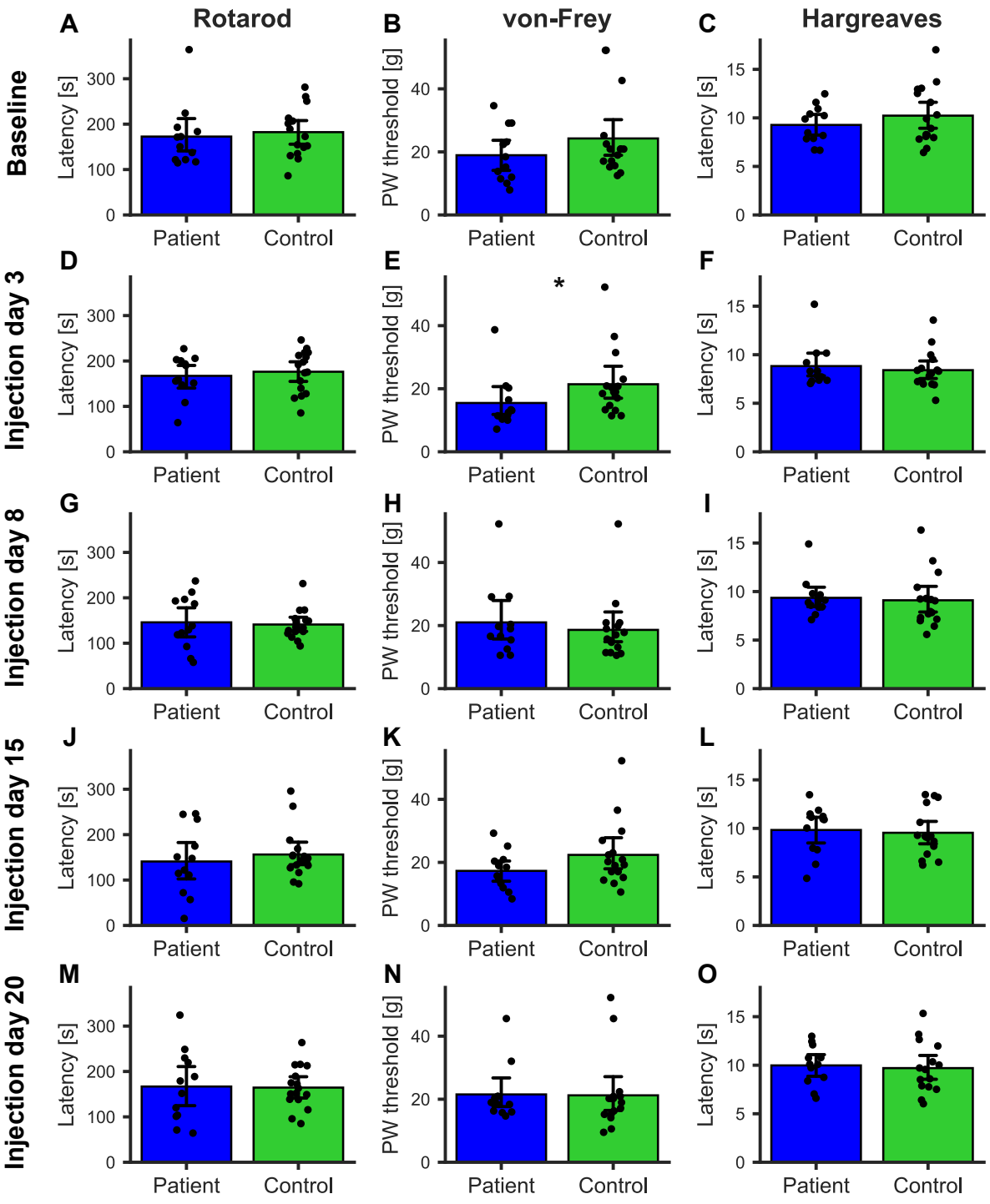

Figure 3: No differences in comparison of control to patient animals in rotarod, von-Frey or Hargreaves tests at baseline (A-C) and days 3 (D-F), 8 (G-I), 15 (J-L) and 20 (M-O) after the first IgG injection. Increased sensitivity in patient animals compared to controls only on day 3. A, D, G, J, M) There were no differences in rotarod fall latencies between the patient and control groups. B, E, H, K, N) Only on day 3, patient animals showed differences in sensitivity to mechanical stimuli compared to control animals. C, F, I, L, O) Between the groups, there were no differences in thermal sensitivity as determined by Hargreaves testing. $*$: $p<0.05$.

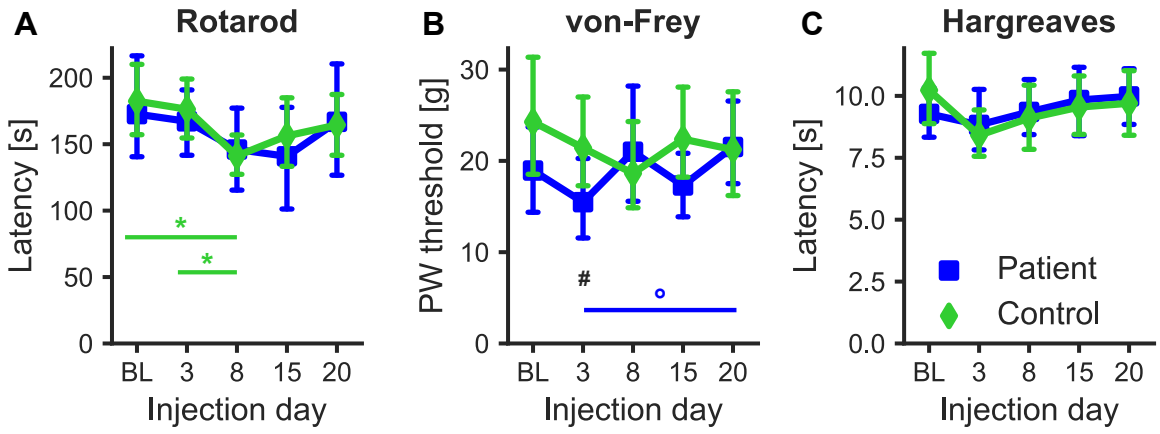

Figure 4: No motor or sensory impairment in patient and control animals over three weeks of analysis as determined by rotarod (A), von-Frey (B) and Hargreaves (C) tests. A) Patient animals did not show changes in motor performance, whereas in control animals latency to fall was decreased on day 8 compared to baseline and day 3 ($*$: $p<0.05$). B) Control animals did not show changes in response to mechanical stimuli, while patient animals showed higher sensitivity on day 3 compared to day 20 ($\circ$: $p<0.05$). On day 3, patient animals were more sensitive to mechanical stimuli compared to controls (#: $p<0.05$). C) There were no changes in thermal sensitivity in neither group, respectively. BL: baseline.

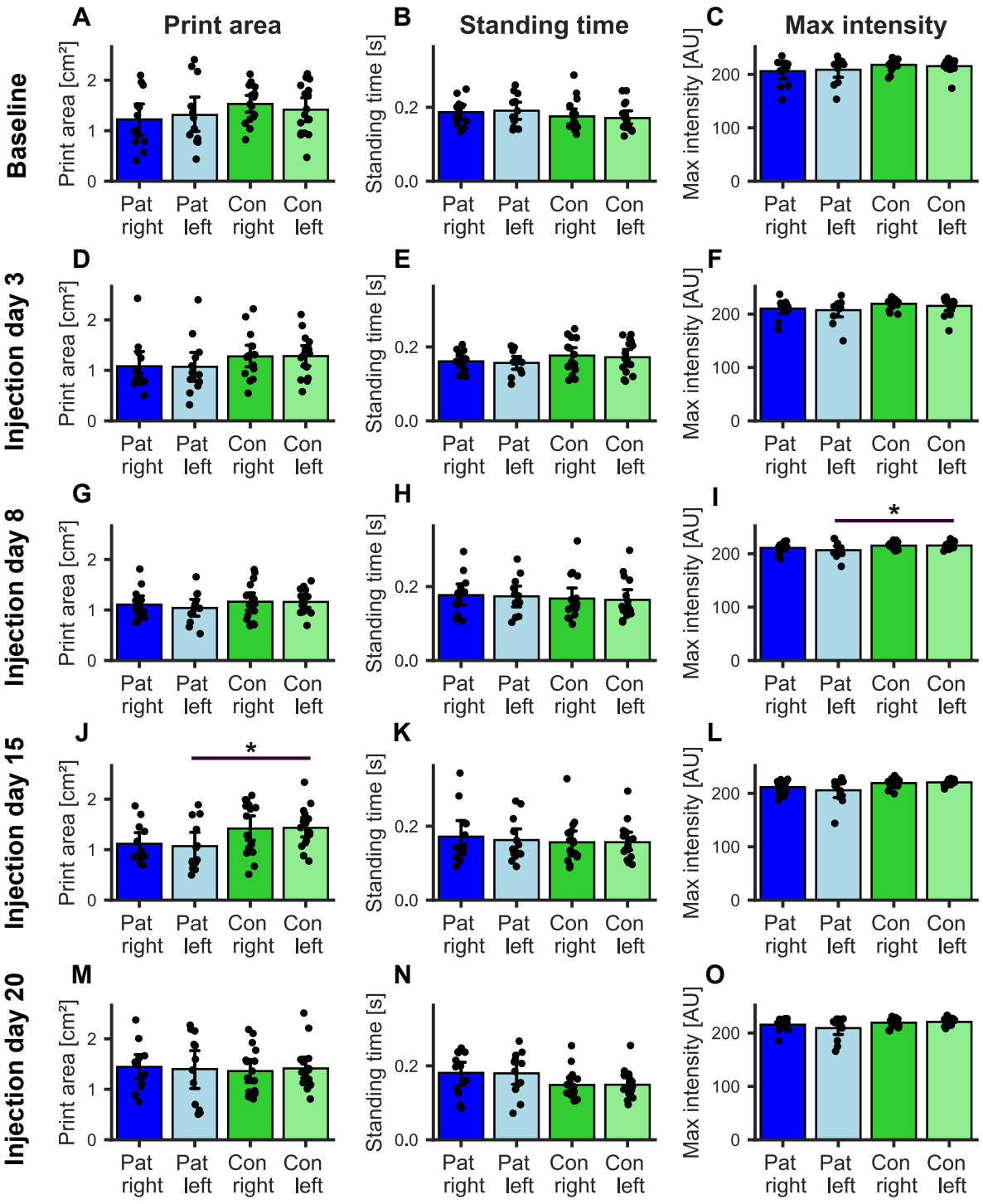

Figure 5: Comparison of gait properties between patient and control animals at baseline (A-C) and on days 3 (D-F), 8 (G-I), 15 (J-L) and 20 (M-O) after first injection. A, D, G, J, M) Only on day 15, there were differences in the print areas between the left hind paws of patient and control groups. B, E, H, K, N) Standing times did not differ between the patient and control groups at all test days. C, F, I, L, O) The mean maximal intensity only differed on day 8 between the left hind paws of patient and control animals. $*$: $p<0.05$.

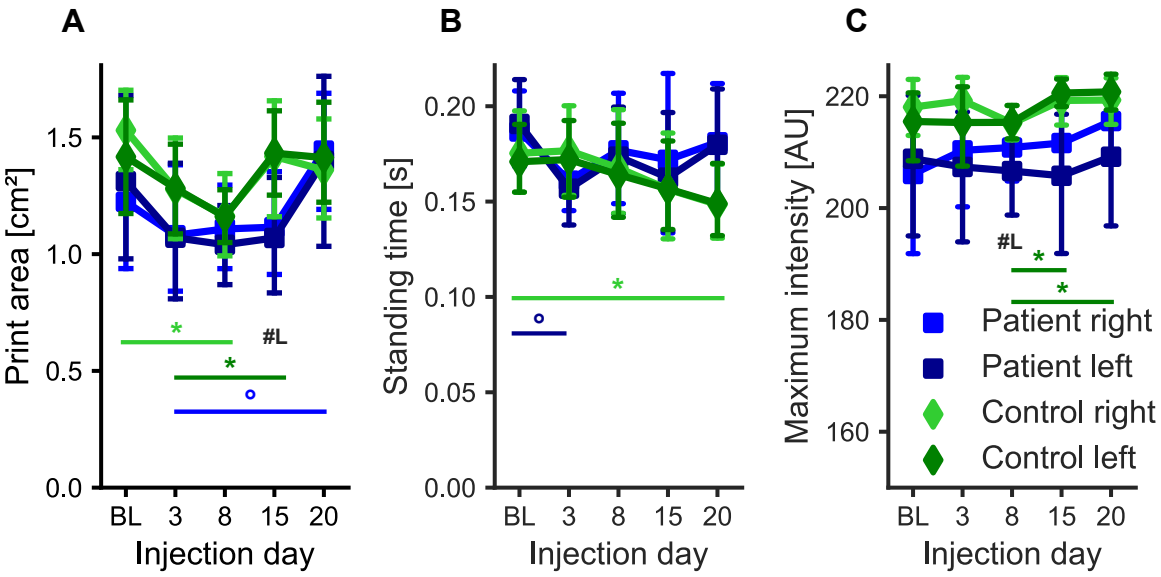

Figure 6: Time course analysis of gait properties as determined using the Catwalk. A) Patient animals did not show changes in maximum intensity of foot prints, whereas left control animal paws showed a decrease at day 8 compared to days 15 and 20 (∗: $p<0.05$, # L: left patient - control paws: $p<0.05$). B) Patient animals showed an initial decline of standing time at day 3 compared to baseline, while in control animals standing time declined progressively until changes were significantly decreased at day 20 compared to BL in right hind paws (∗: $p<0.05$, ř: $p<0.05$). C) Patient animals did not show changes in maximum intensity of foot prints, whereas left control animal paws showed a decrease at day 8 compared to days 15 and 20 (∗: $p<0.05$, # L: left patient - control paws: $p<0.05$). BL: baseline.

3.1.2 No effects of auto-antibodies on nerve conduction properties after intrathecal application

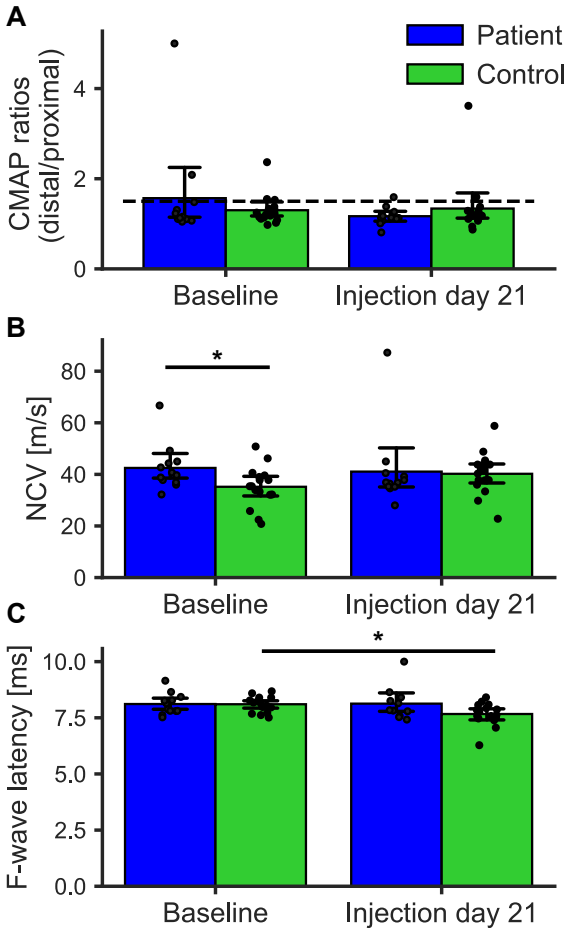

Figure 7: No changes of nerve conduction properties after the 21 day-long injection period in patient animals. A) CMAP ratios showed neither differences between the patient and control groups, nor changes over time within the groups, respectively. The dashed line indicates the 1.5 ratio. B) NCV did not change over time within the groups, respectively. At baseline, control animals showed lower NCV compared to patient animals. C) F-wave latencies improved over time in control animals. In patient animals the latency did not change over time. There were no differences between the groups at both time points. *: $p<0.05$.

Nerve conduction measurements were performed before the first IgG injection and on the day following the last injection, day 21. The ratio of distal to proximal CMAPs can be analyzed to detect conduction blocks. Ratios larger than 1.5 have been previously described as an indicator for conduction blocks (Doppler et al., 2019). There were no differences between the patient and control group regarding CMAP ratios at baseline and injection day 21, neither were there changes over time within the groups. 12.5% of control rats showed signs of conduction block at baseline and 6.25% after injections. In

the patient group, 16.7% of the animals showed elevated CMAP ratios at baseline and 8.3% after injections (Fig. 7 A). Nerve conduction velocities did not change over time in patient animals. At baseline measurements, control NCVs were reduced compared to the patient group. However, there were no differences between the groups after the injection period (Fig. 7 B). F-wave latencies did not change over time in patient animals. In controls however, there was a significant reduction after the injection period compared to baseline values. There were no differences between the groups at both time points (Fig. 7 C). F-wave persistencies recorded at 0.3 Hz, 1 Hz and 10 Hz did not differ between patient and control groups (Fig. 8). Representative plots of recordings of CMAPs in control (Fig. 9 A) and patient (Fig. 9 C) animals show no abnormalities in neither case. Also in F-wave recordings, there were no abnormalities neither in the control case (Fig. 9 B) nor in the patient case (Fig. 9 D).

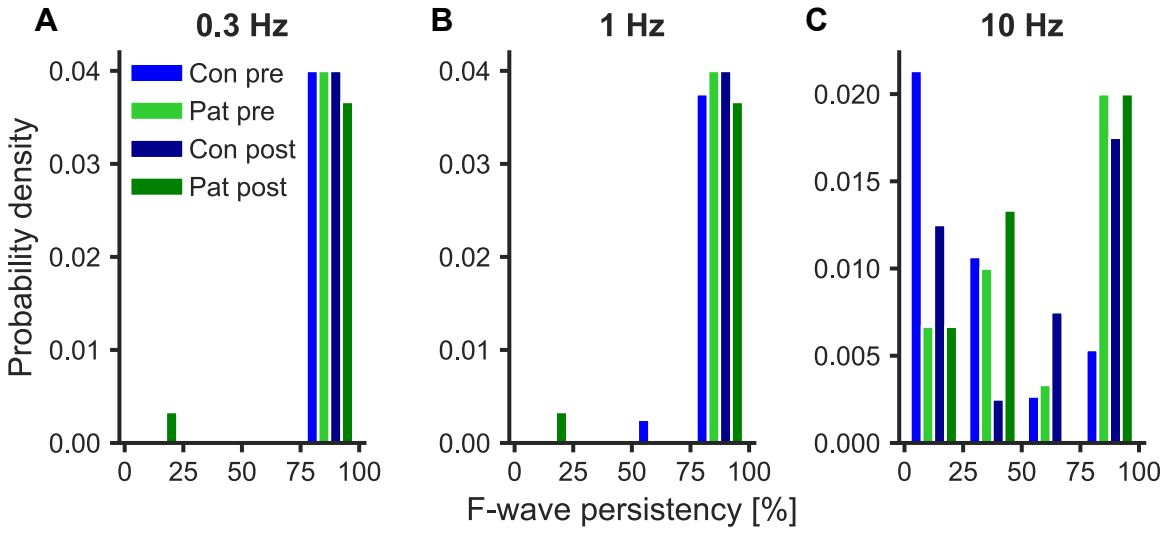

Figure 8: No changes of F-wave persistencies after intrathecal IgG injections when stimulated at frequencies of 0.3 Hz (A), 1 Hz (B) and 10 Hz (C) in neither group.

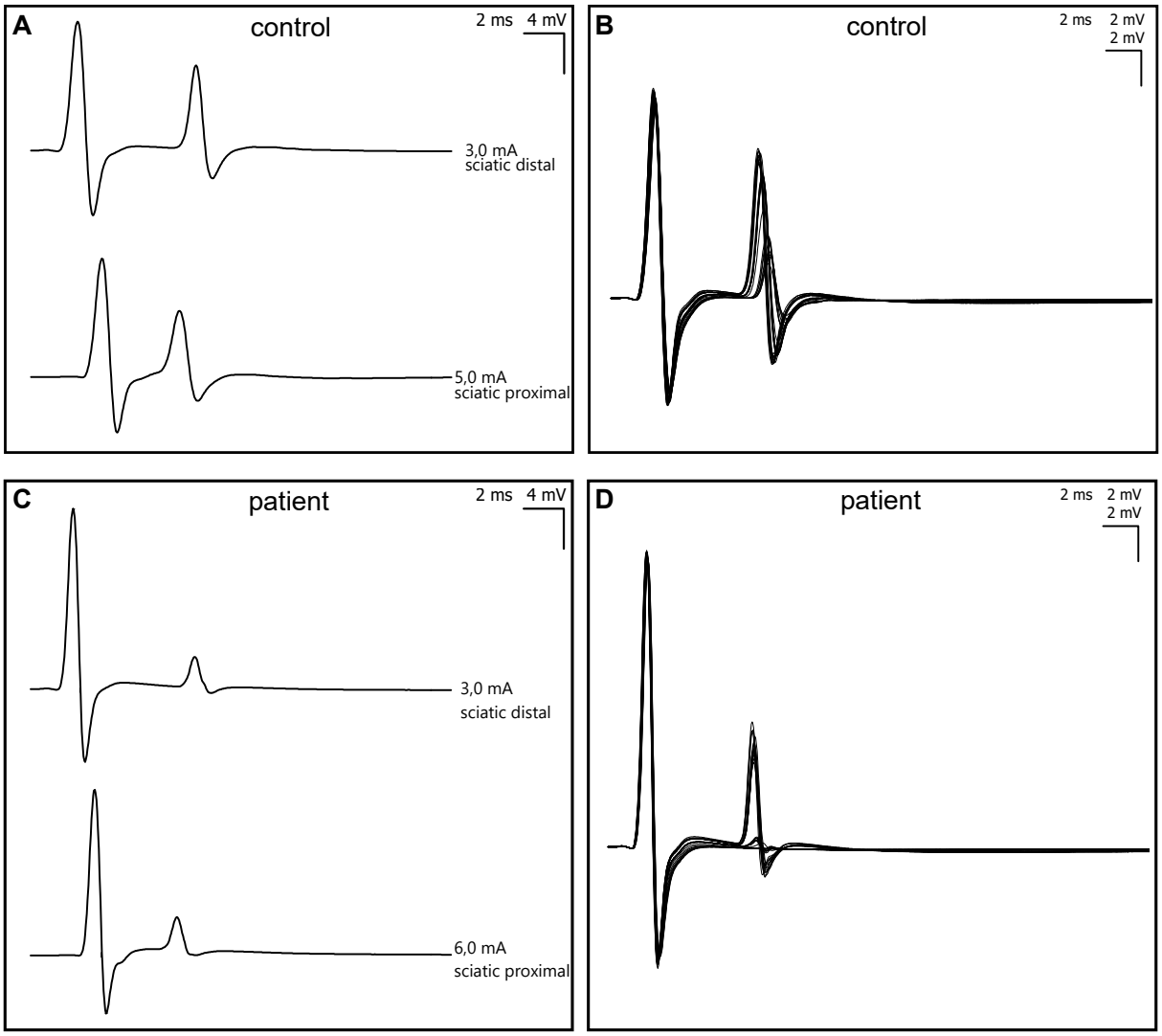

Figure 9: Representative examples of M-waves after single proximal and distal stimulations (A, C) and F-waves after repetitive distal stimulations (B, D). A, C) Recordings of M-waves (first peak) and F-waves (second peak) after single distal (top) and proximal (bottom) stimulation, respectively. B, D) Overlay of recordings after 10 repetitive stimulations with 0.3, 1 and 10 Hz, respectively.

3.1.3 No binding of auto-antibodies to nerve roots after three weeks of intrathecal injections

To investigate if anti-CNTN1 IgG auto-antibodies bound to the lumbar nerve roots after intrathecal injection, we stained teased nerve roots (L3) harvested at injection day 20/21 with secondary anti-human IgG antibodies. Analysis of 12 motor and sensory nerve roots from rats injected with patient IgG did not show any binding. In 16 rats injected with control IgG, there was also no binding detected in neither the motor nor sensory nerve roots. Representative images of nodes of Ranvier in teased nerve roots are shown in Fig. 10.

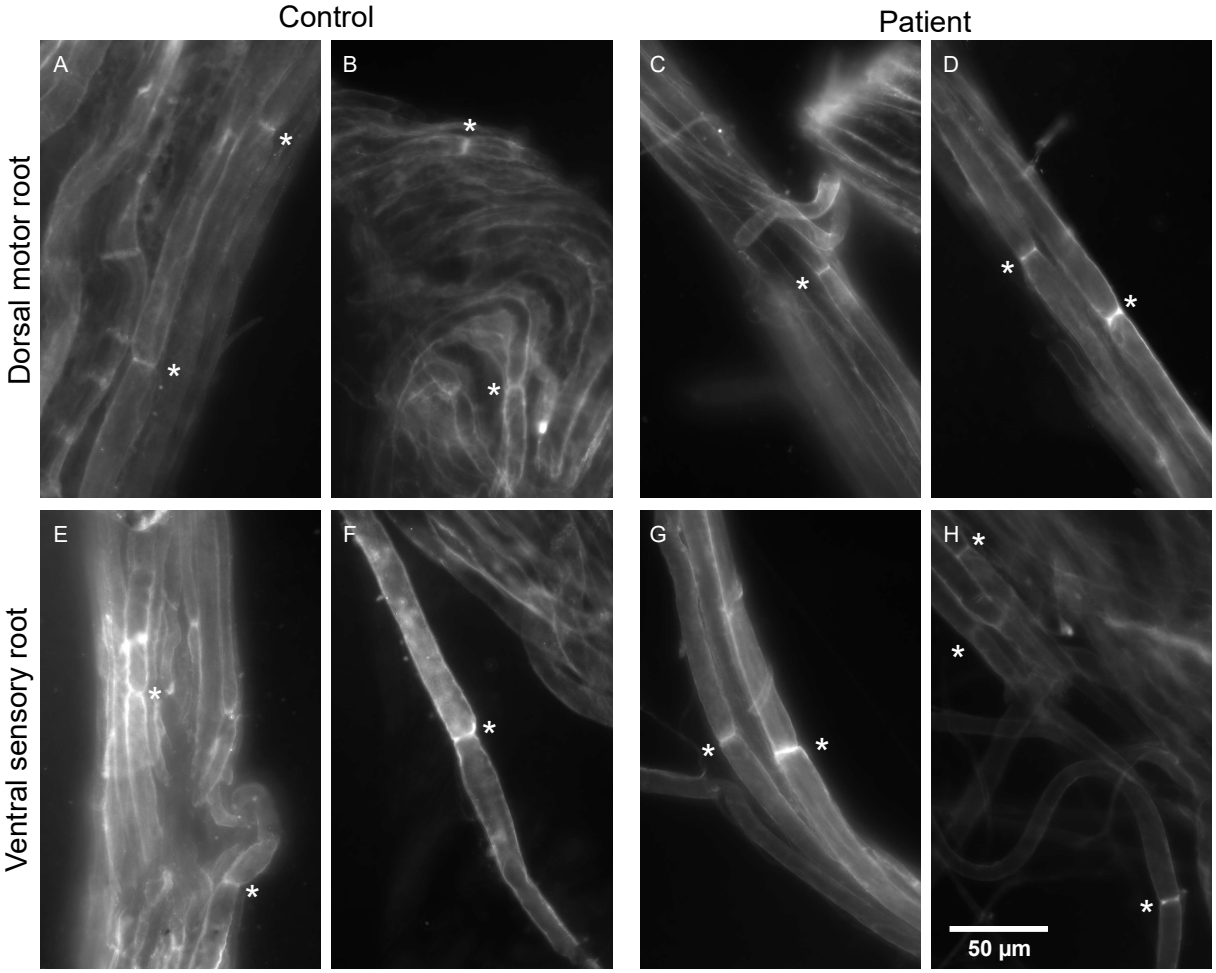

Figure 10: No binding of anti-CNTN1 auto-antibodies detectable in teased motor and sensory nerve roots. Teased fibers were stained with Cy3-conjugated secondary anti-human IgG. Asterisks mark nodes of Ranvier, at none of which binding of antibodies was detectable.

In addition, nerve fibers of two patient animals dissected at injection day 12/13, five patient animals dissected at injection day 10 and one patient animal dissected at day 7

did not show any binding at the paranodal regions of the node of Ranvier. A second investigator (Kathrin Doppler) confirmed that there was no binding of anti-CNTN1 auto-antibodies detectable.

To ensure that the injected IgG was able to reach the lumbar nerve roots, we injected 10 µl EBD solution intrathecally in one rat. We could confirm that Evans Blue spread reached the lumbar spine as well as the lumbar dorsal root ganglia and the associated lumbar nerves (L3, L4, L5) 16 h after injection as shown in Fig. 11.

This suggests that anti-CNTN1 IgG auto-antibodies were able to reach the investigated nerve roots but did not bind to the paranodal regions.

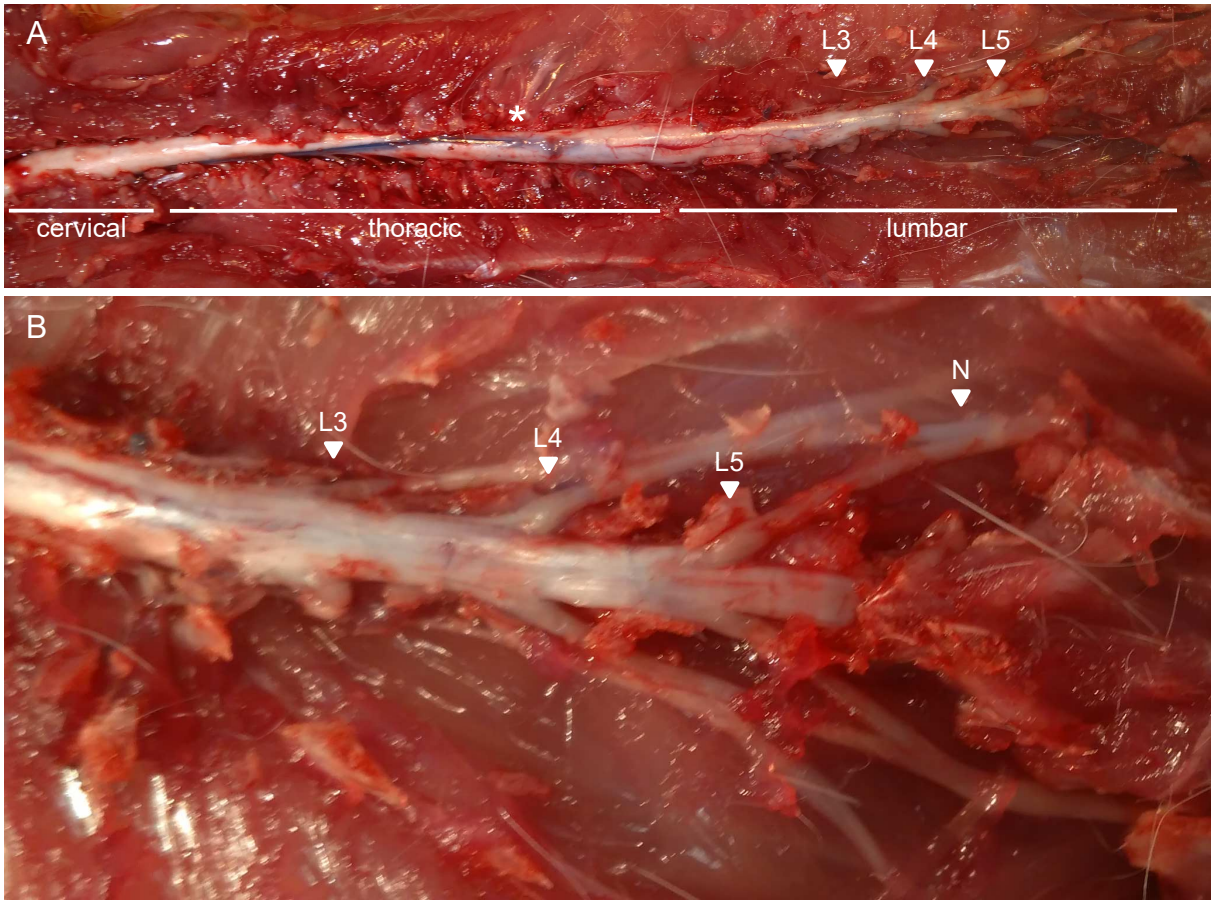

Figure 11: Photographs of spinal cord and dorsal root ganglia with lumbar nerves (L3, L4, L5) confirm spread of EBD into lumbar regions 16 h after injection through intrathecal catheters. A) Cervical, thoracic and lumbar regions of the spinal cord and lumbar dorsal root ganglia. The cervical and more cranial thoracic regions of the spinal cord appear clear white, while the more caudal regions are dyed blue. The catheter is visible as dark blue line on the thoracic spinal cord ending at the asterisk (*). Lumbar root ganglia (L3, L4, L5) also appear blue. B) Lumbar region of the spinal cord with dorsal root ganglia and associated lumbar nerves (L3, L4, L5) are dyed blue 16 h after EBD injection.

3.2 B lymphocyte study

The aim of the B lymphocyte project was to identify the auto-antibody producing B cell subtype from peripheral blood of CIDP patients. This was supposed to be achieved by antigen-specific ELISpot analysis of the FACS sort purified antibody-secreting B cell subsets, which were previously described (Quách et al., 2016). Since we had very limited access to patient blood, we started the establishment of the B cell project - PBMC freezing, thawing, stimulation, MACS, FACS sorting with the 6-color-panel staining and ELISpot protocols - with PBMCs from healthy controls. In the following, PBMCs from healthy donors were used unless stated otherwise. Also most of the performed ELISpot assays were not antigen-specific, but we performed whole IgG- or IgM-detecting ELISpots unless indicated otherwise.

3.2.1 Sort purification of antibody-producing B cell subsets

B cells from peripheral blood have been previously classified into four subpopulations - three of which spontaneously secrete antibodies. Memory B cells do not spontaneously produce antibodies, while PBs, B1 cells and $CD20^{+}CD38^{hi}$ cells do (Quách et al., 2016). To analyze the antibody secretion of these B cell subpopulations, we FACS sorted MACS-purified $CD19^{+}$ B cells after the exclusion of doublets, dead cells, $CD3^{+}$ T cells, and $CD19^{-}$ cells. The four $CD19^{+}$ B cell subtypes were further gated based on their expression of CD20, CD27, CD38 and CD43 as shown in Fig. 12, which was previously described (Quách et al., 2016). Memory B cells were characterized as $CD19^{+}CD20^{+}CD27^{+}CD43^{-}$ with low to intermediate expression level of CD38, while B1 cells as $CD19^{+}CD20^{+}CD27^{+}$ $CD43^{+}$ also showing low to intermediate CD38 expression. PBs were characterized as $CD19^{+}CD20^{-}CD27^{+}CD38^{hi}$, whereas $CD20^{+}CD38^{hi}$ cells were $CD19^{+}CD20^{+}CD27^{+}$ $CD38^{hi}$.

To ensure proper classification of expression levels, gates were adjusted by using fluorescence minus one (FMO) controls, where cells were stained with the whole panel of staining antibodies except for one. We made FMO controls for FITC, PE-Cy7, APC and APC-Cy7 (Fig. 13). The FITC FMO control was used to adjust the dump gate by which $CD3^{+}$ cells and dead cells were excluded.

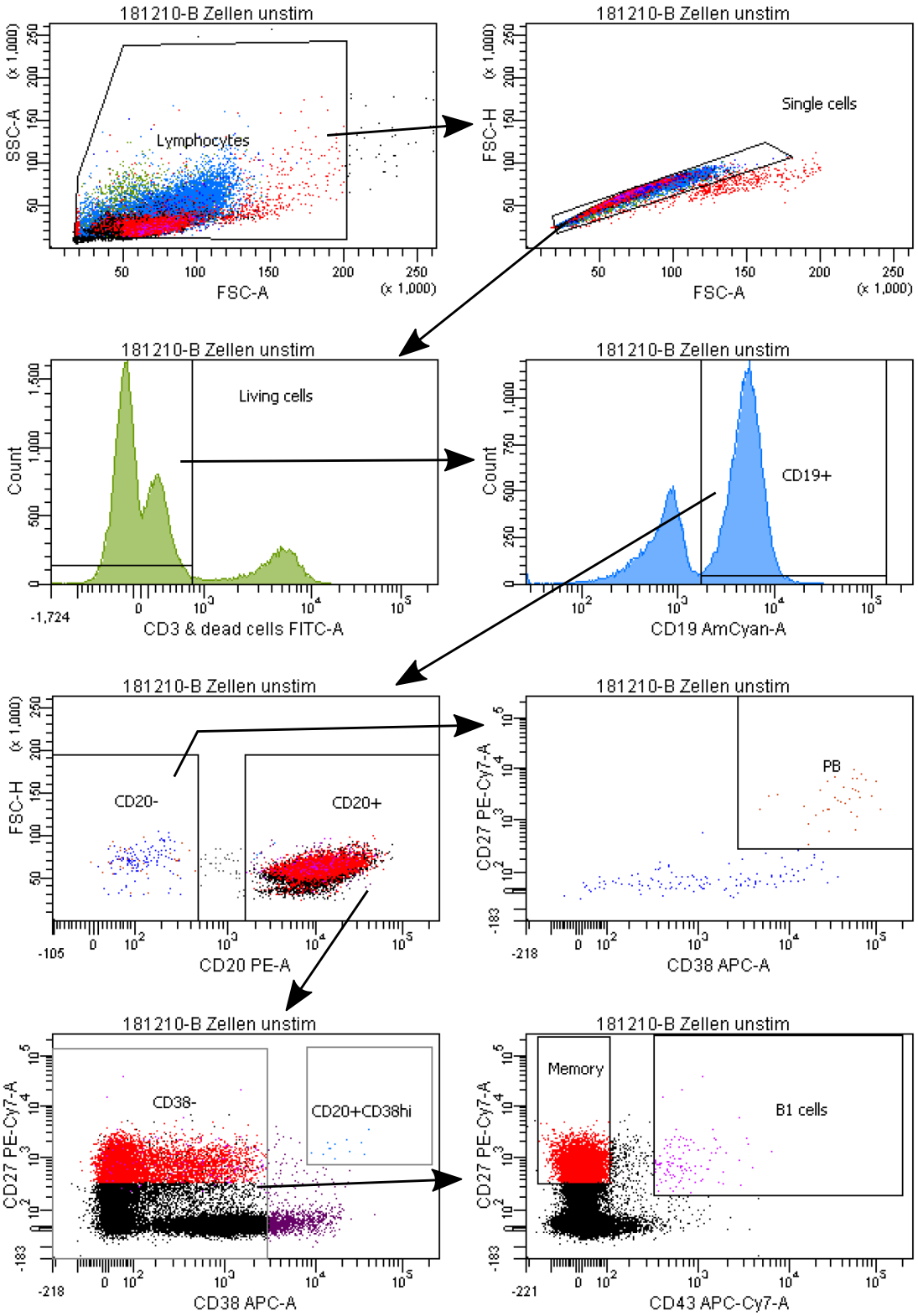

Figure 12: Gating scheme shown on exemplary plots for cell sorting of freshly thawed, unstimulated CD19$^+$ cells after MACS purification. PBMCs were thawed and CD19$^+$ cells were purified by MACS. CD19$^+$ cells were then analyzed and sorted into the target cells: PBs (CD19$^+$CD20$^-$CD27^{hi}CD38^{hi}), CD20$^+$CD38^{hi} cells (CD19$^+$CD20$^+$CD27^{hi}CD38^{hi}), memory B cells (CD19$^+$CD20$^+$CD27$^+$CD43$^-$) and B1 cells (CD19$^+$CD20$^+$CD27$^+$CD43$^+$).

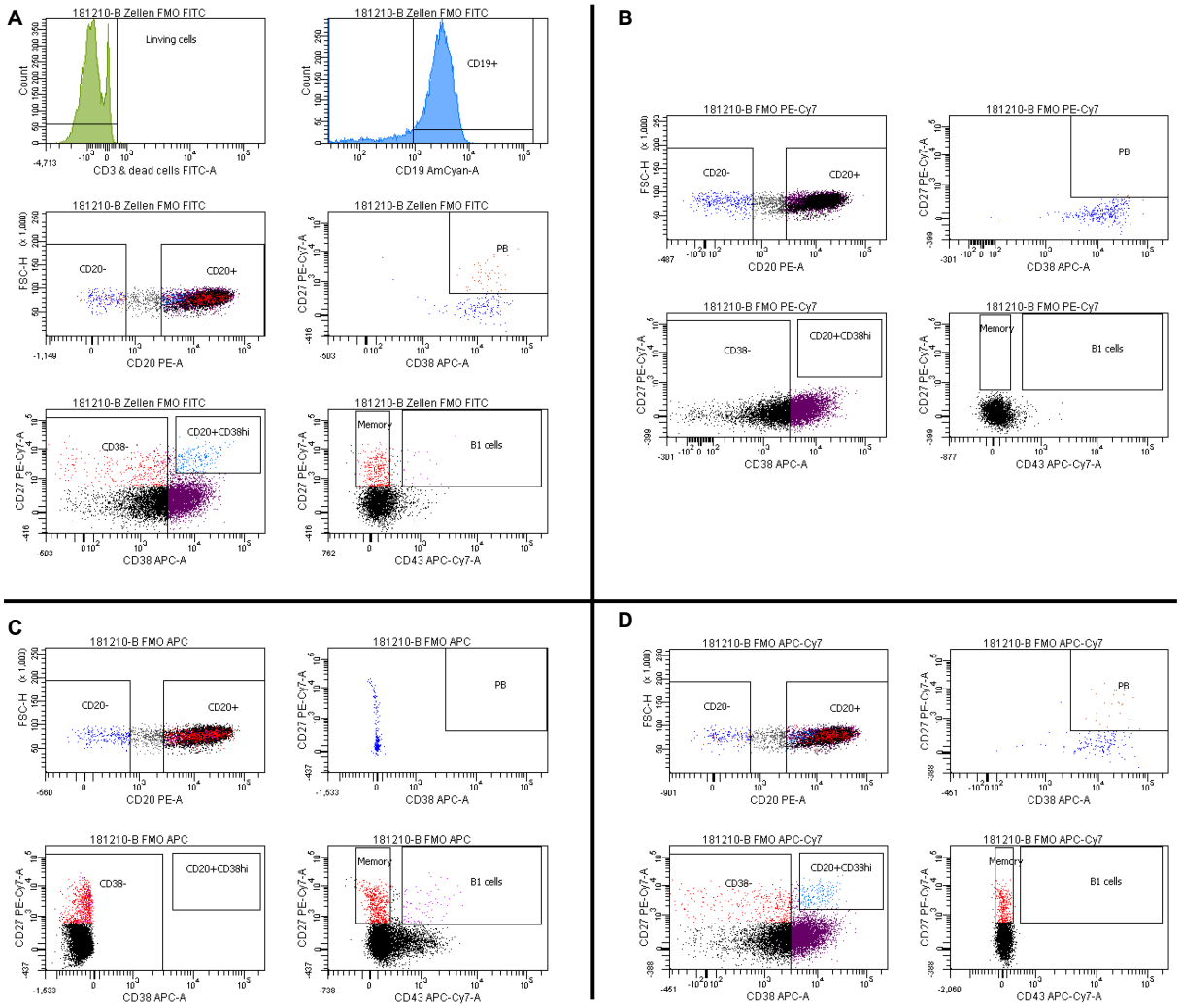

Figure 13: Sort plots of the FMO controls for FITC (A), PE-Cy7 (B), APC (C), APC-Cy7 (D) that were used for gate adjustments. A) The dump channel gate for the exclusion of CD3k cells and dead cells was adjusted using the FITC FMO control. B) The PE-Cy7 FMO control was used to adjust gates for PBs, $CD20^{+}CD38^{hi}$ cells, memory B cells and B1 cells. C) Gates for PBs, $CD38^{-}$ cells and $CD20^{+}CD38^{hi}$ cells were adjusted using an APC FMO control. D) The APC-Cy7 FMO control was done to adjust the gates for memory B and B1 cells.

For proper setup of the PB and the $CD20^{+}CD38^{hi}$ gates APC and PE-Cy7 FMO controls were evaluated. On the basis of PE-Cy7 and APC-Cy7 FMO controls the memory B cell and B1 cells gates were adjusted. As another quality control of our sort setup, the purity of isolated memory and naive B cell populations was determined by post-sort FACS reanalysis. These two subpopulations were used for post-sort analysis as sufficient numbers of cells for both, post-sort and downstream analysis, were retrieved. Both B cell subpopulation showed a high purity of 98% (Fig. 14).

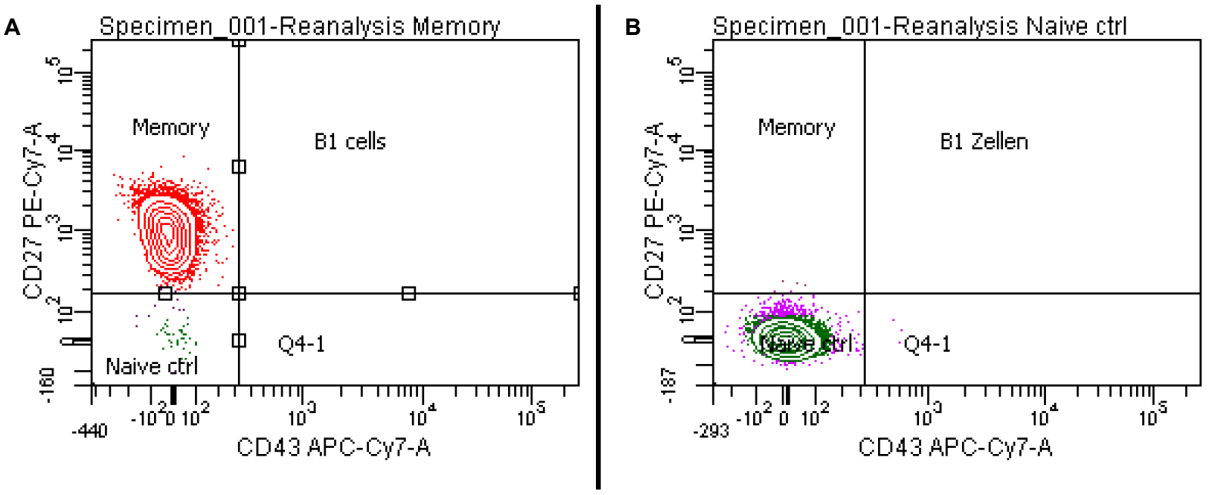

Figure 14: Sort plots of post-sort reanalysis of memory B cells (A) and naive B cells (B). Purities of post-sort reanalyzed memory B cell (A) and naive B cell (B) subpopulations were 98%, respectively.

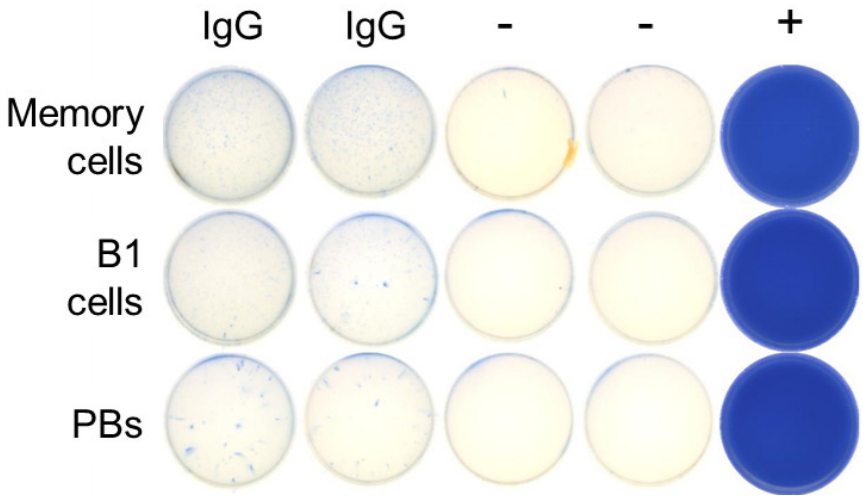

Figure 15: Image of ELISpot for the analysis of whole IgG secretion by memory B cells, B1 cells and PBs from unstimulated PBMCs after FACS sorting. About 5000 memory B cells, 2000 B1 cells and 450 PBs were seeded per well for 16h.

In order to obtain sufficient $CD19^+$ B cells for ELISpot analysis, at least 80×10^6 PBMCs were thawed which usually resulted in at least 2×10^6 $CD19^+$ cells after MACS. Preliminary ELISpot analyses of the frequency of IgG-secreting memory B cells, B1 cells and PBs revealed very low antibody production in B cells from freshly thawed, unstimulated PBMCs (Fig. 15). As expected, memory B cells did not secrete IgG. The frequency of antibody-secreting B1 cells and PBs was very low. It became obvious that the probability to detect antigen-specific B cells would be minimal with these low frequencies of

antibody-secreting B cells. Therefore, we decided to stimulate the PBMCs before MACS and FACS sorting with IL-2 and R848 for 72 h, since it has been previously shown that with this protocol frequencies of antibody-secreting cells reached a maximum (Jahnmatz et al., 2013).

3.2.2 Spontaneous and stimulated antibody-secretion of B cells subsets

In order to characterize B cell subsets from PBMCs that were stimulated with IL-2 and R848 for 72 h prior to MACS purification and FACS sorting, unstimulated B cells were compared to stimulated B cells. Frequencies of memory B cells, naive B cells, $CD20^{+}CD38^{hi}$, PBs, and B1 cells were evaluated by FACS. Representative sort plot of purified B cells from stimulated PBMCs are shown in Fig. 16. The occurrence of $CD20^{+}CD38^{hi}$ seemed to be increased while PB occurrence seemed to be declined. Indeed, quantification of 11 more sorts of stimulated cells in comparison to 10 sort of unstimulated cells revealed an increase in $CD20^{+}CD38^{hi}$ and naive B cells whereas the memory B cell frequency decreased. The frequencies of the other subsets did not change (Fig. 17).
Analysis of antibody secretion of each subset revealed higher spot numbers for each subset as shown in this representative ELISpot plate for both IgG and IgM (Fig. 18). However, only seeded cell numbers of memory B cells and B1 cells were comparable as the 3-day stimulation resulted in more $CD20^{+}CD38^{hi}$ cells but less PBs. Quantification of 4 ELISpots, in which unstimulated and stimulated B cell subsets from the same donor were compared respectively, showed an increase of IgG-secreting cells in memory B cells and B1 cells, while the frequencies in PBs and $CD20^{+}CD38^{hi}$ cells remained the same (Fig. 19). Similar results were found for the frequency of IgM-secreting cells. Memory B cells as well as B1 cells showed an increase, while the frequency of antibody-secreting cells in PBs did not change. However, the frequency in $CD20^{+}CD38^{hi}$ cells was also increased in stimulated compared to unstimulated cells regarding IgM secretion (Fig. 19).

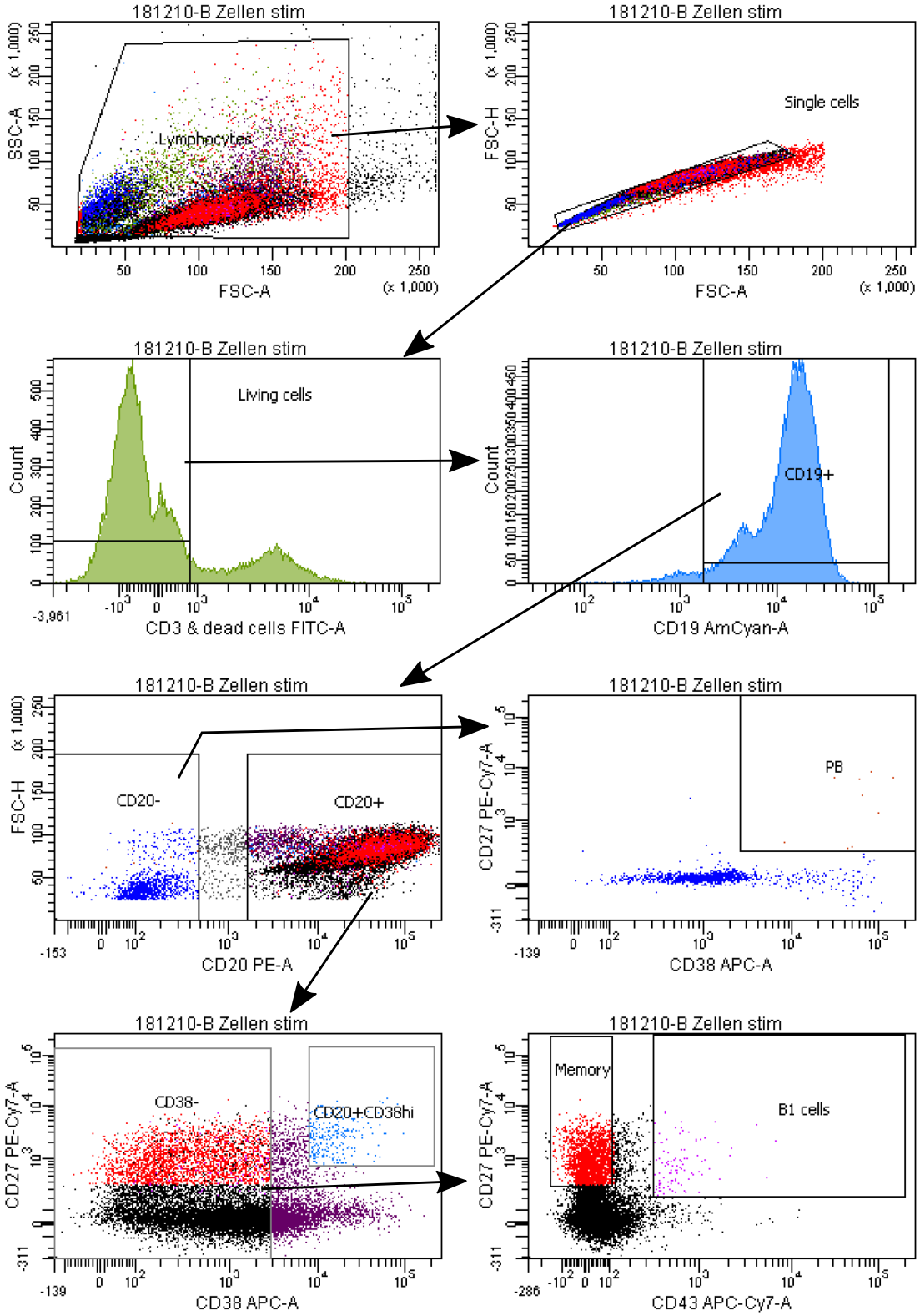

Figure 16: Representative sort plots of cell sorting of stimulated CD19$^+$ cells after MACS purification. After thawing PBMCs were stimulated with IL-2 and R848 for 3 days. Stimulated PBMCs were MACS purified to enrich CD19$^+$ cells. Compared to unstimulated cells, CD20$^+$CD38^{hi} tended to be increased, while PB numbers declined.

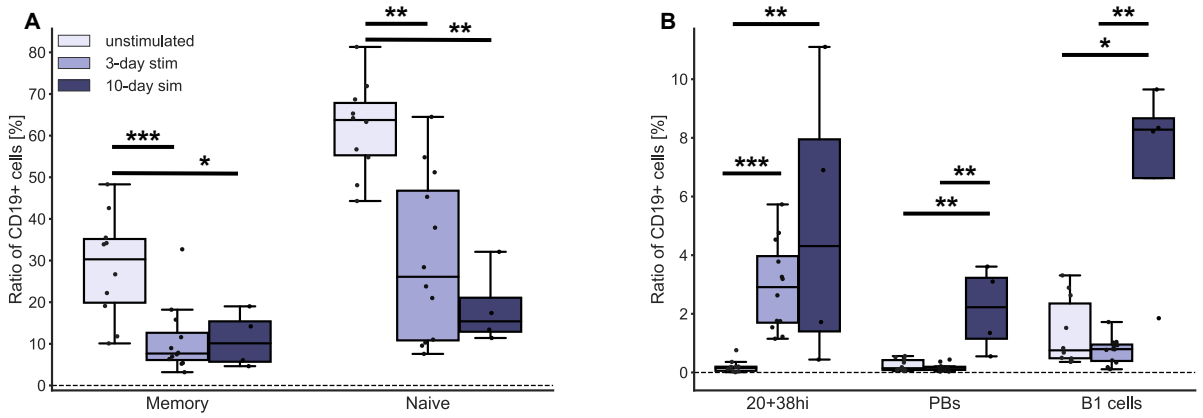

Figure 17: Frequencies of each subset of CD19$^+$ B cells from PMBCs as assessed by FACS analysis. A) Frequencies of memory B cells and naive B cells. B) Frequencies of CD20$^+$CD38^{hi} cells, PBs and B1 cells. For unstimulated cells 10 experiments, for 3-day stimulated cells 12 experiments and for 10-day stimulated cells 4 experiments were performed. *: p<0.05, **: p<0.01, ***: p<001.

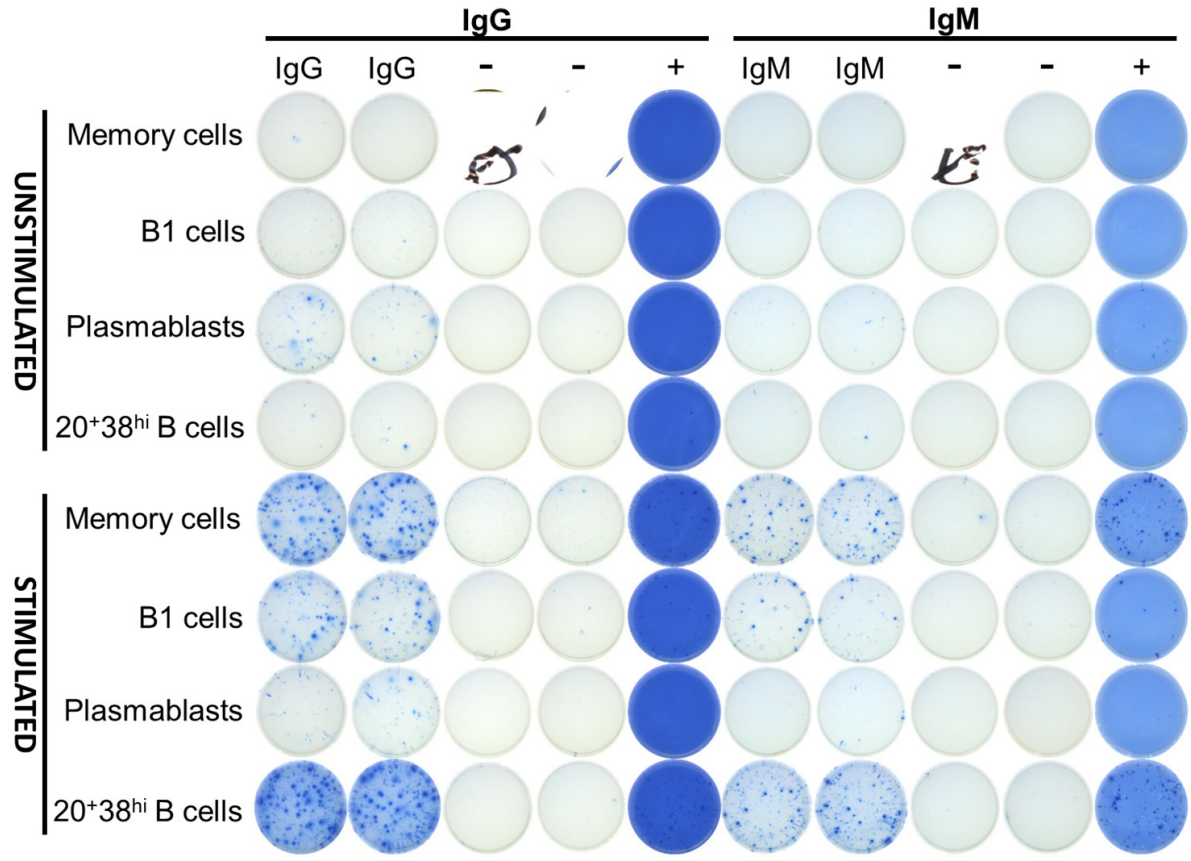

Figure 18: Representative IgG- and IgM-ELISPOT of stimulated and unstimulated B cell subtypes. Per cell type and well, the following cell numbers were seeded: Unstimulated: memory B cells: 4000, B1 cells: 560, PBs: 200, CD20$^+$CD38^{hi}: 60. Stimulated: memory B cells: 2000, B1 cells: 600, PBs: 80, CD20$^+$CD38^{hi}: 1700.

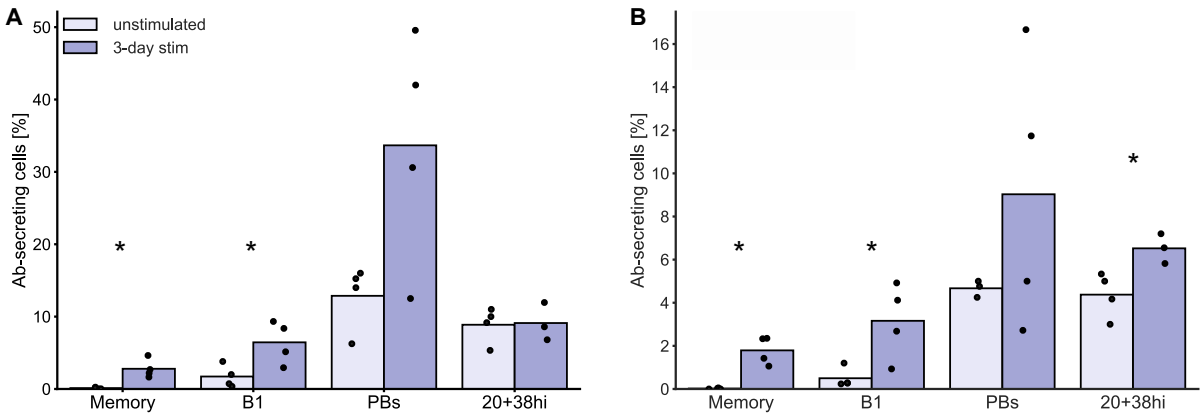

Figure 19: Frequencies of antibody-secreting cells per B cell subtype with and without 3-day stimulation with IL-2 and R848 for IgG (A) and IgM (B) as determined by ELISpot after FACS sorting. *:$p<0.05$.

Since we saw this pronounced decrease of memory B cells while $CD20^{+}CD38^{hi}$ cells increased after 72 h of stimulation, we hypothesized that $CD20^{+}CD38^{hi}$ cells might be derived from memory B cells. To verify this hypothesis, we stimulated sort-purified memory B cells that were not stimulated previously. After 72 h of stimulation, $CD20^{+}CD38^{hi}$ cell numbers were higher compared to unstimulated memory B cells that were cultured for 72 h without stimulation (Fig. 20). In turn, unstimulated memory B cells showed higher numbers of B1 cells compared to stimulated memory B cells. However due to time issues, we could not pursue these investigations any further.

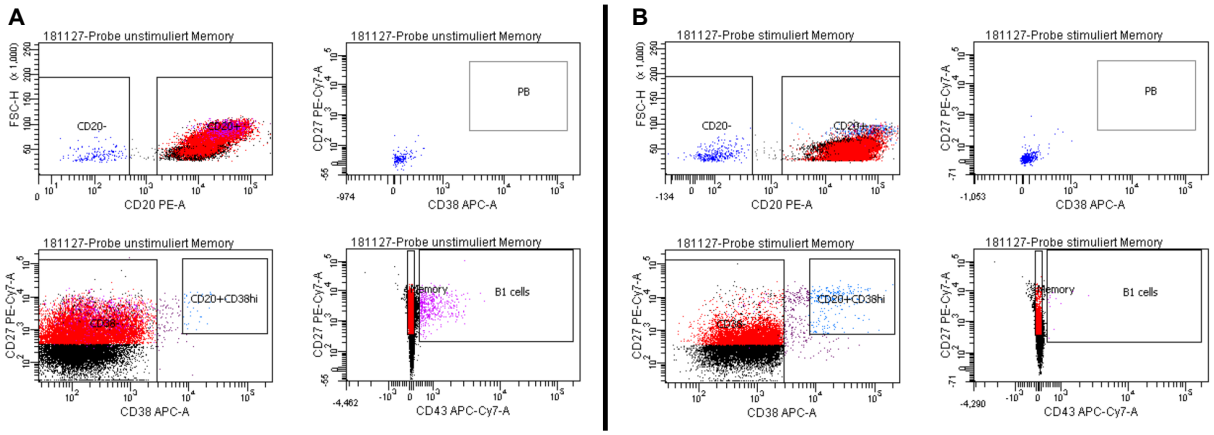

Figure 20: Sort plots of analysis of memory B cells that were cultured unstimulated for 3 days (A) and memory B cells that were stimulated for 3 days (B) following sorting. Comparison of the $CD20^{+}CD38^{hi}$ gate indicate an increase of $CD20^{+}CD38^{hi}$ cells after stimulation, while in unstimulated memory B cells seem to acquire a B1 cell-like phenotype.

Next, we sorted $CD19^+$ B cells from CIDP patients with auto-antibodies targeting paranodal proteins. Several problems occurred during the performance of experiments:
Since we received blood for the PBMC isolation from other hospitals the processing time between blood drawing and PBMC freezing resulted in very low B cell numbers, which were not sufficient for further analysis after FACS.
Although processing time had been minimized some patients still showed low PBMC and B cell quality manifesting in high numbers of erythrocytes and/or very low B cell numbers, which were not sufficient for further analysis after FACS.
Two patient PBMCs samples appeared normal concerning B cell frequencies. However, they did not show positive results in antigen-specific NF155-ELISpot. Furthermore, we were not able to evaluate whether the ELISpot protocol did work adequately since we were not in possession of a positive control.

3.2.3 Auto-antibody secretion of PBMCs in culture

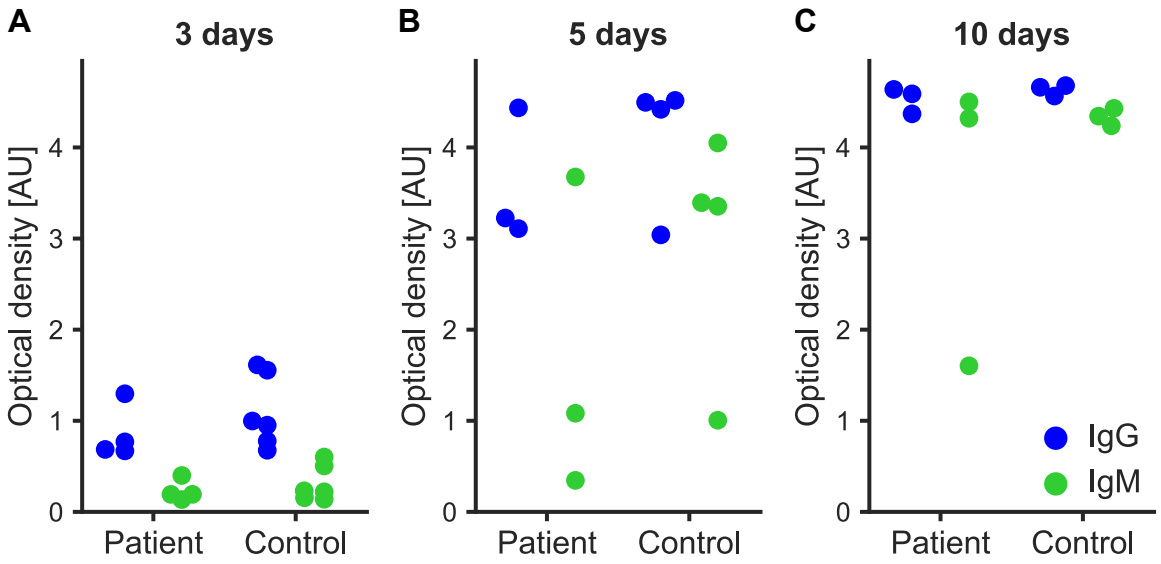

Figure 21: IgG and IgM levels of PBMC supernatants after 3, 5 and 10 days of stimulation with R848 and IL-2 *in vitro*. A) PBMCs were stimulated for 72 h and the supernatant was analyzed by ELISA. IgG and IgM levels were not different between patient samples and controls. B) After 5 days of stimulation, IgG and IgM secretion was not different between patient and control PMBCs. C) Stimulation medium of PBMCs was changed after 5 days. After 5 more days of stimulation the supernatant was taken for analysis. There were no differences between patient and control IgG and IgM levels, respectively. AU: arbitrary units.

Since the amount of patients was limiting and a positive control was not available to verify the suitability of our antigen-specific ELISpot protocol, we determined to check the supernatants of stimulated PBMCs by ELISA. We analyzed the supernatant of PBMCs that were stimulated for 72 h by antigen-specific ELISA which is an established method in our laboratory.

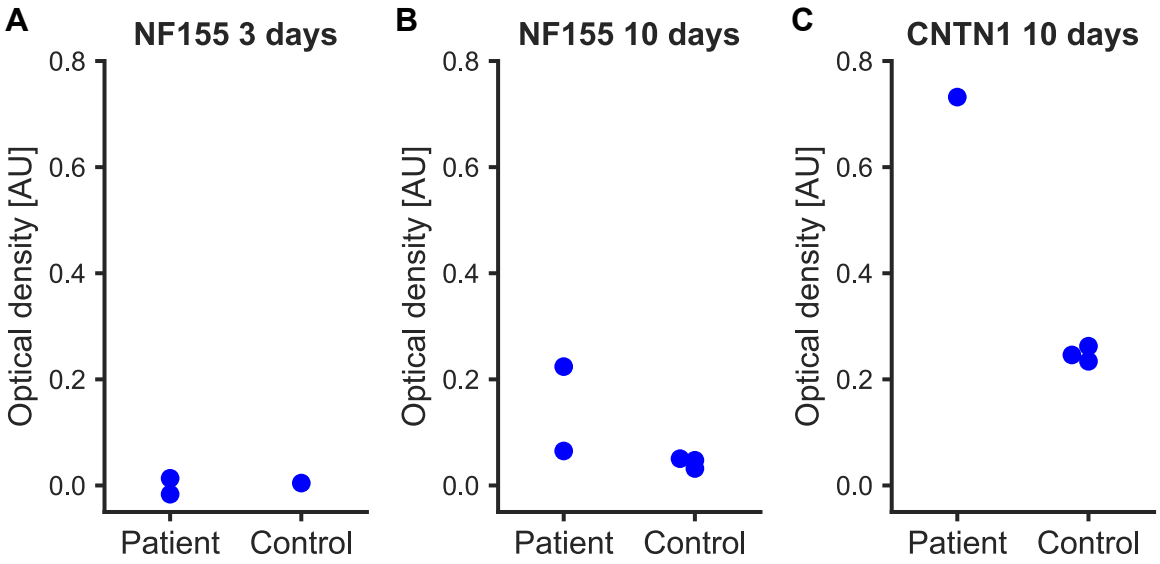

Figure 22: Antigen-specific antibodies levels of PBMC supernatants after 3 and 10 days of stimulation with R848 and IL-2 *in vitro*. A) IgG and IgM levels were not different between patient samples and controls. PBMCs were stimulated for 72 h and the supernatant was analyzed by ELISA. B) After 5 days of stimulation, IgG and IgM secretion was not different between patient and control PMBCs. C) Stimulation medium of PBMCs was changed after 5 days. After 5 more days of stimulation the supernatant was taken for analysis. There were no differences between patient and control IgG and IgM levels, respectively. AU: arbitrary units.

Although IgG and IgM levels in supernatants were comparable between patients and controls (Fig. 21 A), auto-antibody detection was not possible in the supernatants of the patient PBMCs (Fig. 22 A). It has been described that auto-antibodies in a different neurological disease, the stiff person syndrome, are detectable after 10 days of stimulation (Thaler et al., 2019). Therefore, we decided to stimulate PBMCs for 10 days to make sure that there were auto-antibody-secreting cells in the patient blood. Again, three patients compared to three controls showed no differences in IgG and IgM levels after 5 and 10 days of stimulation (Fig. 21 B, C). Antigen-specific ELISA for NF155 and CNTN1 presented increased auto-antibody levels in two out of three patients compared with controls after the 10-day stimulation which confirms that there are in fact auto-antibody-producing B cells

present in the blood (Fig. 22 B, C). To determine whether we can perform our protocol for B cell sorting with PBMCs after the 10-day stimulation, we performed the protocol with 10-day stimulated healthy donor PBMCs (Fig. 23). Following the MACS purification and the FACS sorting, B cells were still able to secrete Ig as assessed by ELISpot (Fig. 24). Frequency analysis of B cell subsets revealed that PBs, $CD20^{+}CD38^{hi}$ and B1 cells were increased while memory B cells and naive B cells did not change compared to cell that were stimulated for 3 days. Compared to unstimulated cells memory B cells and naive B cells were decreased, whereas the other three B cell subpopulations were increased (Fig. 17).

As the sort protocol was feasible with 10-day stimulated PBMCs and we detected auto-antibodies in supernatants of patient PBMCs, we once again attempted the antigen specific ELISpot with the previous positively-screened patient PBMCs. Although numbers of patient B cell subpopulations were sufficient and they secreted IgG, detection of antigen-specific auto-antibodies targeting NF155 or CNTN1 was not possible as shown in Figs. 24 and 25.

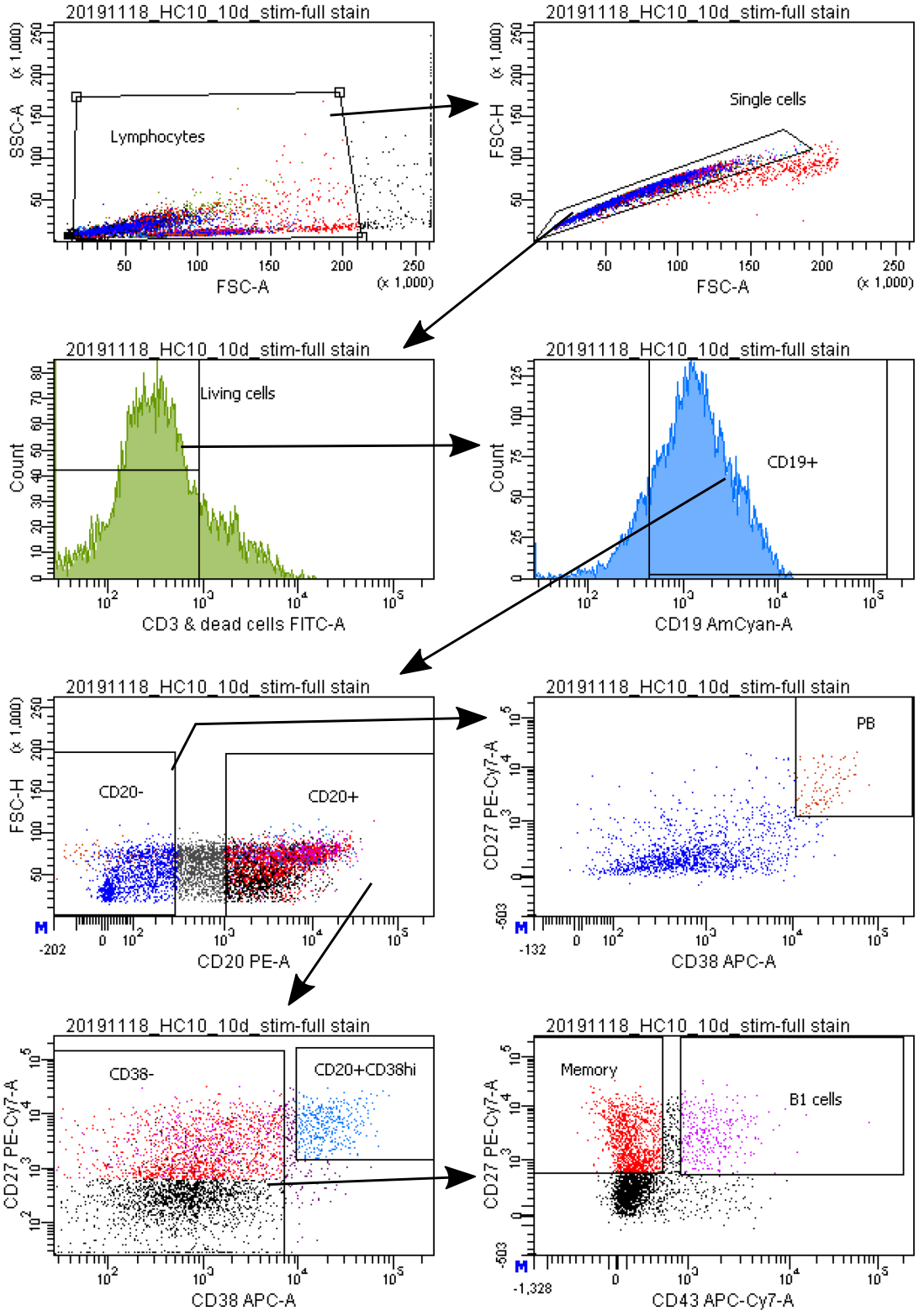

Figure 23: Representative sort plots of cell sorting of 10-day stimulated CD19$^+$ cells after MACS purification. After thawing PBMCs were stimulated with IL-2 and R848 for 10 days. Stimulated PBMCs were MACS purified to enrich CD19$^+$ cells. Compared to unstimulated cells, all subtype numbers increased except for memory B cell numbers.

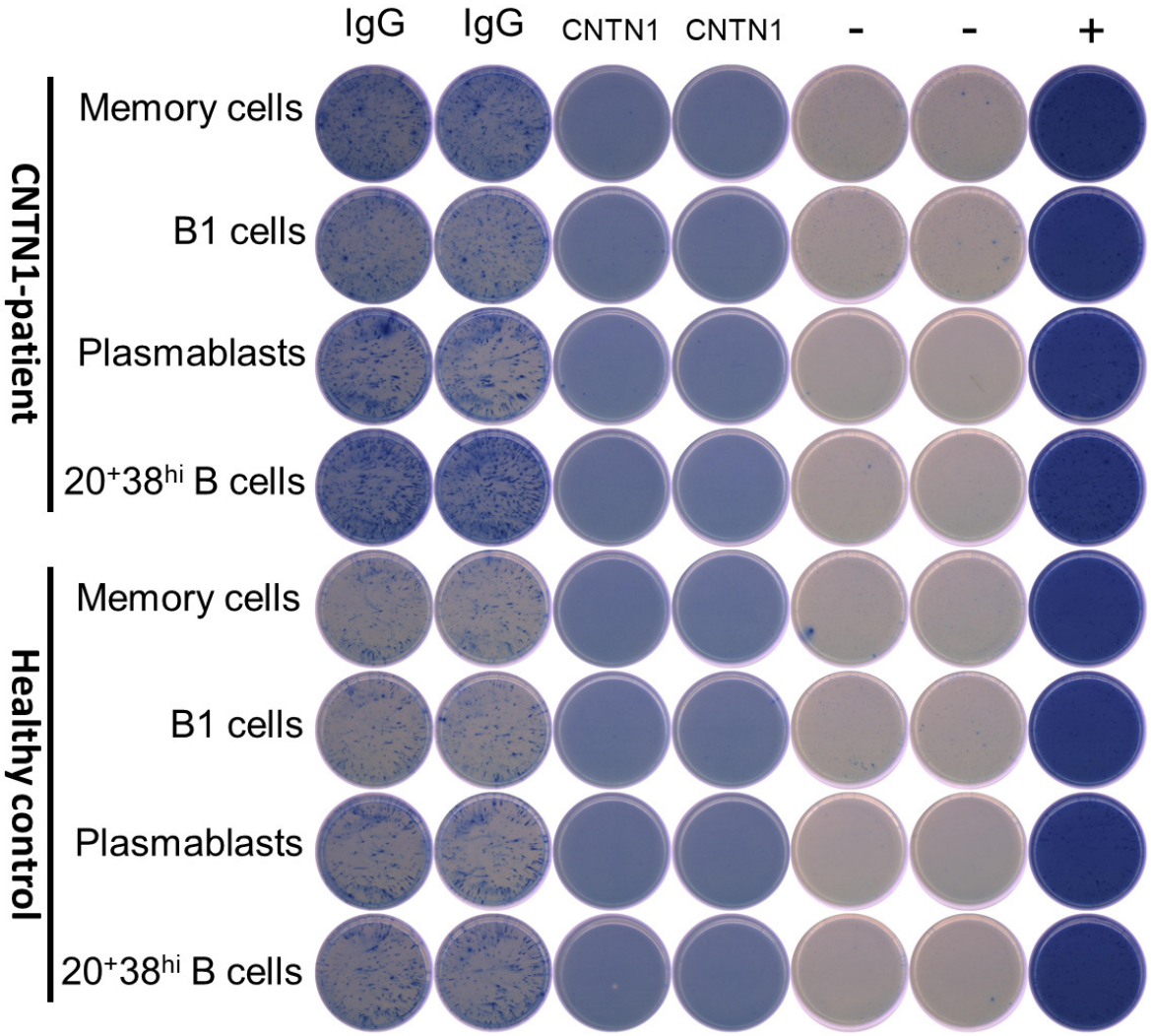

Figure 24: CNTN1-specific ELISpot after FACS sorting and MACS purification of 10-day stimulated PBMCs. Cells were seeded for 24 h. No spots could be detected in the CNTN1-coated wells, while IgG-coated wells show antibody-secreting activity of seeded cells. Per cell type and well, the following cell numbers were seeded: CNTN1-patient: memory B cells: 6000, B1 cells: 3500, PBs: 1000, $CD20^{+}CD38^{hi}$: 1800. Healthy control: memory B cells: 3200, B1 cells: 3200, PBs: 1000, $CD20^{+}CD38^{hi}$: 1600.

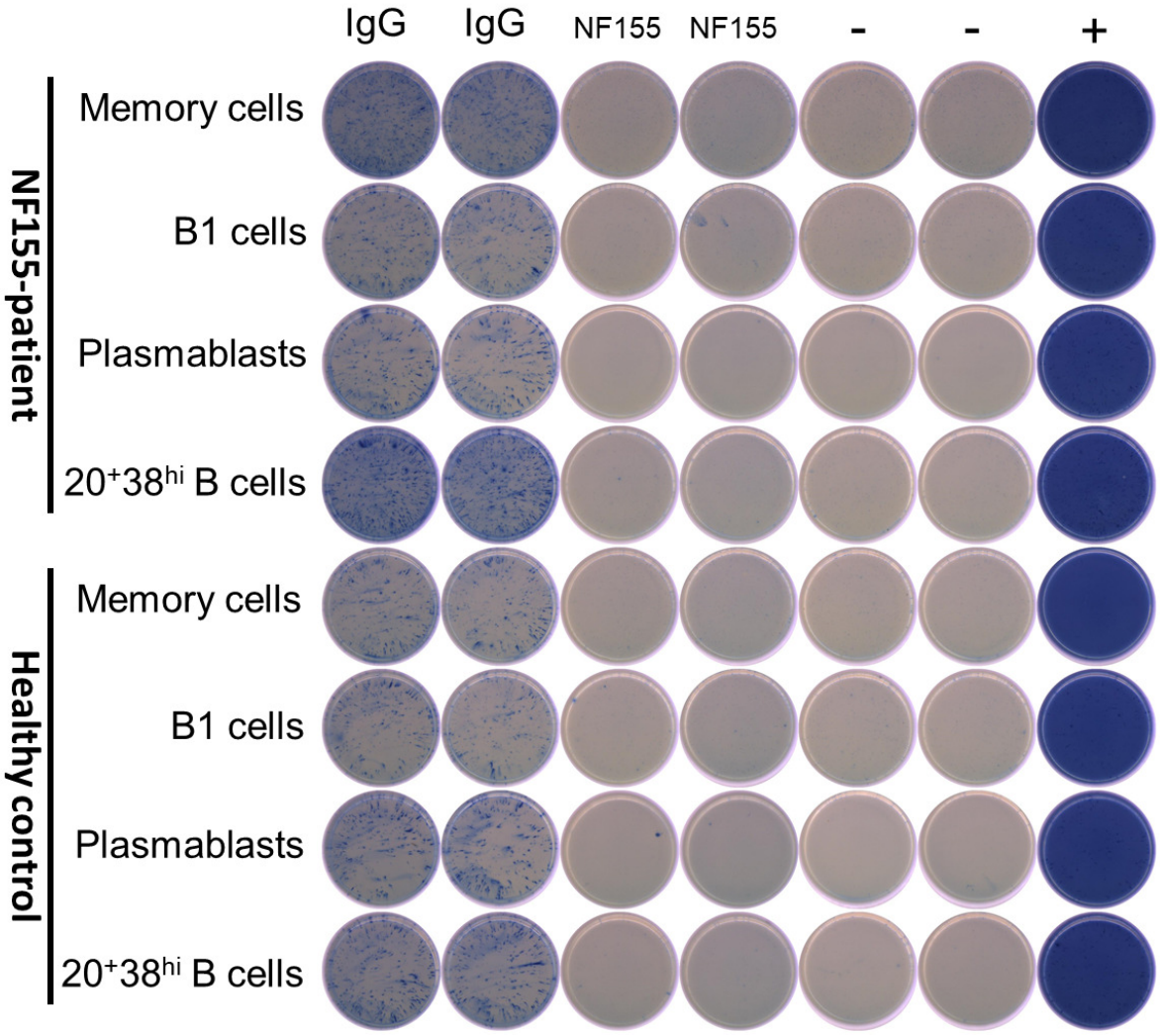

Figure 25: NF155-specific ELISpot after FACS sorting and MACS purification of 10-day stimulated PBMCs. Cells were seeded for 24 h. No spots could be detected in the CNTN1-coated wells, while IgG-coated wells show antibody-secreting activity of seeded cells. Per cell type and well, the following cell numbers were seeded: NF155-patient: memory B cells: 6400, B1 cells: 2800, PBs: 800, $CD20^{+}CD38^{hi}$: 3800. Healthy control: memory B cells: 3200, B1 cells: 3200, PBs: 1000, $CD20^{+}CD38^{hi}$: 1600.

3.3 CMT1A study

In clinical trials testing medication for the treatment of CMT1A, disease severity has been predominantly evaluated using scores that examined clinical and functional parameters (Attarian et al., 2014; Gess et al., 2015; Lewis et al., 2013; Micallef et al., 2009; Pareyson et al., 2011). The actual nerve damage however is not assessed in these parameters. With skin punch biopsies it is possible to investigate nerve damage in a minimally invasive manner (Doppler et al., 2013; Lauria et al., 2009; Sommer, 2008). In CMT1A patients, it has been shown that cutaneous innervation is reduced (Duchesne et al., 2018; Nolano et al., 2015). In these studies, only a few parameters or small numbers of subjects were investigated, though. In order to find objective and reproducible biomarkers that assess the actual nerve damage we investigated a series of parameters in glabrous skin from 48 CMT1A patients and compared them to 45 healthy controls, 16 SFN patients and 7 CIDP patients. Furthermore, we received and analyzed follow-up biopsies from six CMT1A patients.

3.3.1 Identification of possible biomarkers for assessment of disease severity

Patients

Basic clinical and demographic data are listed in Table 1. In the CMT1A group of 48 subjects, disease severity covered a range from mild to severe as assessed by the CMTNSv2 and correlated with age (R=0.402, p<0.005, Fig. 26).

Although the CMT1A group showed a significantly younger age than the healthy control group with 45 subjects, we considered this difference small. As a control for a classic ax-

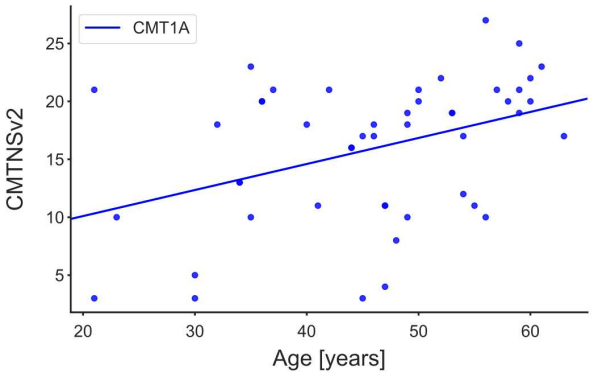

Figure 26: Correlation between age and CMTNSv2 in CMT1A patients (p<0.005, R=0.402). This figure has been previously published in *Hartmannsberger et al. (2020).*

Table 1: Demographic and skin biopsy data. Values are medians (range). CMTNSv2: Charcot-Marie-Tooth Neuropathy Scale version 2, IENFD: intraepidermal nerve fiber density.

Medians (range)	CMT1A	CIDP	SFN	Controls	Ranksums CMT1A - Control
Sample numbers	n=48	n=7	n=16	n=45	-
Age [years]	47 (21-63)	60 (43-76)	51 (31-63)	54 (22-64)	p<0.05
Sex [m:f]	20:28	6:1	6:10	21:24	-
CMTNSv2	18 (3-27)	-	-	-	-
IENFD [number/mm]	3.7 (0.0-17.3)	6.1 (2.7-7.5)	5.85 (0.3-15.3)	5 (0.8-24.9)	p<0.01
Merkel cell density [number/mm]	0.50 (0-3.5)	0.10 (0-6.5)	1.05 (0-6.7)	1.10 (0-11.1)	p<0.05
Fraction of denervated Merkel cells CMT1A: 39, CIDP: 5 SFN: 12, Con: 40	0.80 (0-1)	0.30 (0-1)	0.30 (0-0.7)	0.20 (0-1)	p<0.01
Meissner corpuscle density [number/papilla]	0.037 (0-0.154)	0.029 (0-0.153)	0.042 (0.012-0.137)	0.053 (0-0.171)	p=0.06
Density of bundles with [number/mm2] CMT1A: 46, CIDP: 7 SFN: 15 Con: 41	4.7 (0-11.7)	2.6 (0.5-5.3)	1.9 (0-5.0)	2.4 (0-12.2)	p<0.01
Density of bundles without [number/mm2] CMT1A: 46, CIDP: 7 SFN: 15, Con: 41	1.35 (0-6.3)	1.60 (0-6.2)	1.60 (0-5.1)	1.30 (0-6.0)	p=0.7
Node numbers	164	34	75	189	-
Axonal diameter [µm]	1.48 (0.56-3.7)	1.38 (0.74-3.7)	1.67 (0.56-3.7)	1.48 (0.74-4.81)	p=0.08
Node length [µm]	1.1 (0.37-2.96)	1.5 (0.56-12.95)	1.3 (0.56-4.26)	1.3 (0.56-4.81)	p<1x10-8
Paranode length [µm]	8.3 (3.1-16.6)	9.7 (5.7-22.6)	8.5 (4.8-47.9)	9.1 (5.4-22.4)	p<0.001
Asymmetry index [%]	14 (0-100)	11.8 (0-44.8)	11.1 (0-82.8)	12.35 (0-100)	p=0.5
Ratio node length/diameter	0.70 (0.2-2.2)	0.84 (0.42-11.67)	0.78 (0.2-3.33)	0.80 (0.23-6.5)	p<1x10-4
Fraction of long nodes	9.80%	38.20%	37.30%	25.40%	Binom-test: p < 1x10-6
Langerhans cell density [number/mm] Con: 44	10.0 (2.5-37.6)	14.6 (8.3-28.5)	8.4 (6.0-20.6)	9.9 (1.3-131.2)	p=0.4

onal neuropathy, biopsies from 16 SFN patients with comparable age and sex distribution were collected. To compare our CMT1A cohort to a classic demyelinating neuropathy cohort, 7 samples from CIDP patients with similar sex distribution were included. The CIDP age was significantly higher than the CMT1A age due to later disease onset in CIDP patients.

Intraepidermal nerve fiber density

CMT1A patients showed a decreased IENFD compared to healthy controls (Fig. 27 A, Table 1). Furthermore, IENFD was lower in males than in females in both, the CMT1A and the healthy control groups, respectively (Fig. 27 B). Since the male and female groups were small cohorts (n=20-28), separate correlation analyses by sex were not performed. Correlation analyses of IENFD with age revealed inverse correlation in the control (R=-0.51, $p<0.0005$, Fig. 27 C) but no correlation in the CMT1A group (R=-0.22, p=0.13, Fig. 27C). Interestingly, in the CMT1A cohort, the CMTNSv2 correlated inversely with the IENFD (R=-0.29, $p<0.05$, Fig. 27 D). Representative micrographs of skin sections stained with anti-PGP9.5 are shown in Fig. 27 E, F. In the control section more intraepidermal nerve fibers are present than in the CMT1A section.

Biopsies from CMT1A patients were only half the size of the ones from the other groups. Therefore, we checked if the IENFD was independent from the analyzed epidermis length. Indeed, there was no correlation between the analyzed length and the IENFD in both groups (Controls: R=0.08, p=0.6, CMT1A: R=0.13, p=0.4, Fig. 33 A).

These baseline results indicate that the IENFD can be used to evaluate the disease severity and might be a potential measure to evaluate the disease progression, as well.

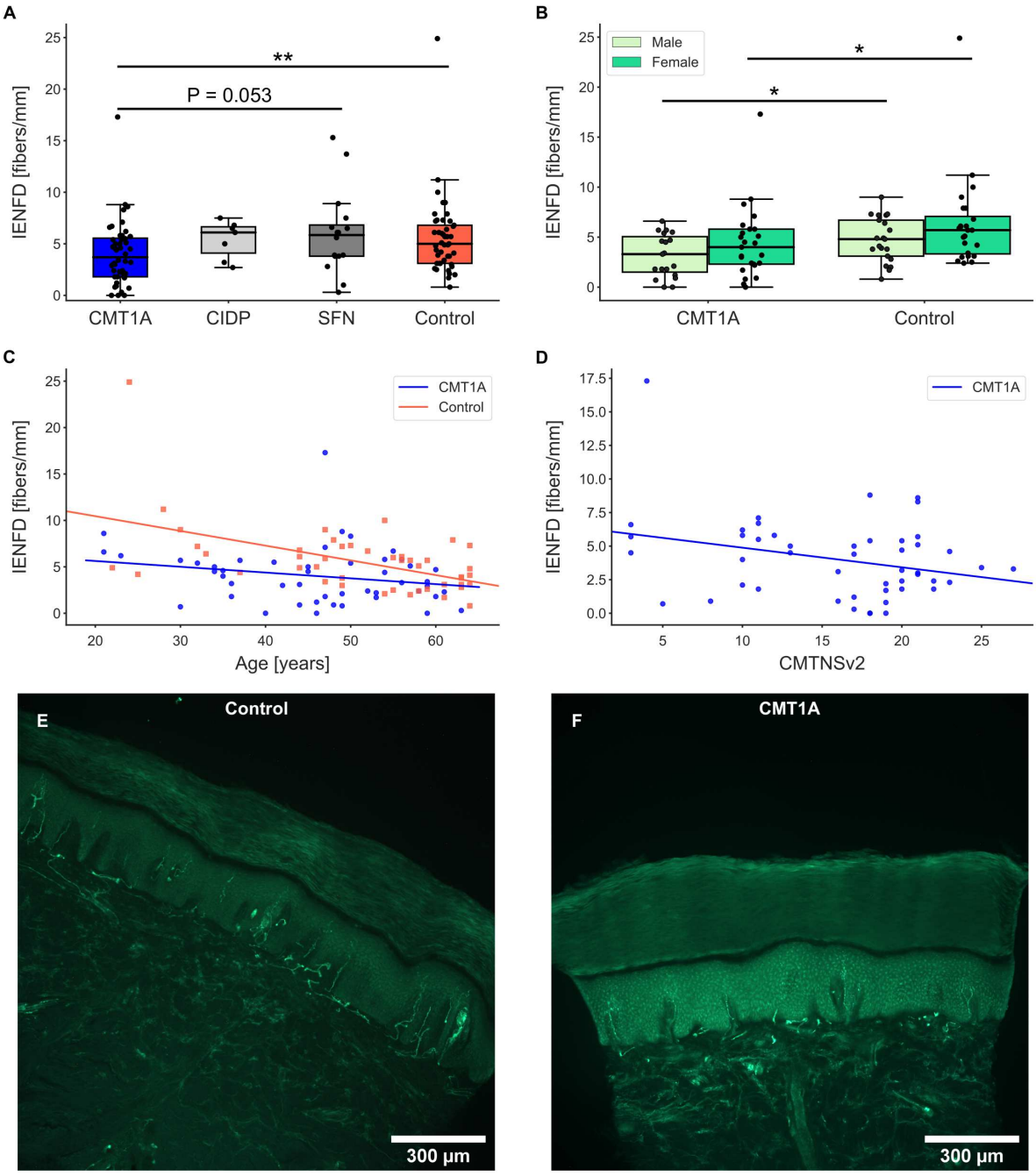

Figure 27: Intraepidermal nerve fiber density (IENFD) in CMT1A patients compared to CIDP, SFN and healthy controls. A) There was a significant reduction of IENFD in CMT1A compared to the healthy control group; **p<0.01. B) In CMT1A and controls, IENFD of females showed a trend to be higher compared to the IENFD of men of the same group (n. s.). Significant differences were still present between CMT1A and controls when divided into males and females; *p<0.05. C) In controls, IENFD showed a strong inverse correlation with age (p<0.001, R=-0.51), but not in CMT1A patients (p=0.1, R=-0.22). D) In CMT1A, IENFD correlated negatively with the CMTNSv2 (p<0.05, R=-0.29). E, F) Representative micrographs of skin sections labeled with anti-PGP9.5 from a control (E) and a CMT1A patient (F). This figure has been previously published in *Hartmannsberger et al. (2020)*.

Dermal nerve bundle densities

The density of bundles without myelinated fibers did not show differences between the groups (Fig. 28 A). Unexpectedly, the density of bundles with myelinated fibers was increased in the CMT1A group compared to the SFN and healthy control groups (Fig. 28 B). To make sure that these results were not caused by differing section areas between the groups, we correlated the section areas with the bundle densities of the control and CMT1A groups. In fact, the dermis areas correlated with the densities of bundles with myelinated nerve fibers in both the control and CMT1A group (Control: R=-0.276, p=0.08, CMT1A, R=-0.414, p<0.005; Fig. 33 B) but not with the densities of bundles without myelinated fibers (Control: R=-0.085, p=0.6, CMT1A: R=-0.191, p=0.2; Fig. 33 C).

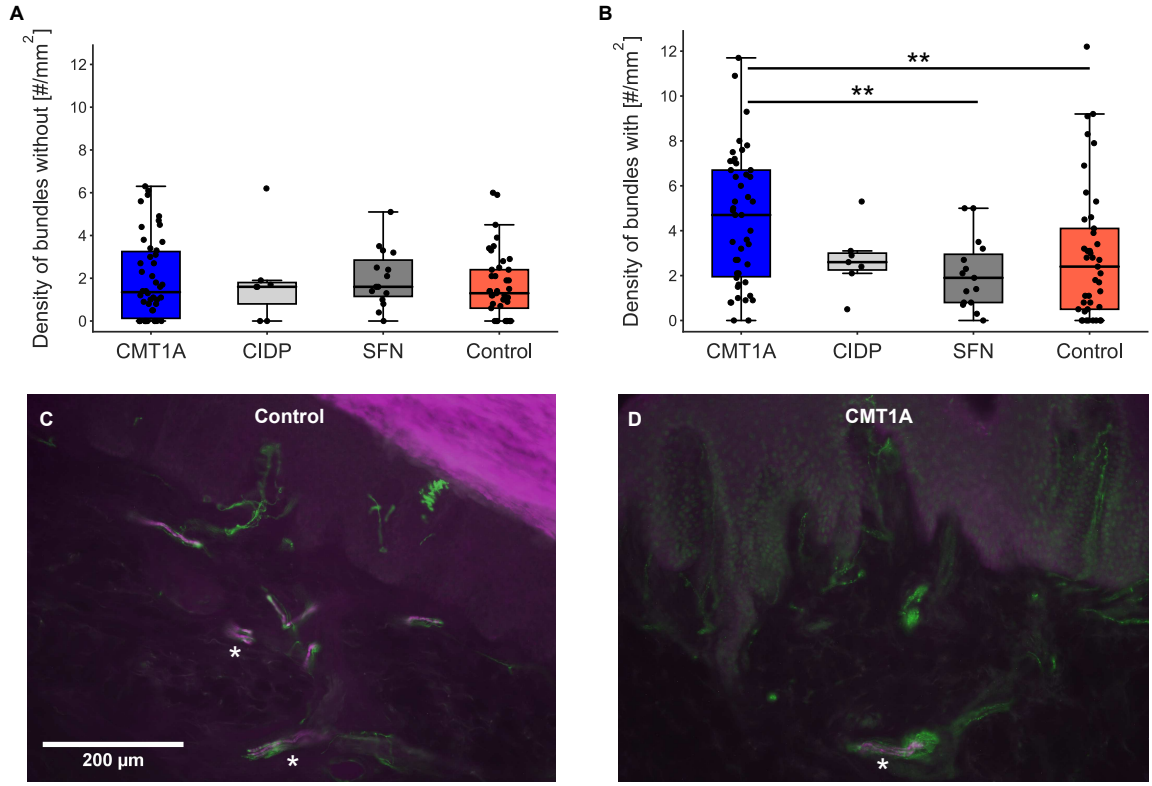

Figure 28: Density of bundles without (A) and with (B) myelinated fibers. A) There were no significant differences in the bundle densities without myelinated nerve fibers between the groups. B) Elevated density of bundles with myelinated fibers in CMT1A patients compared to SFN and control groups; **p<0.01. C, D) Micrographs of sections stained with anti-PGP9.5 (green) and anti-MBP (magenta) from a healthy control (C) and a CMT1A patient (D). Asterisks mark nerve bundles with myelinated fibers. This figure has been previously published in *Hartmannsberger et al. (2020)*.

Exemplary micrographs of skin sections immunostained with anti-MBP and anti-PGP9.5 are shown in Fig. 28 C, D.

We considered the density of bundles with myelinated fibers as not suitable as an outcome measure because it was dependent from the analyzed dermis area.

Meissner corpuscle density

An alternative approach to assess the involvement of myelinated Aβ-fibers in glabrous skin is the determination of mechanoreceptor densities.

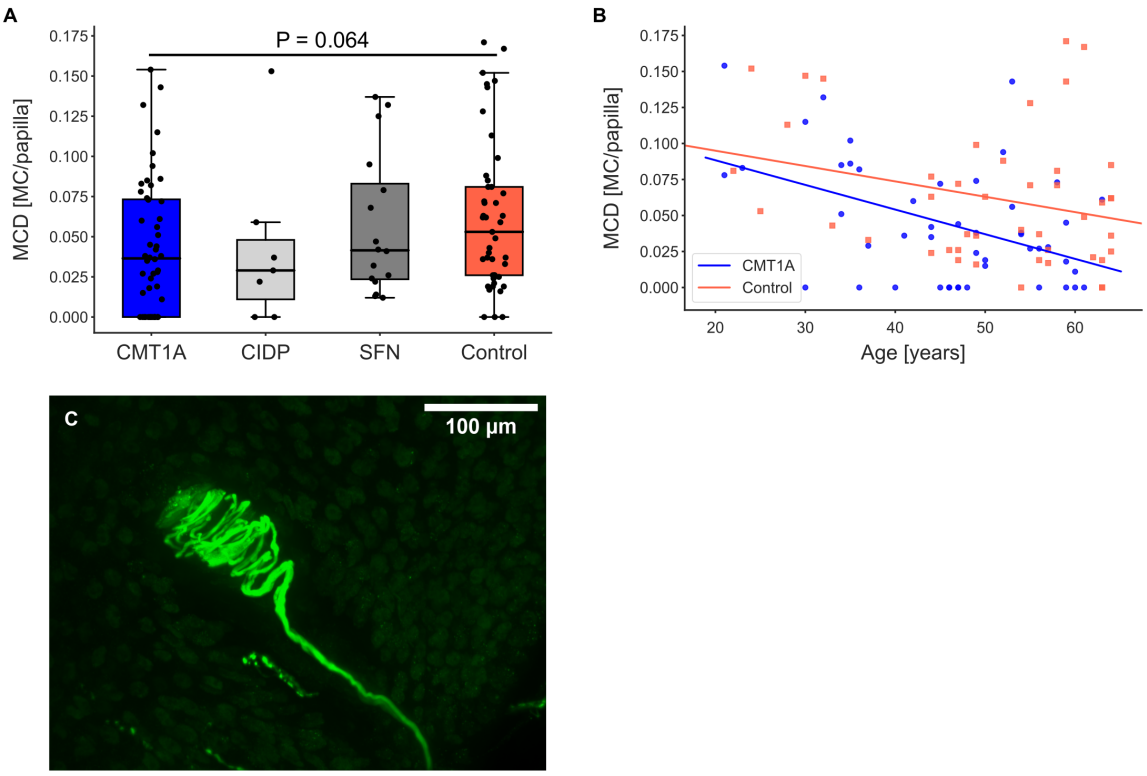

Figure 29: Meissner corpuscle density (MCD) and correlations with age and IENFD. A) Meissner corpuscle density shown as MC per papilla is reduced in CMT1A compared to controls, however not significantly. B) MCD correlates strongly, negatively with age in CMT1A ($p<0.005$ R=-0.452), but not in controls ($p=0.07$, R=-0.276). C) Image of Meissner corpuscle in a papilla stained with anti-PGP9.5. This figure has been previously published in *Hartmannsberger et al. (2020)*.

To investigate the involvement of large Aβ-fibers, we determined the density of Meissner corpuscles. Furthermore, we checked if degeneration of Meissner corpuscles could be objectively detected by immunohistochemical staining.

We examined whether Meissner corpuscles were devoid of either the inner bulb stained

with anti-S100 or the enwrapping nerves stained with anti-PGP9.5. Out of 235 Meissner corpuscles from 98 samples, only five lacked the enwrapping nerve structure.

Meissner corpuscle density showed a trend to be decreased in the CMT1A group compared to healthy controls (p=0.064, Fig. 29 A, Table 1). In addition, Meissner corpuscle density correlated inversely with age in the CMT1A group (R=-0.452, p<0.005, Fig. 29 B), whereas in controls the inverse correlation with age was not as strong and did not reach statistical significance (R=-0.276, p=0.07, Fig. 29 B).

Also with the Meissner corpuscle density, we made sure that the obtained density was independent from the analyzed numbers of papillae. Indeed, the Meissner corpuscle densities of the control and the CMT1A groups did not correlate with the evaluated papillae numbers (Control: R=-0.190, p=0.2; CMT1A: R=-0.117, p=0.4; Fig. 33 D).

In Fig. 29 C an intact Meissner corpuscle is shown. Since the Meissner corpuscle density correlated with age in CMT1A, it might be an additional helpful measure to evaluate the disease severity in CMT1A.

Merkel cell density

Another mechanoreceptor type involving large Aβ-fibers are Merkel cells. They are innervated by unmyelinated nerve endings from Aβ-fibers (Boulais et al., 2007). Merkel cell density was reduced in CMT1A patients compared to healthy controls (p<0.05, Fig. 30 A). Furthermore, different from healthy controls, which showed correlations between the Merkel cell density with the Meissner corpuscle density, this correlation did not occur in the CMT1A groups (Control: R=0.330, p<0.05, CMT1A: R=0.091, p=0.5; Fig. 30 B).

For evaluation of degeneration of Merkel cells, we determined the fraction of denervated Merkel cells, since we considered them degenerating. Only samples with at least one Merkel cell were analyzed, which applied to 39 CMT1A, 5 CIDP, 12 SFN and 40 control samples (Table1). The fraction of denervated Merkel cells was increased in the CMT1A groups compared to the SFN and the control groups (Fig. 30 C). In addition, the fraction of denervated Merkel cells correlated with age in the CMT1A group (R=0.373, p<0.05) but not in the control group (R=0.059, p=0.7, Fig. 30 D).

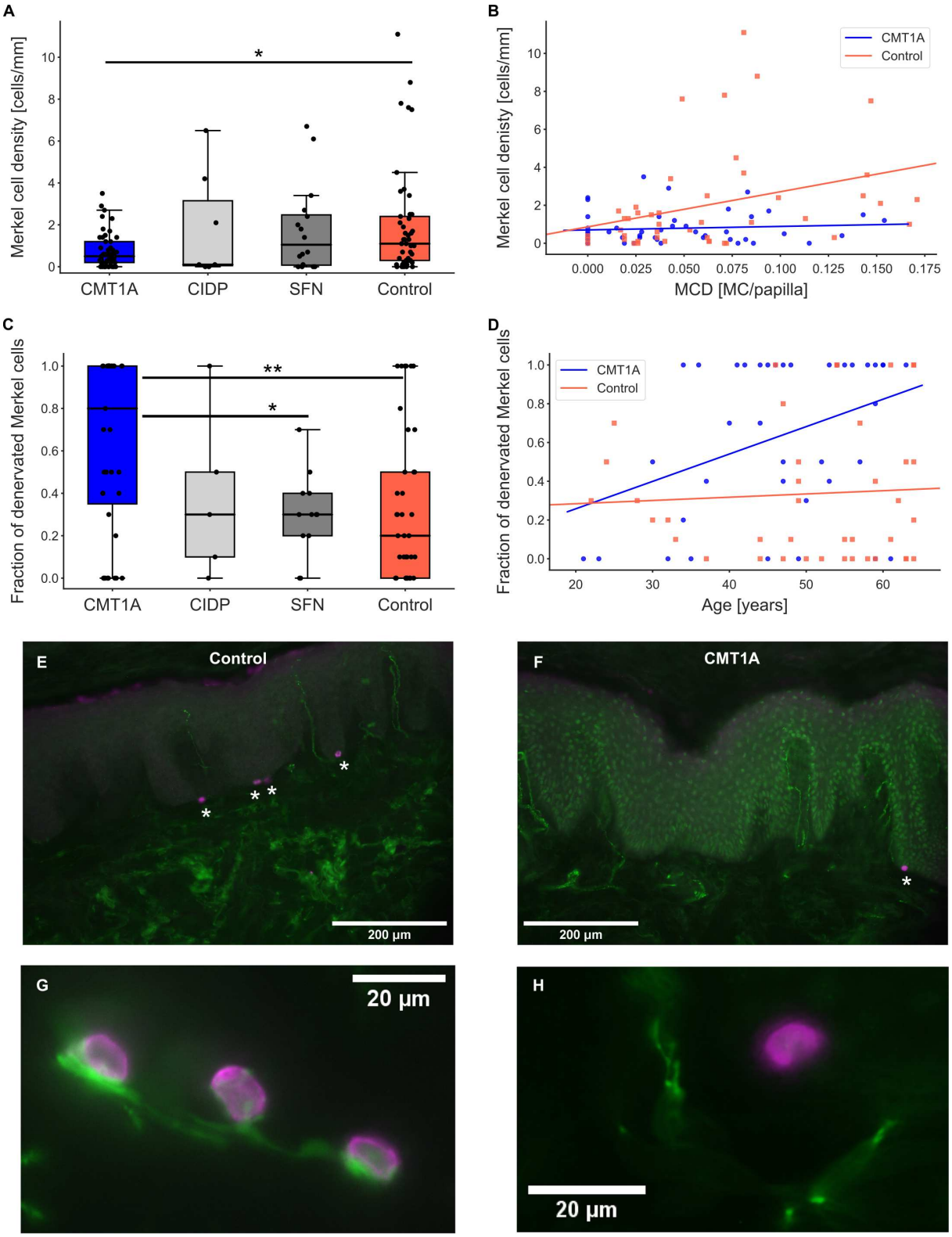

Figure 30: Merkel cell density and fraction of denervated Merkel cells. A) Reduced Merkel cell density in CMT1A compared to healthy controls; *p<0.05. B) Merkel cell density correlated with Meissner corpuscle density (MCD) in controls (p<0.05, R=0.330), but not in CMT1A patients (p=0.5, R=0.091). C) The fraction of denervated Merkel cells was significantly elevated in CMT1A compared to the SFN and control groups; *p<0.05, **p<0.01. D) The fraction of denervated Merkel cells correlated with age in the CMT1A group (p<0.05, R=0.373), but not in the controls (p=0.7, R=0.059). E-H) Micrographs of Merkel cells (magenta) and nerve fibers (green). Skin sections of a representative healthy control (E) and a CMT1A patient (F). Images of innervated Merkel cells (G) in comparison to a denervated Merkel cell (H) are shown. This figure has been previously published in *Hartmannsberger et al. (2020)*.

Representative micrographs of a control section and a CMT1A section stained with anti-CK20 and anti-PGP9.5 are depicted in Fig. 30 E, F. Normally innervated Merkel cells are shown in Fig. 30 G, whereas in Fig. 30 H an example of a denervated Merkel cell is shown. There were no correlations between the fraction of denervated Merkel cells and the CMTNSv2 in the CMT1A group. However, in the control group the fraction of denervated Merkel cells correlated inversely with the Merkel cell density (Fig. 33 E). This indicates that in samples with low Merkel cell density, the remaining Merkel cells tended to be denervated and to be degenerating. This is in accordance with the Merkel cell findings in the CMT1A group, which has low density but a high fraction of denervated cells. Again, we ascertained that the obtained Merkel cell data was independent of the analyzed epidermis length (Control: R=-0.0089, p=0.8, CMT1A: R=-0.010, p=0.9; Fig. 33 F).

Nodal and paranodal parameters

For the assessment of nodal and paranodal parameters, we obtained data from five nodes of Ranvier per sample when possible. This resulted in 164 nodes from 43 CMT1A samples, 34 nodes from seven CIDP samples, 75 nodes from 15 SFN samples and 189 nodes from 42 healthy control samples. In all four groups, the diameters of the evaluated nodes of Ranvier were comparable (Fig. 31 A). The length-to-diameter ratio though was decreased in the CMT1A group compared to the three other groups (Fig. 31 B). This is in consistency with the decreased nodal length in the CMT1A group (Table 1). In addition, the CMT1A group showed a decreased fraction of long nodes compared to all other groups (Fig. 31 C). Similarly, paranodal length was also reduced in the CMT1A group when compared to the CIDP and the control groups (Fig. 31 D). In contrast, there were no differences between the groups regarding the asymmetry indices (Fig. 31 E). These nodal and paranodal parameters did neither correlate with age in controls, nor with age or the CMTNSv2 in CMT1A patients.

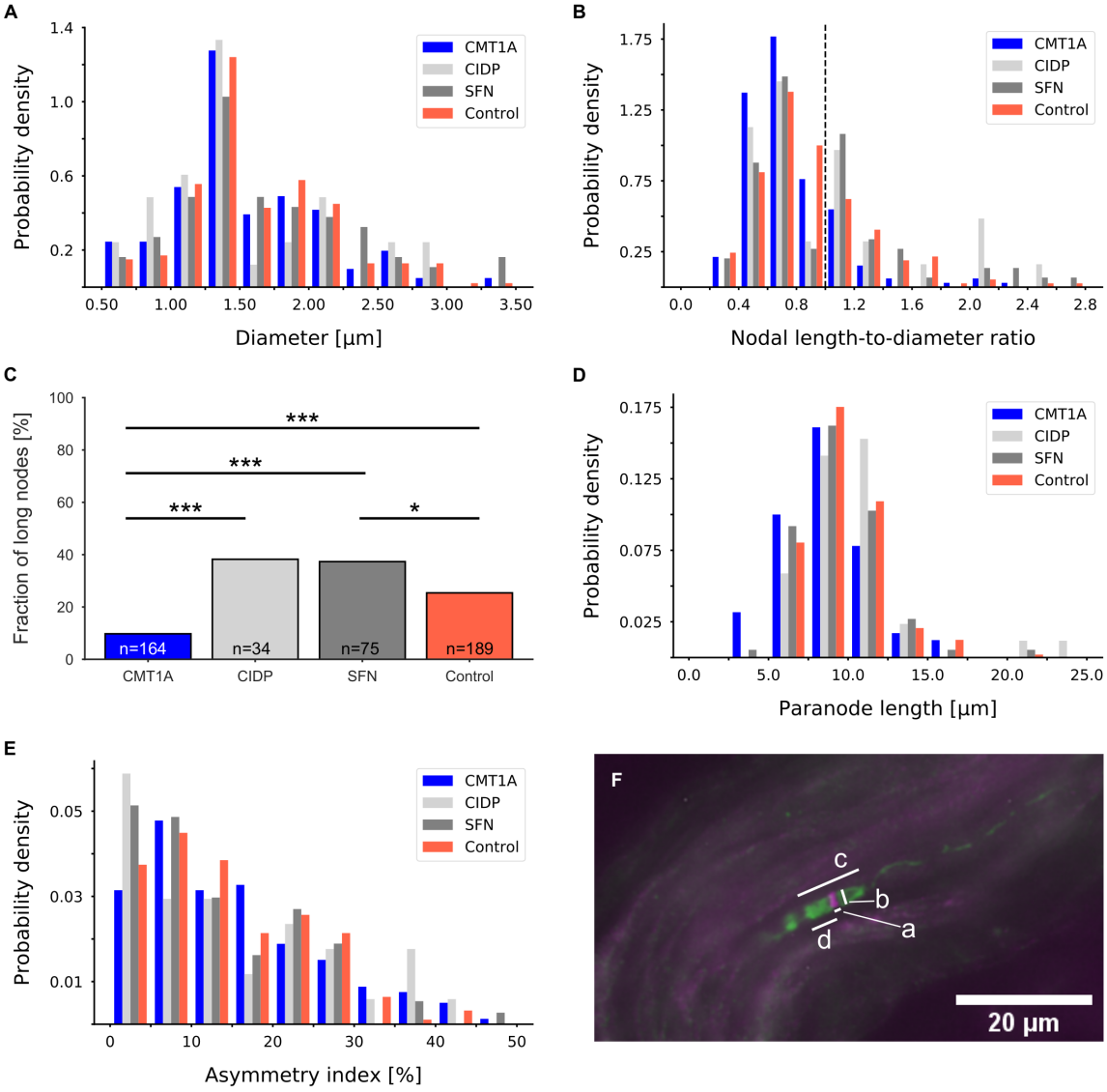

Figure 31: Nodal and paranodal parameters. A) Distributions of axonal diameters of CMT1A, CIDP, SFN and healthy control groups did not show any significant differences. B) Distributions of ratios between the measured nodal gap length and the nodal diameter. Nodes with a ratio greater than 1 were considered long. The dashed line marks the ratio of 1. There were significantly fewer long nodes in the CMT1A group than in the other groups (CIDP: $p<0.005$, SFN: $p<0.001$, Con: $p<0.00005$). C) Fractions of long nodes were depicted; binomial test *$p<0.05$, ***$p<0.001$. D) Distributions of paranodal lengths. In CMT1A patients, paranodal length was significantly decreased compared to the CIDP and control groups (CIDP: $p<0.01$, SFN: $p=0.08$, controls: $p<0.001$). E) Distributions of asymmetry indices did not differ between the groups. F) Representative micrograph of node of Ranvier double-labeled with anti-pan-sodium channel (magenta) and anti-Caspr (green). Measurements were taken as indicated with a: nodal length, b: axonal diameter, c: paranodal length, d: length of hemiparanode. This figure has been previously published in *Hartmannsberger et al. (2020)*.

Langerhans cell density

In a previous study, the Langerhans cell density in skin from the distal leg was reported to be decreased in CMT1A patients in comparison to controls (Duchesne et al., 2018). In comparison to controls or the SFN group, Langerhans cell density was not different in the CMT1A group. In the CIDP group, Langerhans cell density was increased compared to the SFN and CMT1A groups (Fig. 32). Neither in the CMT1A nor in the control groups were there correlations between the Langerhans cell density and the analyzed epidermis length (Control: R=-0.217, p=0.2, CMT1A: R=-0.084, p=0.6, Fig. 33 G).

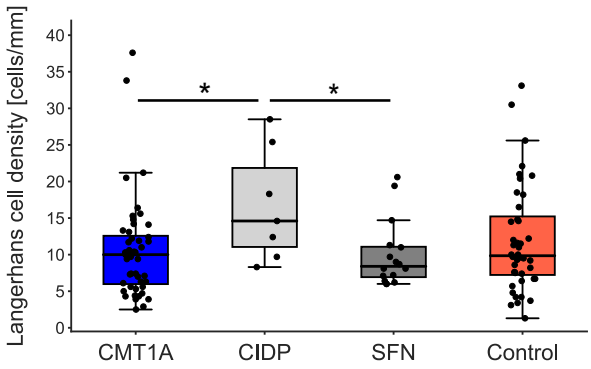

Figure 32: Langerhans cell density was not changed in CMT1A compared to SFN or controls. In CIDP patients, Langerhans cell density was increased compared with CMT1A and SFN patients; *p<0.05. This figure has been previously published in *Hartmannsberger et al. (2020)*.

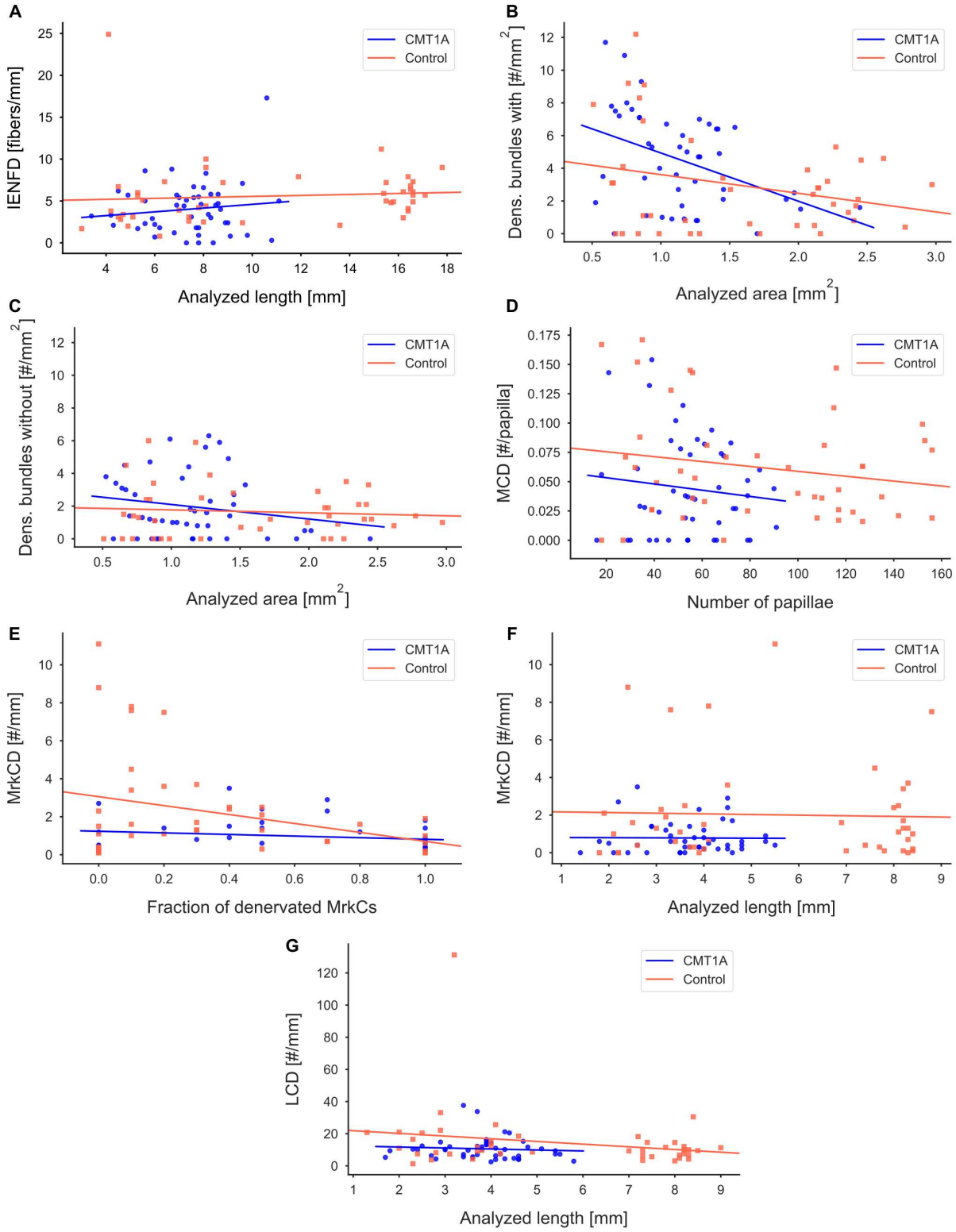

Figure 33: Correlation analyses between cutaneous parameters in healthy controls and CMT1A patients. MCD: Meissner corpuscle density, MrkCD: Merkel cell density, MrkCs: Merkel cells, LCD: Langerhans cell density. This figure has been previously published in the supplement of *Hartmannsberger et al. (2020)*.

3.3.2 No changes of cutaneous parameters detectable in follow-up analyses of a very small cohort

Two years following the baseline biopsy collection, six CMT1A patients agreed to have another biopsy performed (Fig. 34 A). Two of them were female with ages of 59 and 49 years and CMTNSv2 of 13 and 4, respectively. Four patients were male with the ages/CMTNSv2 of 62/22, 52/17, 58/30, 38/22.

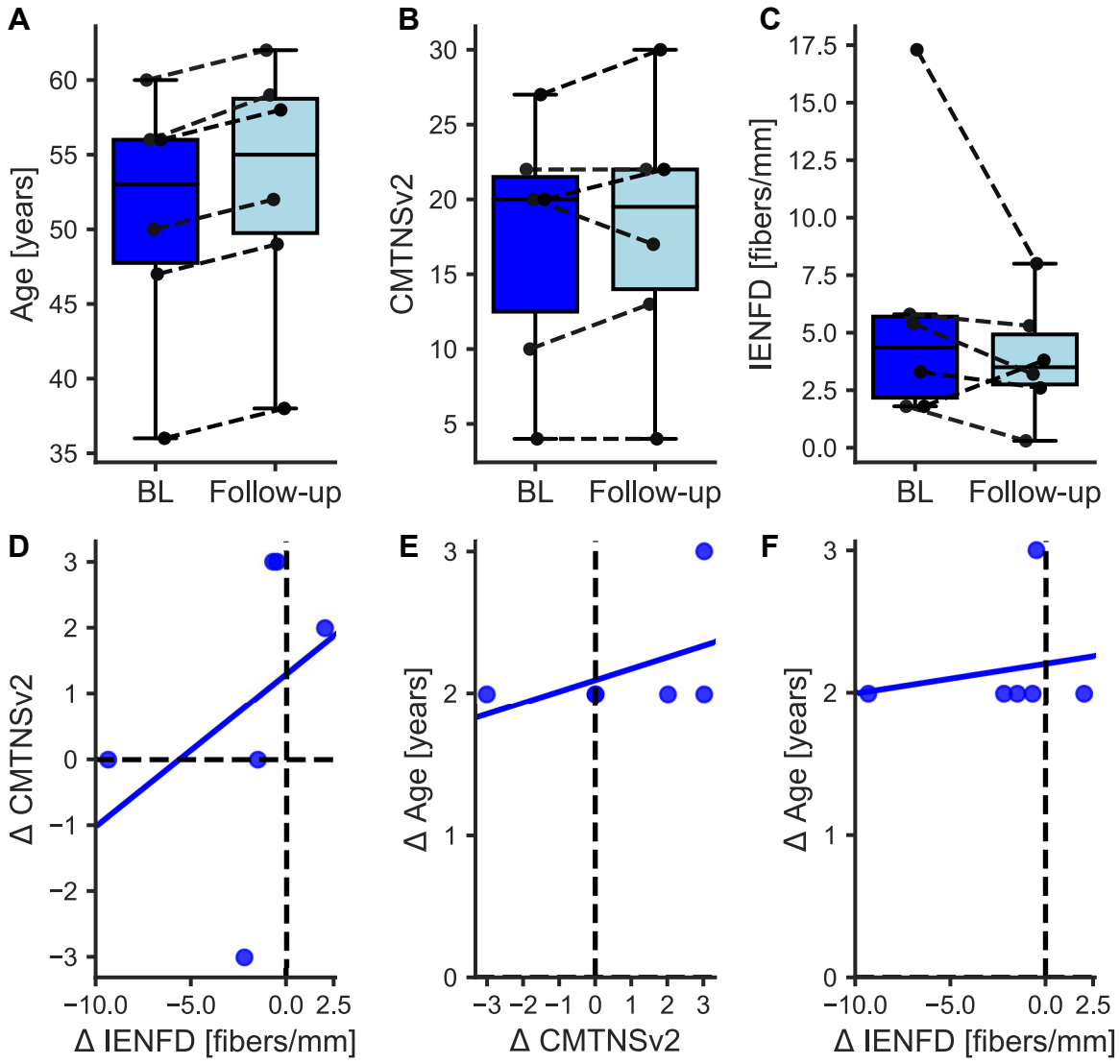

Figure 34: No significant changes and correlations of age, CMTNSv2 and IENFD over time. A) Follow-up biopsies were collected 2 years after the baseline biopsies. B) CMTNSv2 did not change over time. C) IENFD showed a trend of decrease which was not significant. D-F) Analyses of the changes of CMTNSv2, IENFD or age did not reveal significant correlations; D) p=0.117, R=0.71. E) p=0.269, R=0.54. F) p=0.441, R=0.39. A-C) dashed lines connect data points from the same samples. D-E) dashed lines mark the 0 of x- and y-axes. BL: baseline.

The disease severity as assessed by the CMTNSv2 was increased in three of these subjects, stayed stable in two and improved in one patient. Overall, the distribution did not change over time (p=0.872, Fig. 34 B).

IENFD was revealed as a possible measure to evaluate disease severity in our baseline analyses. Although the IENFD of the six follow-up samples showed a trend to be decreased, it was not significant (p=0.6, Fig. 34 C). To check if the changes over time of each of these parameters correlated with each other, we performed correlation analyses. Even though the correlation coefficient between ΔCMTNSv2 and ΔIENFD was high, it did not reach statistical significance (R=0.71, p=0.117, Fig. 34 D). Correlation analyses between Δage with ΔCMTNSv2 and ΔIENFD showed no correlations, respectively (Δ CMTNSv2: R=0.54, p=0.269, Fig. 34 E; ΔIENFD: R=0.39, p=0.441, Fig. 34 F).

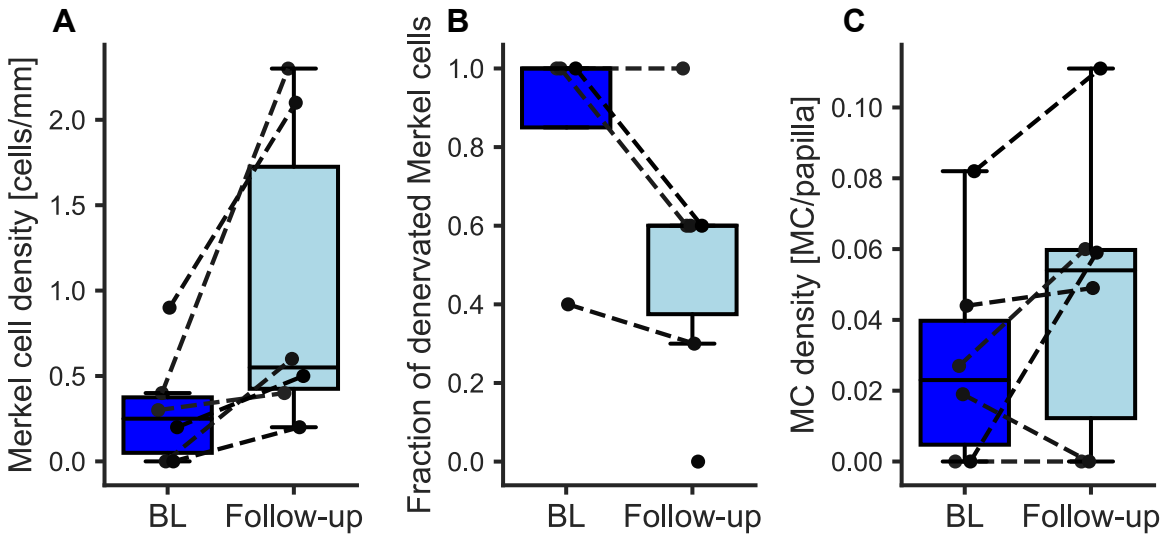

Figure 35: No significant changes of Merkel cell (A) and Meissner corpuscle (C) densities and the fraction of denervated Merkel cells (B). A) Merkel cell density was not changed after two years; p=0.078. B) The fraction of denervated Merkel cells was not changed significantly over time. At baseline analysis no Merkel cell were detected in one sample; p=0.149. C) Meissner corpuscle (MC) density was not changed; p=0.423. BL: baseline. Dashed lines connect data points from the same samples.

Since also Merkel cell parameters and the Meissner corpuscle density were considered possible additional outcome measures for the disease severity, we analyzed them regarding their potential as markers for disease progression using the follow-up biopsies. Surprisingly, Merkel cell density showed a clear trend to be increased over time, however not statistically significant (p=0.078, Fig. 35 A). In accordance with the increased Merkel

cell density, the fraction of denervated Merkel cells tended to be decreased (p=0.149, Fig. 35 B). Similarly, Meissner corpuscle density showed a tendency of a slight increase over time, but this neither showed statistical significance (p=0.423, Fig. 35 C).

4 Discussion

4.1 Passive transfer experiments: No effects of patient anti-CNTN1 IgG on nerve roots *in vivo*

IgG4 auto-antibodies against CNTN1 from a CIDP patient have been shown to be pathogenic in naive animals in a previous study (Doppler et al., 2019). After focal, short-term intraneural injection into the sciatic nerve animals showed loss of F-waves and binding of the auto-antibodies at the paranode was detected. Since in CIDP patients, not only the distal peripheral nerves but also the nerve roots are involved (Broers et al., 2019; Ogata et al., 2015), we investigated the effect of anti-CNTN1 auto-antibodies by passive transfer experiments when injected intrathecally over a period of three weeks.

Analyses of motor and sensory functions using behavioral tests as well as nerve conduction measurements showed that 12 rats injected with whole IgG from a patient with anti-CNTN1 auto-antibodies did not develop any deficits. Furthermore, binding of human anti-CNTN1 auto-antibodies could not be detected in teased motor and sensory nerve roots.

To make sure that the injected auto-antibodies were able to reach the analyzed nerve roots, we injected EBD. However, spread of EBD solution into the lumbar spinal cord and lumbar nerves indicated that also the IgG solution should have been able to reach the lumbar nerve roots. Furthermore, other studies used this technique to successfully apply antibodies to the lumbar nerve roots, as well (Manso et al., 2019). This suggests that whole IgG from our CIDP patient with auto-antibodies against CNTN1 did not bind at the nerve roots and therefore did not cause any symptoms.

Previous studies testing the effect of anti-CNTN1 IgG4 auto-antibodies showed that they can be pathogenic and are able to access and specifically bind to the paranodal region (Doppler et al., 2019; Manso et al., 2016). *Manso et al.* however pre-sensitized their animals (n=20) with P2 peptide and injected purified IgG4 intravenously. *Doppler et al.* used the same patient IgG as used in this study but injected it intraneurally into the sciatic nerve of Lewis rats (n=20). Both groups reported nerve conduction impairment in a fraction of injected animals (40% in both studies). The other treated animals were not affected by the injected auto-antibodies. Still, it seems unlikely that our cohort size

(n=12) prevented us from detecting animals affected by the IgG. *Manso et al.* had two cohorts infused with anti-CNTN1 IgG4 auto-antibodies from two different patients. In one patient group, 70% of treated animals were affected, in the other group only 10%. This suggests that there is variability of binding capacity between patients with the same kind of auto-antibodies. However, our IgG has been already shown to be pathogenic. Still, since the intraneural injection is more focal and directly reaches the target nerve fibers, the IgG from this patient might not be target-specific enough. Another study investigating the pathogenicity of anti-NF155 IgG4 auto-antibodies injected purified IgG4 intrathecally without pre-immunization, similar to our protocol (Manso et al., 2019). They reported a severe motor phenotype with gait abnormalities and nerve conduction alterations. Since patients with anti-NF155 and anti-CNTN1 auto-antibodies show clinical distinct features (Vural et al., 2018), it is not surprising that their findings are not in accordance with ours.

It is also known that different IgG isotypes lead to different pathomechanisms. While IgG4 does not induce complement activation IgG3 - which is often found in the acute phase of the disease - does. *Doppler et al.* also investigated anti-CNTN1 IgG3 auto-antibodies which had a more severe effect than the IgG4 (Doppler et al., 2019).

Since in this study auto-antibody binding could not be detected, it is plausible that we did not detect any changes in behavioral or electrophysiological examinations. Although some single significant differences between the control and patient groups or changes within a group over time were observed, these findings are probably due to inconsistencies between rat cohorts or the time course of the experiments. For instance, the initial decline of rotarod performances in control animals (Fig. 4 A) might be explained by the additional stress on the animals by daily injections and behavioral testing. As the injections became less frequent the rotarod performance was restored. The same trend was observed in patient animals; however the changes were not significant. The increased sensitivity to mechanical stimuli in patient animals on day 3 might also be explained by the increased stress in the first week of injections.

Another reason for these variabilities might be the multiple cohorts of animals. Since patient animals tended to be more prone to complications due to infections or connective tissue formation in the spinal cord than control animals, the ratio of control to patient

animals remained rarely stable until the end of the experiments. This might also influence results of behavioral testing.

In summary, anti-CNTN1 auto-antibodies did not bind to the nerve roots *in vivo* when injected intrathecally over a 3-week period. Therefore, there were neither effects on motor and sensory functions nor on electrophysiological properties. In this study however, we only tested IgG from one CIDP patient. IgG4 or IgG3 auto-antibodies from other patients - also with auto-antibodies targeting other paranodal proteins - might actually bind and cause functional impairment *in vivo* through long-term intrathecal injection.

4.2 B lymphocyte study

Although treatment of auto-antibody associated CIDP with rituximab is often beneficial and well tolerated, it can also pose risks without ameliorating disease symptoms. Identification of auto-antibody producing B cell subsets in peripheral blood from seropositive patients might help to assess whether rituximab treatment will be promising as $CD20^-$ B cells are spared. Furthermore, more specific treatment options might be developed in the future. In order to identify auto-reactive B cell subsets, we aimed to establish a protocol in our laboratory to sort B cell subsets from peripheral blood and detect auto-antibody producing B cells using ELISpot.

The implementation of a protocol for PBMC isolation, MACS and FACS purification with subsequent detection of IgG and IgM secreting cells based on previous studies was successful (Crotty et al., 2004; Griffin et al., 2012; Hansen, 2011; Quách et al., 2016). Although we were able to detect auto-antibodies in supernatants of two CIDP patients by ELISA, the detection of antigen-specific auto-antibody producing B cells was not successful by the ELISpot assay. The number of patients and their material was limited which allowed us to make only a few attempts regarding the antigen-specific ELISpot assay. Since we did not have a reliable positive control for the ELISpot a statement about the suitability of the used protocol cannot be made. It is obvious that further testing is necessary to ensure proper detection of auto-antibodies by ELISpot.

The B cell subpopulation frequencies and the occurrence of antibody-secreting cells were similar to the frequencies reported in a previous study (Quách et al., 2016). In this study, isolated PBMC from freshly drawn unfrozen peripheral blood were used for analyses. Due to logistical reasons, we could not use freshly isolated PBMCs, but froze them until further processing which might explain differences. Furthermore, we only had a low number of samples for our analyses.

Concerning B cell subset frequencies and their occurrence of antibody-secreting cells, we could show that after stimulation for 72 h, frequencies of B cell subsets shifted and numbers of antibody-secreting cells were increased. While the frequencies of memory B cells and naive B cells were decreased, the frequency of $CD20^+CD38^{hi}$ cells increased and the frequencies of PBs and B1 cells remained the same. Further FACS analysis of 3-day stimulated sort-purified memory B cells revealed evidence that $CD20^+CD38^{hi}$ cells - which

are proposed to be pre-PBs (Quách et al., 2016) - might be derived from memory B cells, whereas unstimulated memory B cells tend to acquire a B1-like phenotype. As only one experiment of this kind was performed further analyses need to be performed to verify this observation.

Furthermore, we could show that detection of auto-antibodies in supernatants of PBMCs that were stimulated for 10 days was possible using ELISA, ensuring that there are in fact auto-reactive B cells in blood from patients. However, detection after 3 days of stimulation was not possible in the limited samples of patient supernatants that were available to us. Due to the low number of analyzed samples, we cannot exclude that detection is only possible after 10 days of stimulation. In a previous study, auto-antibodies were also detected after 10 days of stimulation in another disease (Thaler et al., 2019). Taken together, this suggests that for pre-screening PBMCs for auto-reactive B cells the 10-day stimulation might be more reliable.

Even though we could detect auto-antibodies in supernatants of PBMCs of seropositive CIDP patients after 10 days of stimulation, detection by ELISpot following MACS and FACS-purification of B cell subpopulations was not possible. Although sorted B cells secreted IgG, auto-antibodies were not detected. We cannot be sure that the protocol is suitable for NF155 and CNTN1 proteins since we lacked a suitable positive control and enough patient samples to elucidate possible problems. It can furthermore not be excluded that the sorted B cell subpopulations did not produce auto-antibodies or that auto-reactive B cells were to scarce.

In summary, we established a protocol for the purification of antibody-secreting B cell subpopulations in our laboratory. Furthermore, we showed that PBMC can also be processed after 3 and even 10 days after stimulation which then produce larger amounts of antibodies. Some subpopulations are increased in their numbers resulting in more antibody-secreting cells while some subpopulations show a higher frequency of antibody producing cells while their numbers do not increase. We were not able to detect auto-antibody producing B cell subsets. However, we succeeded to detect auto-antibodies in supernatants by ELISA, which presents a method for pre-screening for future experiments concerning auto-antibodies in CIDP patients.

4.3 CMT1A study: Identification of possible biomarkers for assessment of disease severity

In CMT1A, biomarkers that assess the actual nerve damage are not yet established and used in clinical trials. Skin punch biopsies have been shown to be a useful tool to detect nerve damage in different neuropathies. Several studies have shown that in CMT1A cutaneous innervation is disturbed. However, these studies either investigated only single parameters or small cohorts. Our goal was to find objective and reproducible outcome measures that assess the nerve damage for future clinical trials testing CMT1A medication.

To find a possible biomarker we analyzed a series of parameters in 3-mm skin punch biopsies from the lateral index finger from a large cohort of 48 CMT1A patients. In our study, the IENFD, the Merkel cell and Meissner corpuscle densities have been identified as possible outcome criteria in CMT1A. We revealed a loss of small and large nerve fibers. Further, we could show that the disease severity which was evaluated with the CMTNSv2 correlated with small nerve fiber density.

Compared to healthy controls, the IENFD was decreased in our CMT1A cohort. This loss of small epidermal nerve fibers in CMT1A has been previously described in other studies, where biopsies from the fingertip, the thigh and the distal leg in 20 CMT1A patients (Nolano et al., 2015) and 75 biopsies from the distal leg were investigated (Duchesne et al., 2018). In these two studies, IENFD correlated negatively with age and not with the disease severity. In our CMT1A cohort, the IENFD did not correlate with age. However, it did correlate inversely with age in our control cohort. With regard to small nerve fiber involvement in the demyelinating CMT1A disease, it has been previously debated that the overexpression of PMP22 not only occurs in myelinating Schwann cells but also in the plasma membranes of nonmyelinating Schwann cells. This was suggested to lead to axon-Schwann cell interaction disturbances in myelinated Schwann cells, but nerve degeneration might also be caused in Remak bundles (Duchesne et al., 2018; Nolano et al., 2015). Our results indicate that in glabrous skin from the finger IENFD declines with increasing disease severity.

Previous studies have reported that the density of dermal nerve bundles is a measure to

evaluate nerve damage (Doppler et al., 2012; Li et al., 2005). For this study though, the bundle densities did not proof useful as they were dependent from the analyzed dermis area. This shows that it is very important to evaluate bundle densities in sections of comparable sizes. For this study, the dermal nerve bundle densities are no suitable measure and also might not be in future studies, if uniform section size cannot be guaranteed.
Nevertheless, large myelinated fibers can also be investigated by analyzing mechanoreceptors in which myelinated nerve fibers are involved. We chose the Meissner corpuscles and Merkel cells which both are located near the epidermal-dermal junction.
The density of Meissner corpuscles tended to be reduced in CMT1A patients compared to healthy controls. Furthermore, in the CMT1A group Meissner corpuscle density correlated negatively with age which was not shown in the control group. This might indicate that Meissner corpuscle deterioration is accelerated in CMT1A patients compared to controls. Other studies have also proposed the Meissner corpuscle density as a possible outcome measure for therapeutic trials (Almodovar et al., 2011; Manganelli et al., 2015; Saporta et al., 2009). However, in other studies cohort sizes were small and different techniques were used to investigate different sites of the hand (Almodovar et al., 2011; Manganelli et al., 2015; Nolano et al., 2015; Saporta et al., 2009). Furthermore, correlation analyses revealed differing results and were not in consistency with our correlation results. The inconsistency with our results might be due to our units. We decided to define the density per papilla instead of per area, since we observe that the papillae in our sections varied in size. Our data indicate that Meissner corpuscle decline is accelerated in CMT1A patients in comparison to healthy controls. Controls show a less pronounced relationship between age and Meissner corpuscle deterioration than in CMT1A patients. Therefore, the Meissner corpuscle density might be a helpful additional parameter to evaluate nerve damage in CMT1A.
The Merkel cell density was previously described in a P0-deficient mouse model (Frei et al., 1999). To our knowledge however, this measure has not yet been used to investigate human skin innervation. In accordance with our Meissner corpuscle findings, Merkel cell density was reduced in CMT1A patients compared to healthy controls. Since we observed that singled out Merkel cells, that were not clustered with other Merkel cells, tended to be denervated, we determined the fraction of denervated Merkel cells as well. In CMT1A

patients the fraction of denervated Merkel cells was highly elevated compared to healthy controls. This indicated that the degeneration of myelinated nerve fibers and therefore Merkel cells is promoted by CMT1A disease. These findings lead to the conclusion that the density and the fraction of denervated Merkel cells might be a useful biomarker in CMT1A.

Next, we more closely investigated the architecture of nodes of Ranvier to assess myelinated fibers in the dermis. The fiber calibers were comparable between the four groups. Still, the CMT1A group showed shortened nodes and paranodes. Previous studies have also observed shortened paranodes in *Trembler-J* mice - used as a model for CMT1A - (Devaux et al., 2005) and in CMT1A patients (Saporta et al., 2009). *Saporta et al.* however, also described higher asymmetry indeces compared to healthy control, which we could not confirm. Possible reasons for this discordance could be the different analyses between the studies. In our study, we randomly chose five nodes per sample. In contrast, *Saporta et al.* measured each node they could find. Potentially, more symmetric nodes than asymmetric were measured for our evaluation. As paranodal parameters only show weak effects in relation to disease severity in our study, and the acquisition is very time-consuming, we reasoned that these measures are too impractical for future studies.

In a previous study, Langerhans cells were reported to be reduced in CMT1A patients compared to healthy controls (Duchesne et al., 2018). In our cohort though, no differences were detected in comparison to healthy controls. We analyzed glabrous skin, but the reduction of Langerhans cells was found in biopsies from the distal leg, which might be the reason for these differing results. The validity of our findings is supported by the fact that in our CIDP group - an inflammatory disease - Langerhans cell density was elevated. When glabrous skin biopsies are used, such as in or study, the Langerhans cell density is not a useful measure to evaluate disease severity.

In the baseline examination of the study, we were looking for measures that evaluate the disease severity and therefore might be candidates as biomarkers that also assess disease progression. In summary of the baseline results, we identified the IENFD, Merkel cell density and Meissner corpuscle density as parameters that might be valuable for the assessment of disease severity. The nodal and paranodal parameters and the Langerhans cell density might be further investigated as there were no difficulties in their acquisition.

Although dermal nerve bundle densities have been shown to be useful in other studies, in our study this measure was not suitable due to the varying sample sizes. A graphical summary of the baseline results, which compares skin from healthy controls and CMT1A patients is shown in Fig. 36.

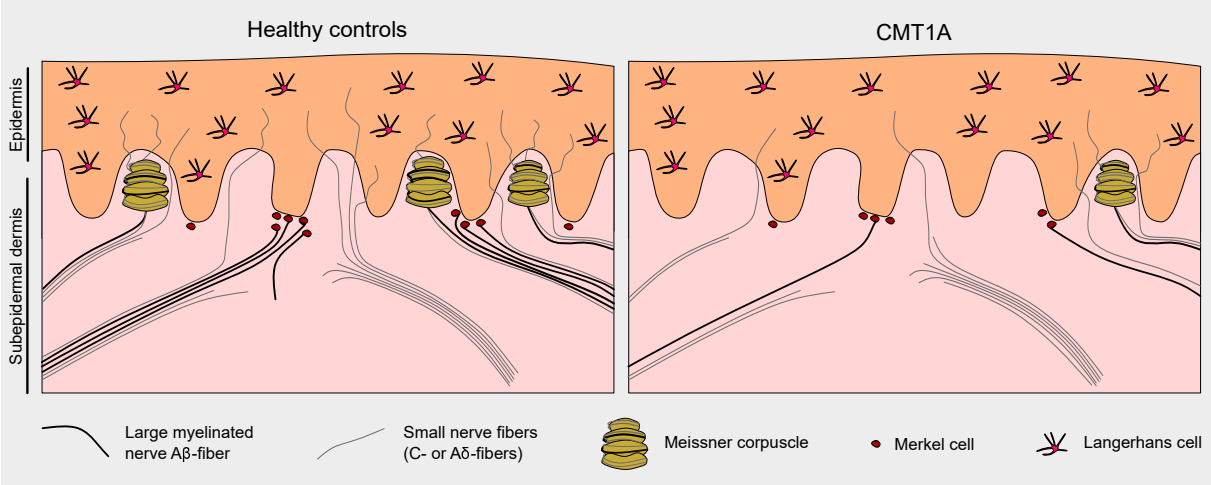

Figure 36: Comparison of cutaneous nerve structures and their occurrence in glabrous skin from healthy controls and CMT1A patients. This figure has been previously published in *Hartmannsberger et al. (2020)*.

The suitability as outcome measure still needed to be confirmed. In order to evaluate the identified possible parameters (IENFD, Meissner corpuscle and Merkel cell densities), follow-up biopsies were collected two years after baseline collection. However, we were not able not draw any conclusions about the suitability of the measures since only six follow-up biopsies were obtained.

Although the IENFD tended to decrease over time and this change showed a trend to correlate with the change of the CMTNSv2, these analyses showed no statistical significance. Surprisingly, the Merkel cell and Meissner corpuscle densities showed a trend to increase over time, while the fraction of denervated Merkel cells tended to decrease which is consistent with the elevated Merkel cell density.

A possible explanation for these unexpected results might be the overall very scarce distribution of these mechanoreceptors throughout the lateral index finger. Only small deviations from the original biopsy site might cause deviation in the receptor distribution as well. Another factor to consider is the fact that since we investigated less parameters in the follow-up analysis, we had more tissue for each evaluated parameter. However,

the baseline analyses revealed that this should not be the case. Since we only received six biopsies a clear statement about the suitability of the mechanoreceptors as potential outcome measures cannot be given.

The low number of follow-up biopsies is by far the biggest limitation of the study. This prevents us from concluding if there is a parameter among our candidates that evaluates not only disease severity but also disease progression. For the baseline analysis, one of the limitations is the low number of patients between the ages 20-30 years which might introduce a bias. Another limitation might be the chosen biopsy site to minimize the patients' discomfort. The innervation at the lateral part is not as dense as at the fingertip. However, evaluation of innervation was still possible.

In summary, we identified the IENFD, Merkel cell density, fraction of denervated Merkel cells and the Meissner corpuscle density as measures that might be useful for the evaluation of the disease severity. However, given the small sample size, we could not assess whether one of these parameters might be valuable as an indicator for disease progression.

5 References

Abraira, V. E., & Ginty, D. D. (2013). The sensory neurons of touch. *Neuron*, *79*(4), 618–639.

Airaksinen, M. S., Koltzenburg, M., Lewin, G. R., Masu, Y., Helbig, C., Wolf, E., Brem, G., Toyka, K. V., Thoenen, H., & Meyer, M. (1996). Specific subtypes of cutaneous mechanoreceptors require neurotrophin-3 following peripheral target innervation. *Neuron*, *16*(2), 287–295.

Almodovar, J. L., Ferguson, M., McDermott, M. P., Lewis, R. A., Shy, M. E., & Herrmann, D. N. (2011). In vivo confocal microscopy of Meissner corpuscles as a novel sensory measure in CMT1A. *Journal of the Peripheral Nervous System*, *16*(3), 169–174.

Attarian, S., Vallat, J. M., Magy, L., Funalot, B., Gonnaud, P. M., Lacour, A., Péréon, Y., Dubourg, O., Pouget, J., Micallef, J., Franques, J., Lefebvre, M. N., Ghorab, K., Al-Moussawi, M., Tiffreau, V., Preudhomme, M., Magot, A., Leclair-Visonneau, L., Stojkovic, T., ... Cohen, D. (2014). An exploratory randomised double-blind and placebo-controlled phase 2 study of a combination of baclofen, naltrexone and sorbitol (PXT3003) in patients with Charcot-Marie-Tooth disease type 1A. *Orphanet Journal of Rare Diseases*, *9*(1).

Baumgarth, N. (2011). The double life of a B-1 cell: Self-reactivity selects for protective effector functions. *Nature Reviews Immunology*, *11*(1), 34–46.

Berghen, N., Vulsteke, J. B., Westhovens, R., Lenaerts, J., & De Langhe, E. (2019). Rituximab in systemic autoimmune rheumatic diseases: indications and practical use. *Acta Clinica Belgica: International Journal of Clinical and Laboratory Medicine*, *74*(4), 272–279.

Berghs, S., Aggujaro, D., Dirkx, R., Maksimova, E., Stabach, P., Hermel, J. M., Zhang, J. P., Philbrick, W., Slepnev, V., Ort, T., & Solimena, M. (2000). βIV spectrin, a new spectrin localized at axon initial segments and nodes of ranvier in the central and peripheral nervous system. *Journal of Cell Biology*, *151*(5), 985–1001.

Bhat, M. A., Rios, J. C., Lu, Y., Garcia-Fresco, G. P., Ching, W., Martin, M. S., Li, J., Einheber, S., Chesler, M., Rosenbluth, J., Salzer, J. L., & Bellen, H. J. (2001). Axon-glia interactions and the domain organization of myelinated axons requires Neurexin IV/Caspr/Paranodin. *Neuron*, *30*(2), 369–383.

Boulais, N., & Misery, L. (2007). Merkel Cells. *Journal of American Academic Dermatology*, *57*(1), 33–38.

Boyle, M. E., Berglund, E. O., Murai, K. K., Weber, L., Peles, E., & Ranscht, B. (2001). Contactin orchestrates assembly of the septate-like junctions at the paranode in myelinated peripheral nerve. *Neuron*, *30*(2), 385–397.

Broers, M. C., Bunschoten, C., Nieboer, D., Lingsma, H. F., & Jacobs, B. C. (2019). Incidence and Prevalence of Chronic Inflammatory Demyelinating Polyradiculoneu-

ropathy: A Systematic Review and Meta-Analysis. *Neuroepidemiology*, *52*(3-4), 161–172.

Cassese, G., Arce, S., Hauser, A. E., Lehnert, K., Moewes, B., Mostarac, M., Muehlinghaus, G., Szyska, M., Radbruch, A., & Manz, R. A. (2003). Plasma Cell Survival Is Mediated by Synergistic Effects of Cytokines and Adhesion-Dependent Signals. *The Journal of Immunology*, *171*(4), 1684–1690.

Chaplan, S. R., Bach, F. W., Pogrel, J. W., Chung, J. M., & Yaksh, T. L. (1994). Quantitative assessment of tactile allodynia in the rat paw. *Journal of Neuroscience Methods*, *53*(1), 55–63.

Charles, P., Tait, S., Faivre-Sarrailh, C., Barbin, G., Gunn-Moore, F., Denisenko-Nehrbass, N., Guennoc, A. M., Girault, J. A., Brophy, P. J., & Lubetzki, C. (2002). Neurofascin is a glial receptor for the paranodin/Caspr-contactin axonal complex at the axoglial junction. *Current Biology*, *12*(3), 217–220.

Collongues, N., Samama, B., Schmidt-Mutter, C., Chamard-Witkowski, L., Debouverie, M., Chanson, J. B., Antal, M. C., Benardais, K., Jérôme, D. S., Velten, M., & Boehm, N. (2018). Quantitative and qualitative normative dataset for intraepidermal nerve fibers using skin biopsy. *PLoS ONE*, *13*(1), e0191614.

Cornett, K. M., Wojciechowski, E., Sman, A. D., Walker, T., Menezes, M. P., Bray, P., Halaki, M., Burns, J., Sman, D., Cornett, K. M., Wojciechowski, E., Menezes, M. P., Mandarakas, M. R., Rose, K. J., Bray, P., Baldwin, J., McKay, M. J., Refshauge, K. M., Raymond, J., … Sman, A. (2019). Magnetic resonance imaging of the anterior compartment of the lower leg is a biomarker for weakness, disability, and impaired gait in childhood Charcot–Marie–Tooth disease. *Muscle and Nerve*, *59*(2), 213–217.

Covens, K., Verbinnen, B., Geukens, N., Meyts, I., Schuit, F., Van Lommel, L., Jacquemin, M., & Bossuyt, X. (2013). Characterization of proposed human B-1 cells reveals pre-plasmablast phenotype. *Blood*, *121*(6), 5176–5183.

Crotty, S., Aubert, R. D., Glidewell, J., & Ahmed, R. (2004). Tracking human antigen-specific memory B cells: A sensitive and generalized ELISPOT system. *Journal of Immunological Methods*, *286*(1-2), 111–122.

Dalakas, M. C. (2011). Advances in the diagnosis, pathogenesis and treatment of CIDP. *Nature Reviews Neurology*, *7*(9), 507–517.

Damato, V., Evoli, A., & Iorio, R. (2016). Efficacy and safety of rituximab therapy in neuromyelitis optica spectrum disorders: A systematic review and meta-analysis. *JAMA Neurology*, *73*(11), 1342–1348.

Davis, J. Q., Lambert, S., & Bennett, V. (1996). Molecular composition of the node of Ranvier: Identification of ankyrin- binding cell adhesion molecules neurofascin (mucin+/third FNIII domain-) and NrCAM at nodal axon segments. *Journal of Cell Biology*, *135*(5), 1355–1367.

Devaux, J. J., & Scherer, S. S. (2005). Altered ion channels in an animal model of Charcot-Marie-Tooth disease type IA. *Journal of Neuroscience*, *25*(6), 1470–1480.

Doppler, K., Werner, C., Henneges, C., & Sommer, C. (2012). Analysis of myelinated fibers in human skin biopsies of patients with neuropathies. *Journal of Neurology*, *259*(9), 1879–1887.

Doppler, K., Schuster, Y., Appeltshauser, L., Biko, L., Villmann, C., Weishaupt, A., Werner, C., & Sommer, C. (2019). Anti-CNTN1 IgG3 induces acute conduction block and motor deficits in a passive transfer rat model. *Journal of Neuroinflammation*, *16*(1), 1–13.

Doppler, K., Appeltshauser, L., Villmann, C., Martin, C., Peles, E., Krämer, H. H., Haarmann, A., Buttmann, M., & Sommer, C. (2016). Auto-antibodies to contactin-associated protein 1 (Caspr) in two patients with painful inflammatory neuropathy. *Brain*, *139*(10), 2617–2630.

Doppler, K., Appeltshauser, L., Wilhelmi, K., Villmann, C., Dib-Hajj, S. D., Waxman, S. G., Mäurer, M., Weishaupt, A., & Sommer, C. (2015). Destruction of paranodal architecture in inflammatory neuropathy with anti-contactin-1 autoantibodies. *Journal of Neurology, Neurosurgery and Psychiatry*, *86*(7), 720–728.

Doppler, K., Werner, C., & Sommer, C. (2013). Disruption of nodal architecture in skin biopsies of patients with demyelinating neuropathies. *Journal of the Peripheral Nervous System*, *18*(2), 168–176.

Doppler, K., Stengel, H., Appeltshauser, L., Grosskreutz, J., King Man Ng, J., Meinl, E., & Sommer, C. (2018). Neurofascin-155 IgM autoantibodies in patients with inflammatory neuropathies. *Journal of neurology, neurosurgery, and psychiatry*, *89*(11), 1145–1151.

Duchesne, M., Danigo, A., Richard, L., Vallat, J. M., Attarian, S., Gonnaud, P. M., Lacour, A., Péréon, Y., Stojkovic, T., Nave, K. A., Bertrand, V., Nabirotchkin, S., Cohen, D., Demiot, C., & Magy, L. (2018). Skin biopsy findings in patients with CMT1A: Baseline data from the CLN-PXT3003-01 study provide new insights into the pathophysiology of the disorder. *Journal of Neuropathology and Experimental Neurology*, *77*(4), 274–281.

Feinberg, K., Eshed-Eisenbach, Y., Frechter, S., Amor, V., Salomon, D., Sabanay, H., Dupree, J. L., Grumet, M., Brophy, P. J., Shrager, P., & Peles, E. (2010). A Glial Signal Consisting of Gliomedin and NrCAM Clusters Axonal Na+ Channels during the Formation of Nodes of Ranvier. *Neuron*, *65*(4), 490–502.

Fledrich, R., Schlotter-Weigel, B., Schnizer, T. J., Wichert, S. P., Stassart, R. M., Meyer Zu Hörste, G., Klink, A., Weiss, B. G., Haag, U., Walter, M. C., Rautenstrauss, B., Paulus, W., Rossner, M. J., & Sereda, M. W. (2012a). A rat model of Charcot-Marie-Tooth disease 1A recapitulates disease variability and supplies biomarkers of axonal loss in patients. *Brain*, *135*(1), 72–87.

Fledrich, R., Mannil, M., Leha, A., Ehbrecht, C., Solari, A., Pelayo-Negro, A. L., Berciano, J., Schlotter-Weigel, B., Schnizer, T. J., Prukop, T., Garcia-Angarita, N., Czesnik, D., Haberlová, J., Mazanec, R., Paulus, W., Beissbarth, T., Walter, M. C., Hogrel, J. Y., Dubourg, O., ... Sereda, M. W. (2017). Biomarkers predict outcome in Charcot-Marie-Tooth disease 1A. *Journal of Neurology, Neurosurgery and Psychiatry*, *88*(11), 941–952.

Fledrich, R., Stassart, R. M., & Sereda, M. W. (2012b). Murine therapeutic models for Charcot-Marie-Tooth (CMT) disease. *British Medical Bulletin*, *102*(1), 89–113.

Fledrich, R., Stassart, R. M., Klink, A., Rasch, L. M., Prukop, T., Haag, L., Czesnik, D., Kungl, T., Abdelaal, T. A., Keric, N., Stadelmann, C., Brück, W., Nave, K. A., & Sereda, M. W. (2014). Soluble neuregulin-1 modulates disease pathogenesis in rodent models of Charcot-Marie-Tooth disease 1A. *Nature Medicine*, *20*(9), 1055–1061.

Franks, S. E., Getahun, A., Hogarth, P. M., & Cambier, J. C. (2016). Targeting B cells in treatment of autoimmunity. *Current Opinion in Immunology*, *43*, 39–45.

Frei, R., Mötzing, S., Kinkelin, I., Schachner, M., Koltzenburg, M., & Martini, R. (1999). Loss of Distal Axons and Sensory Merkel Cells and Features Indicative of Muscle Denervation in Hindlimbs of P0-Deficient Mice. *The Journal of Neuroscience*, *19*(14), 6058–6067.

Gess, B., Baets, J., De Jonghe, P., Reilly, M. M., Pareyson, D., & Young, P. (2015). Ascorbic acid for the treatment of Charcot-Marie-Tooth disease. *Cochrane Database of Systematic Reviews*, (12), CD011952.

Gess, B., Schirmacher, A., Boentert, M., & Young, P. (2013). Charcot-Marie-Tooth disease: Frequency of genetic subtypes in a German neuromuscular center population. *Neuromuscular Disorders*, *23*(8), 647–651.

Graham, R. C., & Hughes, R. A. (2006). A modified peripheral neuropathy scale: The Overall Neuropathy Limitations Scale. *Journal of Neurology, Neurosurgery and Psychiatry*, *77*(8), 973–976.

Griffin, D. O., & Rothstein, T. L. (2012). Human B1 cell frequency: Isolation and analysis of human B1 cells. *Frontiers in Immunology*, *3*(MAY).

Griffin, D. O., Holodick, N. E., & Rothstein, T. L. (2011). Human B1 cells in umbilical cord and adult peripheral blood express the novel phenotype CD20+CD27+CD43+CD70-. *Journal of Experimental Medicine*, *208*(1), 67–80.

Hansen, R. S. (2011). SOP: Isolation of CD20-positive cells from human leukapheresis product. *UW Encode Project*, http://www.uwencode.org/protocols.

Hartmannsberger, B., Doppler, K., Stauber, J., Schlotter-Weigel, B., Young, P., Sereda, M. W., & Sommer, C. (2020). Intraepidermal nerve fiber density as biomarker in Charcot-Marie-Tooth disease 1A. *Brain Communications*, *2*(1), fcaa012.

Höfer, T., Muehlinghaus, G., Moser, K., Yoshida, T., Mei, H. E., Hebel, K., Hauser, A., Hoyer, B., Luger, E. O., Dörner, T., Manz, R. A., Hiepe, F., & Radbruch, A. (2006). Adaptation of humoral memory. *Immunological Reviews*, *211*, 295–302.

Horresh, I., Bar, V., Kissil, J. L., & Peles, E. (2010). Organization of myelinated axons by Caspr and Caspr2 requires the cytoskeletal adapter protein 4.1B. *Journal of Neuroscience*, *30*(7), 2480–2489.

Huxley, C., Passage, E., Manson, A., Putzu, G., Figarella-Branger, D., Pellissier, J. F., & Fontés, M. (1996). Construction of a mouse model of Charcot-Marie-Tooth disease type 1A by pronuclear injection of human YAC DNA. *Human Molecular Genetics*, *5*(5), 563–569.

Huxley, C., Passage, E., Robertson, A. M., Youl, B., Huston, S., Manson, A., Sabéran-Djoniedi, D., Figarella-Branger, D., Pellissier, J. F., Thomas, P. K., & Fontés, M. (1998). Correlation between varying levels of PMP22 expression and the degree of demyelination and reduction in nerve conduction velocity in transgenic mice. *Human Molecular Genetics*, *7*(3), 449–458.

Inui, M., Hirota, S., Hirano, K., Fujii, H., Sugahara-Tobinai, A., Ishii, T., Harigae, H., & Takai, T. (2015). Human CD43+ B cells are closely related not only to memory B cells phenotypically but also to plasmablasts developmentally in healthy individuals. *International Immunology*, *27*(7), 345–355.

Jahnmatz, M., Kesa, G., Netterlid, E., Buisman, A. M., Thorstensson, R., & Ahlborg, N. (2013). Optimization of a human IgG B-cell ELISpot assay for the analysis of vaccine-induced B-cell responses. *Journal of Immunological Methods*, *391*(1-2), 50–59.

Kasi, P. M., Tawbi, H. A., Oddis, C. V., & Kulkarni, H. S. (2012). Clinical review: Serious adverse events associated with the use of rituximab - a critical care perspective. *Critical Care*, *16*(4), 231.

Katona, I., Wu, X., Feely, S. M. E., Sottile, S., Siskind, C. E., Miller, L. J., Shy, M. E., & Li, J. (2009). PMP22 expression in dermal nerve myelin from patients with CMT1A. *Brain*, *132*(7), 1734–1740.

Kawamura, N., Yamasaki, R., Yonekawa, T., Matsushita, T., Kusunoki, S., Nagayama, S., Fukuda, Y., Ogata, H., Matsuse, D., Murai, H., & Kira, J. I. (2013). Anti-neurofascin antibody in patients with combined central and peripheral demyelination. *Neurology*, *81*(8), 714–722.

Khalil, M., Teunissen, C. E., Otto, M., Piehl, F., Sormani, M. P., Gattringer, T., Barro, C., Kappos, L., Comabella, M., Fazekas, F., Petzold, A., Blennow, K., Zetterberg, H., & Kuhle, J. (2018). Neurofilaments as biomarkers in neurological disorders. *Nature Reviews Neurology*, *14*(10), 577–589.

Klein, U., Rajewsky, K., & Küppers, R. (1998). Human immunoglobulin (Ig)M+IgD+ peripheral blood B cells expressing the CD27 cell surface antigen carry somatically

mutated variable region genes: CD27 as a general marker for somatically mutated (memory) B cells. *Journal of Experimental Medicine*, *188*(9), 1679–1689.

Koike, H., Kadoya, M., Kaida, K. I., Ikeda, S., Kawagashira, Y., Iijima, M., Kato, D., Ogata, H., Yamasaki, R., Matsukawa, N., Kira, J. I., Katsuno, M., & Sobue, G. (2017). Paranodal dissection in chronic inflammatory demyelinating polyneuropathy with anti-neurofascin-155 and anti-contactin-1 antibodies. *Journal of Neurology, Neurosurgery and Psychiatry*, *88*(6), 465–473.

Labasque, M., Hivert, B., Nogales-Gadea, G., Querol, L., Illa, I., & Faivre-Sarrailh, C. (2014). Specific contactin N-glycans are implicated in neurofascin binding and autoimmune targeting in peripheral neuropathies. *Journal of Biological Chemistry*, *289*(11), 7907–7918.

Lauria, G., Cornblath, D. R., Johansson, O., McArthur, J. C., Mellgren, S. I., Nolano, M., Rosenberg, N., & Sommer, C. (2005). EFNS guidelines on the use of skin biopsy in the diagnosis of peripheral neuropathy. *European Journal of Neurology*, *12*(10), 747–758.

Lauria, G., Lombardi, R., Camozzi, F., & Devigili, G. (2009). Skin biopsy for the diagnosis of peripheral neuropathy. *Histopathology*, *54*(3), 273–285.

Lee, S., Bazick, H., Chittoor-Vinod, V., Al Salihi, M. O., Xia, G., & Notterpek, L. (2018). Elevated Peripheral Myelin Protein 22, Reduced Mitotic Potential, and Proteasome Impairment in Dermal Fibroblasts from Charcot-Marie-Tooth Disease Type 1A Patients. *American Journal of Pathology*, *188*(3), 728–738.

Lee, W. J., Lee, S. T., Byun, J. I., Sunwoo, J. S., Kim, T. J., Lim, J. A., Moon, J., Lee, H. S., Shin, Y. W., Lee, K. J., Kim, S., Jung, K. H., Jung, K. Y., Chu, K., & Lee, S. K. (2016). Rituximab treatment for autoimmune limbic encephalitis in an institutional cohort. *Neurology*, *86*(18), 1683–1691.

Lewis, R. A., McDermott, M. P., Herrmann, D. N., Hoke, A., Clawson, L. L., Siskind, C., Feely, S. M., Miller, L. J., Barohn, R. J., Smith, P., Luebbe, E., Wu, X., & Shy, M. E. (2013). High-dosage ascorbic acid treatment in charcot-marie-tooth disease type 1A results of a randomized, double-masked, controlled trial. *JAMA Neurology*, *70*(8), 981–987.

Li, J., Bai, Y., Ghandour, K., Qin, P., Grandis, M., Trostinskaia, A., Ianakova, E., Wu, X., Schenone, A., Vallat, J. M., Kupsky, W. J., Hatfield, J., & Shy, M. E. (2005). Skin biopsies in myelin-related neuropathies: Bringing molecular pathology to the bedside. *Brain*, *128*(5), 1168–1177.

Li, W., Batliwalla, F., & Rothstein, T. L. (2013). Human B-1 cells are not preplasmablasts: Analysis of microarray data and other issues. *Blood*, *122*(22), 3691–3693.

Lindholm, C., Börjesson-Asp, K., Zendjanchi, K., Sundqvist, A.-C., Tarkowski, A., & Bokarewa, M. (2008). Longterm clinical and immunological effects of anti-CD20

treatment in patients with refractory systemic lupus erythematosus. *The Journal of rheumatology*, *35*(5), 826–33.

Malkmus, S. A., & Yaksh, T. L. (2004). Intrathecal Catheterization and Drug Delivery in the Rat. *Methods in Molecular Medicine*, *99*, 109–121.

Manganelli, F., Tozza, S., Pisciotta, C., Bellone, E., Iodice, R., Nolano, M., Geroldi, A., Capponi, S., Mandich, P., & Santoro, L. (2014). Charcot-Marie-Tooth disease: Frequency of genetic subtypes in a Southern Italy population. *Journal of the Peripheral Nervous System*, *19*(4), 292–298.

Manganelli, F., Nolano, M., Pisciotta, C., Provitera, V., Fabrizi, G. M., Cavallaro, T., Stancanelli, A., Caporaso, G., Shy, M. E., & Santoro, L. (2015). Charcot-Marie-Tooth disease: New insights from skin biopsy. *Neurology*, *85*(14), 1202–1208.

Mannil, M., Solari, A., Leha, A., Pelayo-Negro, A. L., Berciano, J., Schlotter-Weigel, B., Walter, M. C., Rautenstrauss, B., Schnizer, T. J., Schenone, A., Seeman, P., Kadian, C., Schreiber, O., Angarita, N. G., Fabrizi, G. M., Gemignani, F., Padua, L., Santoro, L., Quattrone, A., … Sereda, M. W. (2014). Selected items from the Charcot-Marie-Tooth (CMT) Neuropathy Score and secondary clinical outcome measures serve as sensitive clinical markers of disease severity in CMT1A patients. *Neuromuscular Disorders*, *24*(11), 1003–1017.

Manso, C., Querol, L., Lleixà, C., Poncelet, M., Mekaouche, M., Vallat, J. M., Illa, I., & Devaux, J. J. (2019). Anti–neurofascin-155 IgG4 antibodies prevent paranodal complex formation in vivo. *Journal of Clinical Investigation*, *129*(6), 2222–2236.

Manso, C., Querol, L., Mekaouche, M., Illa, I., & Devaux, J. J. (2016). Contactin-1 IgG4 antibodies cause paranode dismantling and conduction defects. *Brain*, *139*(6), 1700–1712.

Mathey, E. K., Park, S. B., Hughes, R. A., Pollard, J. D., Armati, P. J., Barnett, M. H., Taylor, B. V., Dyck, P. J. B., Kiernan, M. C., & Lin, C. S. (2015). Chronic inflammatory demyelinating polyradiculoneuropathy: From pathology to phenotype. *Journal of Neurology, Neurosurgery and Psychiatry*, *86*(9), 973–985.

Micallef, J., Attarian, S., Dubourg, O., Gonnaud, P. M., Hogrel, J. Y., Stojkovic, T., Bernard, R., Jouve, E., Pitel, S., Vacherot, F., Remec, J. F., Jomir, L., Azabou, E., Al-Moussawi, M., Lefebvre, M. N., Attolini, L., Yaici, S., Tanesse, D., Fontes, M., … Blin, O. (2009). Effect of ascorbic acid in patients with Charcot-Marie-Tooth disease type 1A: a multicentre, randomised, double-blind, placebo-controlled trial. *The Lancet Neurology*, *8*(12), 1103–1110.

Morrow, J. M., Sinclair, C. D., Fischmann, A., Machado, P. M., Reilly, M. M., Yousry, T. A., Thornton, J. S., & Hanna, M. G. (2016). MRI biomarker assessment of neuromuscular disease progression: A prospective observational cohort study. *The Lancet Neurology*, *15*(1), 65–77.

Moura, R. A., Quaresma, C., Vieira, A. R., Gonçalves, M. J., Polido-Pereira, J., Romão, V. C., Martins, N., Canhão, H., & Fonseca, J. E. (2017). B-cell phenotype and IgD-CD27- memory B cells are affected by TNF-inhibitors and tocilizumab treatment in rheumatoid arthritis. *PLoS ONE*, *12*(9), e0182927.

Murphy, S. M., Herrmann, D. N., McDermott, M. P., Scherer, S. S., Shy, M. E., Reilly, M. M., & Pareyson, D. (2011). Reliability of the CMT neuropathy score (second version) in Charcot-Marie-Tooth disease. *Journal of the Peripheral Nervous System*, *16*(3), 191–198.

Mygland, A., & Monstad, P. (2001). Chronic polyneuropathies in Vest-Agder, Norway. *European Journal of Neurology*, *8*(2), 157–165.

Nemazee, D. (2017). Mechanisms of central tolerance for B cells. *Nature Reviews Immunology*, *17*(5), 281–294.

Ng, J. K. M., Malotka, J., Kawakami, N., Derfuss, T., Khademi, M., Olsson, T., Linington, C., Odaka, M., Tackenberg, B., Prüss, H., Schwab, J. M., Harms, L., Harms, H., Sommer, C., Rasband, M. N., Eshed-Eisenbach, Y., Peles, E., Hohlfeld, R., Yuki, N., ... Meinl, E. (2012). Neurofascin as a target for autoantibodies in peripheral neuropathies. *Neurology*, *79*(23), 2241–2248.

Nobbio, L., Visigalli, D., Radice, D., Fiorina, E., Solari, A., Lauria, G., Reilly, M. M., Santoro, L., Schenone, A., & Pareyson, D. (2014). PMP22 messenger RNA levels in skin biopsies: Testing the effectiveness of a Charcot-Marie-Tooth 1A biomarker. *Brain*, *137*(6), 1614–1620.

Nolano, M., Provitera, V., Crisci, C., Stancanelli, A., Wendelschafer-Crabb, G., Kennedy, W. R., & Santoro, L. (2003). Quantification of myelinated endings and mechanoreceptors in human digital skin. *Annals of Neurology*, *54*(2), 197–205.

Nolano, M., Manganelli, F., Provitera, V., Pisciotta, C., Stancanelli, A., Caporaso, G., Iodice, R., Shy, M. E., & Santoro, L. (2015). Small nerve fiber involvement in CMT1A. *Neurology*, *84*(4), 407–414.

Ogata, H., Yamasaki, R., Hiwatashi, A., Oka, N., Kawamura, N., Matsuse, D., Kuwahara, M., Suzuki, H., Kusunoki, S., Fujimoto, Y., Ikezoe, K., Kishida, H., Tanaka, F., Matsushita, T., Murai, H., & Kira, J. I. (2015). Characterization of IgG4 anti-neurofascin 155 antibody-positive polyneuropathy. *Annals of Clinical and Translational Neurology*, *2*(10), 960–971.

Pan, Z., Kao, T., Horvath, Z., Lemos, J., Sul, J. Y., Cranstoun, S. D., Bennett, V., Scherer, S. S., & Cooper, E. C. (2006). A common ankyrin-G-based mechanism retains KCNQ and Na V channels at electrically active domains of the axon. *Journal of Neuroscience*, *26*(10), 2599–2613.

Pareyson, D., Reilly, M. M., Schenone, A., Fabrizi, G. M., Cavallaro, T., Manganelli, L., Vita, G., Quattrone, A., Padua, L., Gemignani, F., Visioli, F., Laurà, M., Radice, D., Calabrese, D., Hughes, R. A., Solari, A., Salsano, C., Nanetti, L., Marelli,

C., ... Sereda, M. (2011). Ascorbic acid in charcot-marie-tooth disease type 1A (CMTTRIAAL and CMT-TRAUK): A double-blind randomised trial. *The Lancet Neurology*, *10*(4), 320–328.

Pareyson, D., Scaioli, V., & Laurà, M. (2006). Clinical and electrophysiological aspects of charcot-marie-tooth disease. [Review]. *NeuroMolecular Medicine*, *8*(1-2), 3–22.

Passage, E., Norreel, J. C., Noack-Fraissignes, P., Sanguedolce, V., Pizant, J., Thirion, X., Robaglia-Schlupp, A., Pellissier, J. F., & Fontés, M. (2004). Ascorbic acid treatment corrects the phenotype of a mouse model of Charcot-Marie-Tooth disease. *Nature Medicine*, *10*(4), 396–401.

Pereira, M. P., Mühl, S., Pogatzki-Zahn, E. M., Agelopoulos, K., & Ständer, S. (2016). Intraepidermal Nerve Fiber Density: Diagnostic and Therapeutic Relevance in the Management of Chronic Pruritus: a Review. *Dermatology and Therapy*, *6*(4), 509–517.

Perez-Andres, M., Paiva, B., Nieto, W. G., Caraux, A., Schmitz, A., Almeida, J., Vogt, R. F., Marti, G. E., Rawstron, A. C., Van Zelm, M. C., Van Dongen, J. J., Johnsen, H. E., Klein, B., & Orfao, A. (2010). Human peripheral blood B-Cell compartments: A crossroad in B-cell traffic. *Cytometry Part B - Clinical Cytometry*, *78B*(SUPPL. 1), S47–S60.

Pillai, A. M., Thaxton, C., Pribisko, A. L., Cheng, G., Dupree, J. L., & Bhat, M. A. (2009). Spatiotemporal ablation of myelinating glia-specific neurofascin (NF155) in mice reveals gradual loss of paranodal axoglial junctions and concomitant disorganization of axonal domains. *Journal of Neuroscience Research*, *87*(8), 1773–1793.

Poliak, S., Salomon, D., Elhanany, H., Sabanay, H., Kiernan, B., Pevny, L., Stewart, C. L., Xu, X., Chiu, S. Y., Shrager, P., Furley, A. J., & Peles, E. (2003). Juxtaparanodal clustering of Shaker-like K+ channels in myelinated axons depends on Caspr2 and TAG-1. *Journal of Cell Biology*, *162*(6), 1149–1160.

Provitera, V., Nolano, M., Pagano, A., Caporaso, G., Stancanelli, A., & Santoro, L. (2007). Myelinated nerve endings in human skin. *Muscle and Nerve*, *35*(6), 767–775.

Prukop, T., Stenzel, J., Wernick, S., Kungl, T., Mroczek, M., Adam, J., Ewers, D., Nabirotchkin, S., Nave, K. A., Hajj, R., Cohen, D., & Sereda, M. W. (2019). Early short-term PXT3003 combinational therapy delays disease onset in a transgenic rat model of Charcot-Marie-Tooth disease 1A (CMT1A). *PLoS ONE*, *14*(1), e0209752.

Quách, T. D., Rodríguez-Zhurbenko, N., Hopkins, T. J., Guo, X., Hernández, A. M., Li, W., & Rothstein, T. L. (2016). Distinctions among Circulating Antibody-Secreting Cell Populations, Including B-1 Cells, in Human Adult Peripheral Blood. *The Journal of Immunology*, *196*(3), 1060–1069.

Querol, L., Nogales-Gadea, G., Rojas-Garcia, R., Martinez-Hernandez, E., Diaz-Manera, J., Suárez-Calvet, X., Navas, M., Araque, J., Gallardo, E., & Illa, I. (2013). Antibodies to contactin-1 in chronic inflammatory demyelinating polyneuropathy. *Annals of Neurology*, *73*(3), 370–380.

Querol, L., Rojas-García, R., Diaz-Manera, J., Barcena, J., Pardo, J., Ortega-Moreno, A., Sedano, M. J., Seró-Ballesteros, L., Carvajal, A., Ortiz, N., Gallardo, E., & Illa, I. (2015). Rituximab in treatment-resistant CIDP with antibodies against paranodal proteins. *Neurology: Neuroimmunology and NeuroInflammation*, *2*(5), e149.

Racanelli, V., Frassanito, M. A., Leone, P., Galiano, M., De Re, V., Silvestris, F., & Dammacco, F. (2006). Antibody Production and In Vitro Behavior of CD27-Defined B-Cell Subsets: Persistent Hepatitis C Virus Infection Changes the Rules. *Journal of Virology*, *80*(8), 3923–3934.

Rasband, M. N., & Peles, E. (2016). The nodes of Ranvier: Molecular assembly and maintenance. *Cold Spring Harbor Perspectives in Biology*, *8*(3).

Rosenbluth, J. (2009). Multiple functions of the paranodal junction of myelinated nerve fibers. *Journal of Neuroscience Research*, *87*(15), 3250–3258.

Rothstein, T. L., Griffin, D. O., Holodick, N. E., Quach, T. D., & Kaku, H. (2013). Human B-1 cells take the stage. *Annals of the New York Academy of Sciences*, *1285*(1), 97–114.

Sandelius, Å., Zetterberg, H., Blennow, K., Adiutori, R., Malaspina, A., Laura, M., Reilly, M. M., & Rossor, A. M. (2018). Plasma neurofilament light chain concentration in the inherited peripheral neuropathies. *Neurology*, *90*(6), e518–e524.

Saporta, M. A., Katona, I., Lewis, R. A., Masse, S., Shy, M. E., & Li, J. (2009). Shortened internodal length of dermal myelinated nerve fibres in Charcot-Marie-Tooth disease type 1A. *Brain*, *132*(12), 3263–3273.

Schafflick, D., Kieseier, B. C., Wiendl, H., & Meyer zu Horste, G. (2017). Novel pathomechanisms in inflammatory neuropathies.

Schenone, A., Nobbio, L., Bragadin, M. M., Ursino, G., & Grandis, M. (2011). Inherited neuropathies. *Current Treatment Options in Neurology*, *13*(2), 160–179.

Sereda, M. W., Griffiths, I., Pühlhofer, A., Stewart, H., Rossner, M. J., Zimmermann, F., Magyar, J. P., Schneider, A., Hund, E., Meinck, H. M., Suter, U., & Nave, K. A. (1996). A transgenic rat model of Charcot-Marie-Tooth disease. *Neuron*, *16*(5), 1049–1060.

Sereda, M. W., Meyer Zu Hörste, G., Suter, U., Uzma, N., & Nave, K. A. (2003). Therapeutic administration of progesterone antagonist in a model of Charcot-Marie-Tooth disease (CMT-1A). *Nature Medicine*, *9*(12), 1533–1537.

Shy, M. E., Blake, J., Krajewski, K., Fuerst, D. R., Laura, M., Hahn, A. F., Li, J., Lewis, R. A., & Reilly, M. (2005). Reliability and validity of the CMT neuropathy score as a measure of disability. *Neurology*, *64*(7), 1209–1214.

Sindhava, V. J., & Bondada, S. (2012). Multiple regulatory mechanisms control B-1 B cell activation. *Frontiers in Immunology*, *3*(DEC).

Snipes, G. J., & Suter, U. (1995). Molecular anatomy and genetics of myelin proteins in the peripheral nervous system. *Journal of anatomy*, *186*, 483–494.

Sommer, C. (2008). Skin biopsy as a diagnostic tool. *Current Opinion in Neurology*, *21*(5), 563–568.

Sommer, C., Weishaupt, A., Brinkhoff, J., Biko, L., Wessig, C., Gold, R., & Toyka, K. V. (2005). Paraneoplastic stiff-person syndrome: Passive transfer to rats by means of IgG antibodies to amphiphysin. *Lancet*, *365*(9468), 1406–1411.

Stathopoulos, P., Alexopoulos, H., & Dalakas, M. C. (2015). Autoimmune antigenic targets at the node of Ranvier in demyelinating disorders. *Nature Reviews Neurology*, *11*(3), 143–156.

Susuki, K., & Rasband, M. N. (2008). Spectrin and ankyrin-based cytoskeletons at polarized domains in myelinated axons. *Experimental Biology and Medicine*, *233*(4), 394–400.

Tangye, S. G. (2013). To B1 or not to B1: That really is still the question! *Blood*, *121*(26), 5109–5110.

Thaler, F. S., Thaller, A. L., Biljecki, M., Schuh, E., Winklmeier, S., Mahler, C. F., Gerhards, R., Völk, S., Schnorfeil, F., Subklewe, M., Hohlfeld, R., Kümpfel, T., & Meinl, E. (2019). Abundant glutamic acid decarboxylase (GAD)-reactive B cells in gad-antibody–associated neurological disorders. *Annals of Neurology*, *85*(3), 448–454.

Traka, M., Goutebroze, L., Denisenko, N., Bessa, M., Nifli, A., Havaki, S., Iwakura, Y., Fukamauchi, F., Watanabe, K., Soliven, B., Girault, J. A., & Karagogeos, D. (2003). Association of TAG-1 with Caspr2 is essential for the molecular organization of juxtaparanodal regions of myelinated fibers. *Journal of Cell Biology*, *162*(6), 1161–1172.

Üçeyler, N., Vollert, J., Broll, B., Riediger, N., Langjahr, M., Saffer, N., Schubert, A. L., Siedler, G., & Sommer, C. (2018). Sensory profiles and skin innervation of patients with painful and painless neuropathies. *Pain*, *159*(9), 1867–1876.

Uncini, A., & Vallat, J. M. (2018). Autoimmune nodo-paranodopathies of peripheral nerve: The concept is gaining ground. *Journal of Neurology, Neurosurgery and Psychiatry*, *89*(6), 627–635.

Uncini, A., Susuki, K., & Yuki, N. (2013). Nodo-paranodopathy: Beyond the demyelinating and axonal classification in anti-ganglioside antibody-mediated neuropathies. *Clinical Neurophysiology*, *124*(10), 1928–1934.

Van Paassen, B. W., Van Der Kooi, A. J., Van Spaendonck-Zwarts, K. Y., Verhamme, C., Baas, F., & De Visser, M. (2014). PMP22 related neuropathies: Charcot-Marie-Tooth disease type 1A and Hereditary Neuropathy with liability to Pressure Palsies. *Orphanet Journal of Rare Diseases*, *9*(1), 38–53.

Vega, J. A., Lopez-Muniz, A., G. Calavia, M., Garcia-Suarez, O., Cobo, J., Otero, J., Arias-Carrion, O., Perez-Pinera, P., & Menendez-Gonzalez, M. (2013). Clinical Implication of Meissner's Corpuscles. *CNS & Neurological Disorders - Drug Targets*, *11*(7), 856–868.

Verhamme, C., King, R. H., Ten Asbroek, A. L., Muddle, J. R., Nourallah, M., Wolterman, R., Baas, F., & Van Schaik, I. N. (2011). Myelin and axon pathology in a long-term study of PMP22-overexpressing mice. *Journal of Neuropathology and Experimental Neurology*, *70*(5), 386–398.

Vural, A., Doppler, K., & Meinl, E. (2018). Autoantibodies against the node of ranvier in seropositive chronic inflammatory demyelinating polyneuropathy: Diagnostic, pathogenic, and therapeutic relevance. *Frontiers in Immunology*, *9*(MAY).

Walsh, P. N., Friedrich, D. P., Williams, J. A., Smith, R. J., Stewart, T. L., Carter, D. K., Liao, H. X., McElrath, M. J., & Frahm, N. (2013). Optimization and qualification of a memory B-cell ELISpot for the detection of vaccine-induced memory responses in HIV vaccine trials. *Journal of Immunological Methods*, *394*(1-2), 84–93.

Weis, J., Claeys, K. G., Roos, A., Azzedine, H., Katona, I., Schröder, J. M., & Senderek, J. (2016). Towards a functional pathology of hereditary neuropathies. *Acta Neuropathologica*, *133*(4), 493–515.

Woo, S. H., Lumpkin, E. A., & Patapoutian, A. (2015). Merkel cells and neurons keep in touch. *Trends in Cell Biology*, *25*(2), arXiv NIHMS150003, 74–81.

Zhao, H. T., Damle, S., Ikeda-Lee, K., Kuntz, S., Li, J., Mohan, A., Kim, A., Hung, G., Scheideler, M. A., Scherer, S. S., Svaren, J., Swayze, E. E., & Kordasiewicz, H. B. (2018). PMP22 antisense oligonucleotides reverse Charcot-Marie-Tooth disease type 1A features in rodent models. *Journal of Clinical Investigation*, *128*(1), 359–368.

Zielasek, J., Martini, R., & Toyka, K. V. (1996). Functional abnormalities in P0-deficient mice resemble human hereditary neuropathies linked to P0 gene mutations. *Muscle and Nerve*, *19*(8), 946–952.

6 Abbreviations

AP	Alkaline phosphatase
BCR	B cell receptor
BSA	Bovine serum albumin
C	Celsius
Caspr	Contactin-associated protein 1
CD	Cluster of differentiation
CIDP	Chronic inflammatory demyelinating polyradiculoneuropathy
CK20	Cytokeratin 20
CMAP	Compound muscle action potential
CMT	Charcot-Marie-Tooth disease
CMT1A	Charcot-Marie-Tooth disease type 1A
CMTNSv2	Charcot-Marie-Tooth Neuropathy Score version 2
CNTN1	Contactin-1
DMSO	Dimethyl sulfoxide
DPBS	Dulbecco's phosphate buffered saline
DPBS/T	DPBS with 0.1% Tween
EBD	Evans Blue dye
EDTA	Ethylenediaminetetraacetic acid
ELISA	Enzyme-linked immunosorbent assay
ELISpot	Enzyme-linked immuno spot
EtOH	Ethanol
FACS	Fluorescence activated cell sorting
FCS	Fetal calf serum
FMO	Fluorescence minus one
G	Gauge
h	Hours
HRP	Horseradish peroxidase
IENFD	Intraepidermal nerve fiber density

Ig	Immunoglobulin
IL-2	Interleukin-2
K_V	Voltage-gated potassium
LRSC	Leukoreduction system chamber
MACS	Magnetic activated cell separation
MBP	Myelin basic protein
min	Minutes
mRNA	Messenger ribonucleic acid
NaCl	Sodium chloride
Na_V	Voltage-gated sodium
NCV	Nerve conduction velocity
NF155	Neurofascin-155
NF186	Neurofascin-186
PB	Plasmablast
PBMC	Peripheral blood mononuclear cell
PBS	Phosphate buffered saline
PFA	Paraformaldehyde
PGP9.5	Protein gene product 9.5
PMP22	Peripheral myelin protein 22 kDa
R848	Resiquimod
rpm	Revolutions per minute
RT	Room temperature
sec	Seconds
SFN	Small fiber neuropathy

7 Appendix

7.1 Technical equipment

Accu-jet® pro	Brand GmbH + Co. KG, Wertheim, Germany
Aluminum foil	Toppits®, Minden, Germany
Analog Vortex Mixer	VWR, Radnor, USA
BD FACSAriaIII	Beckton Dickinson, San Jose, USA
Biosphere Filter Tips	Sarstedt, Nuernbrecht, Germany
Canules 19G, 20G, 27G	BD Microlance™ 3, Beckton Dickinson, San Jose, USA
CatWalk™ XT	Noldus Information Technology, Wageningen, Netherlands
CCD camera	Visitron Systems, Tuchheim, Germany
Cell culture flask (25cm2, 75cm2)	Greiner Bio-One GmbH, Frickenhausen, Germany
CELLSTAR® serological pipette, sterile (5, 10, 25, 50ml)	Greiner Bio-One GmbH, Frickenhausen, Germany
Centrifuge 5471R	Eppendorf, Hamburg, Germany
Centrifuge Rotanta 460R	Hettich, Tuttlingen, Germany
Cryostat Leica CM 3050 S	Leica, Wetzlar, Germany
Cryovial®, 2ml, sterile	Biozym Scientific GmbH, Hess. Oldendorf, Germany
Dentalon® plus liquid	Kulzer GmbH, Hanau, Germany
Dentalon® plus powder	Kulzer GmbH, Hanau, Germany
Disposable scalpel CUTFIX, 10- and 15-blade	B. Braun, Melsungen, Germany
Eppis: safe-lock tube 2.0ml	Eppendorf, Hamburg, Germany
Falcon Tubes (15ml, 50ml)	Greiner Bio-One GmbH, Frickenhausen, Germany
Freezer confort -20°C	Liebherr, Biberach, Germany

Freezer TSX Series-80°C	Thermo Scientific, Waltham, USA
Gelaire BSB 4A sterile bench	Gelaire® flow laboratories, Sydney, Australia
Hamilton microliter syringe	Hamilton Company, Reno, USA
Hargreaves apparatus	Ugo Basile Inc., Comerio, Italy
Heracell 150 Incubator	Heraeus Instruments, Hanau, Germany
KNT LABOPORT Mini membrane vacuum pump N86	KNF Neuberger GmbH, Freiburg, Germany
LS Columns	Miltenyi Biotec B.V. & Co. KG, Bergisch Gladbach, Germany
MACS MultiStand	Miltenyi Biotec B.V. & Co. KG, Bergisch Gladbach, Germany
Memmert water bath	A. Hartenstein GmbH, Würzburg, Germany
Microscopes Ax10	Zeiss, Oberkochen, Germany
Microscopes Axiophot 2	Zeiss, Oberkochen, Germany
MidiMACS™ Separator	Miltenyi Biotec B.V. & Co. KG, Bergisch Gladbach, Germany
MiniMACS™ Separator	Miltenyi Biotec B.V. & Co. KG, Bergisch Gladbach, Germany
MS Columns	Miltenyi Biotec B.V. & Co. KG, Bergisch Gladbach, Germany
Multipipette 200 (25-200µl)	Eppendorf, Hamburg, Germany
Multiskan™ FC microplate photometer	ThermoFisher Scientific, Waltham, USA
Neubauer counting chamber	A. Hartenstein GmbH, Würzburg, Germany
Neurosoft-Evidence 3102 electromyograph	Schreiber & Tholen Medizintechnik, Stade, Germany
Objectslides superfrost	Langenbrinck, Tenningen, Germany
OLYMPUS CKX41 inverted microscope	Olympus, Hamburg, Germany
Optical adhesive covers	Langenbrinck, Teningen, Germany
Parafilm®M	Bemis Company Inc., Oshkosh, USA
PE-10 tubing	Instech Laboratories, Inc., Plymouth Meeting, USA

Rapid-Flow™ 50mm Bottle Top Filter	Thermo Scientific, Nalgene
Research plus pipette (1-10, 10-100, 100-1000µl)	Eppendorf, Hamburg, Germany
Super PAP-Pen liquid blocker	Science Services GmbH, Munich Germany
Surgical instruments	FST, Heidelberg, Germany
Suture Dafilon 4/0	B. Braun, Melsungen, Germany
Suture Silkam 4/0	B. Braun, Surgical, S. A. Rubi, Spain
Stereotactic frame	Custom-made
Syringes (1ml, 5ml)	BD Plastipak™, Beckton Dickinson, San Jose, USA
Tissue-Tek ® Cryomold	Sakura, Staufen, Germany
Transfer pipette 3.5ml	Sarstedt, Nuernbrecht, Germany
TSE RotaRod Advanced	TSE Systems, Bad Homburg, Germany
von-Frey filaments	Stoelting, Wood Dale, USA
0.28mm copper wire	BLOCK Transformatoren-Elektronik GmbH, Verden, Germany
30-µm mesh filter	Miltenyi Biotec B.V. & Co. KG, Bergisch Gladbach, Germany
30G canules	SFM Hospital Products GmbH, Berln,Germany
5ml polystyrene Round-Boottom Tube	Corning/FALCON, Corning, USA
96-Well ELISA U plates	ThermoFisher Scientific, Waltham, USA
96-Well ELISPOT plates	ThermoFisher Scientific, Waltham, USA

7.2 Reagents

Aqua, Ecotainer®	B. Braun, Melsungen, Germany
Blue AP substrate kit	Vector Laboratories, Burlingame, USA
Bovine serum albumin	Sigma-Aldrich, Munich, Germany
DMSO ROTIPURAN® 99.8%, p.a.	Carl Roth GmbH + Co. KG, Karlsruhe, Germany

Dulbecco's phosphate buffered saline	Sigma-Aldrich, Munich, Germany
EDTA salt solution	Sigma-Aldrich, Munich, Germany
Ethanol	Sigma-Aldrich, Munich, Germany
Evans blue dye	Sigma-Aldrich, Munich, Germany
FcR Blocking Reagent, human	Miltenyi Biotec B.V. & Co. KG, Bergisch Gladbach, Germany
Fetal calf serum	Biochrom GmbH, Berlin, Germany
Isoflurane (1ml/ml)	CP-Pharma Handels GmbH, Burgdorf, Germany
Lymphoprep™	Alere Technologies AS, Oslo, Norway
Normal Goat Serum	Agilent Technologies GmbH & Co. KG, Hamburg, Germany
Penillicin/streptomycin	Gibco®/Life Technologies™, Carlsbad, USA
REAlease CD19 MicroBead Kit, human	Miltenyi Biotec B.V. & Co. KG, Bergisch Gladbach, Germany
RPMI1640 medium	Gibco®/Life Technologies™, Carlsbad, USA
Sulfiric acid	Carl Roth, Karlsruhe, Germany
Tissue-Tek® O.C.T. Compound	Sakura, Staufen, Germany
Triton X-100	Carl Roth, Karlsruhe, Germany
Trypan blue solution (0.4%)	Sigma-Aldrich, Munich, Germany
Tween20	Carl Roth, Karlsruhe, Germany
Ursotamin (Ketaminhydrochloride)	Serumwerk Bernburg AG, Bernburg, Germany
Viobility staining 488/520 Fixable Dye	Miltenyi Biotec B.V. & Co. KG, Bergisch Gladbach, Germany
Xylazine (Xylavet)	CP-Pharma Handels GmbH, Burgdorf, Germany
0.9% NaCl solution	B. Braun, Melsungen, Germany

7.3 Buffers, media and solutions

Cell culture medium	1640 RPMI medium 10% FCS 1% penillicin/streptomycin
Stimulation medium	1640 RPMI medium 10% FCS 1% penillicin/streptomycin 15 ng/ml IL-2 2.5 µg/ml R848
MACS buffer	DPBS 0.5% BSA 2 mM EDTA
FACS medium	1640 RPMI medium, phenol red-free 0.5% BSA 2 mM EDTA
PBS	137 mM NaCl 2.7 mM KCL 1.5 mM KH 2 PO 4 8.1 mM Na 2 PO 4 pH 7.4
Carbonate-bicarbonate buffer	0.1 M Na_2CO_3 0.1 M $NaCO_3$ pH 9.6

7.4 Staining antibodies

Reactivity	Host/ Clone	Catalog number	Company	Dilution/ concentration	Fixation/ additives	Conjugation	Study
S-100	rabbit	ab868	Abcam	1:100	4% PFA / 0.3% TritonX 100	none	CMT1A
PGP9.5	rabbit	7863-1004	Bio-Rad	1:200	4% PFA / 0.3% TritonX 100	none	CMT1A
PGP9.5	mouse	516-3344	Zytomed	1:200	4% PFA / 0.3% TritonX 100	none	CMT1A
MBP	mouse	GTX11159	GeneTex	1:200	4% PFA / 0.3% TritonX 100	none	CMT1A
CK20	mouse	61054	PROGEN Biotechnik	1:40	4% PFA / 0.3% TritonX 100	none	CMT1A
Langerin/ CD207	rabbit	DDX0362	Dendritics	1:500	4% PFA / 0.3% TritonX 100	none	CMT1A
NF155	rabbit	ab31457	Abcam	1:100	4% PFA / 0.3% TritonX 100	none	CMT1A
Caspr	rabbit	ab34151	Abcam	1:500	4% PFA / 0.3% TritonX 100	none	CMT1A
pan-sodium channel	mouse	S8809	Sigma Aldrich	1:100	4% PFA / 0.3% TritonX 100	none	CMT1A
mouse IgG	donkey	715-165-151	Jackson Immuno Research	1:100	4% PFA / 0.3% TritonX 100	Cy3	CMT1A
rabbit IgG	donkey	711-545-152	Jackson Immuno Research	1:400	4% PFA / 0.3% TritonX 100	Alexa Fluor488	CMT1A
human IgG	goat	109-165-003	Jackson Immuno Research	1:100	4% PFA / 0.3% TritonX 100	Cy3	Passive transfer
CD3	REA613	130-113-138	Miltenyi Biotec	1:100	none	FITC	B cells

CD19	LT19	130-113-649	Miltenyi Biotec	1:50	none	VioGreen	B cells
CD20	REA780	130-111-338	Miltenyi Biotec	1:50	none	PE	B cells
CD27	M-T271	130-100-442	Miltenyi Biotec	1:50	none	PE-Vio770	B cells
CD38	REA572	130-113-429	Miltenyi Biotec	1:50	none	APC	B cells
CD43	REA833	130-114-596	Miltenyi Biotec	1:50	none	APC-Vio770	B cells
human IgG	goat	2040-01	Biozol	5µg/ml / 1:2000	none	none	ELISPOT/ ELISA
human IgM	goat	2020-01	Biozol	5µg/ml / 1:2000	none	none	ELISPOT/ ELISA
human IgG	goat	A18808	Invitrogen	1:4000	none	AP	ELISPOT
human IgM	goat	A18838	Invitrogen	1:4000	none	AP	ELISPOT
human IgG	goat	A18805	Invitrogen	1:20000	none	HRP	ELISA
human IgM	goat	A18835	Invitrogen	1:20000	none	HRP	ELISA
human kappa chain	SB81a, mouse	9230-01	Biozol	10µg/ml	none	none	ELISPOT
chicken IgY	goat	PA1-28798	Thermo Fisher Scientific	1:5000	none	HRP	ELISA
human Neuro-fascin	chicken	AF3235	R&D systems	1:1000	none	none	ELISA
human CNTN1	goat	ab191285	abcam	1:400	none	none	ELISA
goat IgG	donkey	ab205723	abcam	1:1000	none	HRP	ELISA

List of Figures

List of Tables

8 Curriculum vitae

9 Danksagung

Großer Dank gilt Frau Prof. Claudia Sommer und Frau PD Kathrin Doppler, die mir ermöglichten, meine Doktorarbeit in ihrer Arbeitsgruppe durchzuführen. Für die Betreuung und die einzigartige Gelegenheit, mein Methodenspektrum in diesem Umfang zu erweitern, möchte ich mich ebenfalls bedanken.

Bei Herrn Prof. Rudolf Martini bedanke ich mich für die wertvollen und konstruktiven Ratschläge zum Gelingen meiner Arbeit und natürlich auch dafür, dass ich im Journal Club seiner Arbeitsgruppe teilnehmen und vieles lernen konnte.

Bei Frau Prof. Heike Rittner möchte ich mich ebenfalls für die hilfreiche Kritik bedanken, die zum Gelingen dieser Arbeit beigetragen hat.

Ebenfalls möchte ich mich bei den Mitgliedern des CMT-NETs für die Sammlung der Hautbiopsien, insbesondere bei Dr. Lisa Reinecke für die reibungslose Koordinierung, bedanken.

Für die tatkräftige Unterstützung bei der Durchführung der Tierexperimente möchte ich mich ganz herzlich bei Frau Lydia Biko bedanken, die mir vieles erleichtert hat und jederzeit hilfreichen Rat parat hatte. Auch bei Frau Maria Gallant bedanke ich mich für die große Hilfe in jedem erdenkbaren Bereich der Experimente. Frau Barbara Dekant gilt ebenfalls Dank für ihre umfassende Organisation und Vorbereitung der Gewebeentnahmen, sowie für das Durchführen der vielen Färbungen. Weiterer Dank gilt auch allen Zupfhelferinnen für das Zupfen der unzählbar vielen Nerven und natürlich auch den Kuchenessern, mit denen die Kuchenpausen bei OPs und Gewebeentnahmen immer sehr entspannend waren.

Außerdem möchte ich mich bei Frau Helga Brünner bedanken, die für tierexperimentelle Fragen, ob organisatorische oder praktische, jederzeit ein offenes Ohr hatte. Ein großer Dank geht auch an die Tierpfleger für die ständige Umsorgung der Tiere.

Ein ganz außergewöhnliches Dankeschön möchte ich auch Herrn Dr. Damiano Rovituso aussprechen, mit dem ich nicht nur sehr viele, sondern auch sehr vielfältige Stunden im Labor verbracht habe. Ohne seiner leidenschaftlichen Arbeit am B-Zell-Projekt und seiner unermüdlichen Lehr- und Erklärungsbereitschaft hätte dieses Projekt nicht so weit fortgeschreiten können. Bei Dr. Martha-Lena Müller möchte ich mich ebenfalls sehr herzlich für ihre großartige Unterstützung und Hilfsbereitschaft im B-Zell-Projekt bedanken. Ihre Begeisterung und Motivation haben nicht nur auf das gemeinsame Arbeiten, sondern auch die Kaffeepausen, super angenehm gemacht. Ein großes Dankeschön geht auch an Frau Sonja Mildner, die mich im B-Zell-Projekt ebenfalls tatkräftig unterstützt hat.

Weiterhin möchte ich mich bei meinen Bürokolleginnen für die tolle Zeit und Stimmung bedanken. Besonders möchte ich mich bei Julia Grüner bedanken, die mir nicht nur im Büro oder Labor, sondern auch allen anderen Angelegenheiten, stets gerne eine Hilfe war.

Allen anderen Mitgliedern der Arbeitsgruppen Sommer, Doppler und Üçeyler möchte ich mich ebenfalls für die ständige Hilfsbereitschaft im Labor und bei organisatorischen Angelegenheiten bedanken. Ebenso danke ich den Mitgliedern der AG Martini für die freundliche Aufnahme im Journal Club.

Zu guter Letzt möchte ich mich bei meiner Familie und besonders bei meinen Freunden bedanken, die, so oft es ging, ganz hervorragend für äußerst gute Ablenkung vom Laboralltag gesorgt haben.